Universitat de Girona

SIMULATION OF DELAMINATION IN COMPOSITES UNDER QUASI-STATIC AND FATIGUE LOADING USING COHESIVE ZONE MODELS

Albert TURON TRAVESA

ISBN: 978-84-690-4372-1
Dipòsit legal: GI-285-2007

Universitat de Girona
Escola Politècnica Superior
Dept. d'Enginyeria Mecànica i de la Construcció Industrial

Simulation of delamination in composites under quasi-static and fatigue loading using cohesive zone models

A thesis submitted for the degree of Doctor of Philosophy

by

Albert Turon Travesa

2006

Advisors:

Pedro P. Camanho
Universidade do Porto, Portugal

Josep Costa Balanzat
Universitat de Girona, Spain

To whom it might concern,

Dr. Pedro P. Camanho, Assistant Professor at the University of Porto, and Josep Costa Balanzat, Associate Professor at the University of Girona,

CERTIFY that the study entitled "Simulation of delamination in composites under quasi-static and fatigue loading using cohesive zone models" has been carried out under their supervision by Albert Turon Travesa to obtain the doctoral degree,

Girona, October 2006,

Pedro P. Camanho
Universidade do Porto, Portugal

Josep Costa Balanzat
Universitat de Girona, Spain

The present work has been funded by the Universitat de Girona under research grant BR01/09. Also, it has been partially funded by the Spanish Government under research projects MAT2000–00741–C02–01 and MAT2003–09768–C03–01.

This research was conducted in part during the author's visits to the Universidade do Porto, Portugal, and NASA Langley Research Center, Hampton VA, USA, which were funded by University of Girona and by NASA Langley Research Center.

Agraïments - Aknowledgements

The subject of this work starts from the ideas of my thesis advisors, Dr. Josep Costa Balanzat and Pedro Manuel Ponces Rodrigues de Castro Camanho. Their excellent ideas, advice and support were invaluable for the completion of this work and I render thanks to them.

I would like to express my gratitude to Carlos Dávila for his continuous interest in the work and his valuable comments and contributions that were very constructive. I would also like to thank him for having offered me the possibility to visit NASA Langley during the summers of 2004 and 2005.

A la Universitat de Girona he tingut la possibilitat de treballar en el grup de recerca AMADE, on en tot moment m'han facilitat la feina. Voldria agraïr a en Narcís Gascons, que fou qui em va introduir dins AMADE. Agraïr especialment l'amistat, els consells i la seva sempre bona disposició d'en Joan Andreu, en Jordi Renart, en Pere Maimí, en Pep, en Benigne, en Norbert, en Dani, l'Elio, en Sergi, l'Emili, la Montse i la Marta, tots plegats hem passat bones estones.

I would also like to thank you Cassilda and Sukdee with whom I have shared the different phases of the research stages in Porto and in Hampton, respectively.

Voldria agraïr també el suport dels meus amics, en Santi, en Sergi, la Maria, la Gemma, la Yolanda, en Toni, la Carme i especialment a en Dani pel seu continu interés. De les dues preguntes que sempre em feieu: de què va la tesi? quan acabaràs? ara si que ja puc respondre la segona. Per la primera us deixo que la llegiu!

Un agraïment profund als meus pares, Llorenç i Isabel, la meva àvia Francesca i especialment a la meva germana Margarita pels inestimables ànims i el seu continu suport.

Finalment, el meu més sincer agraïment a l'Anna. Ella va ser qui més em va esperonar a emprendre aquest viatge i la seva paciència, comprensió i recolzament m'han ajudat molt durant tot aquest temps.

al meu avi,

Contents

List of Figures **5**

List of Tables **11**

1 Introduction and objectives **15**

I Delamination under quasi-static loading **21**

2 Delamination in composite materials **23**

2.1 Introduction 23

2.1.1 Origin of delamination 23

2.1.2 Types of delamination 24

2.2 Micromechanics of delamination 26

2.3 Approaches to delamination 28

2.3.1 Fracture Mechanics approach 29

2.3.2 Cohesive or Damage Zone Models 31

3 Interface damage model **39**

3.1 Introduction 39

3.2 Model for delamination onset and propagation 41

3.2.1 Boundary value problem 41

3.2.2 Kinematics of the interfacial surface 42

3.2.3 Constitutive laws 44

3.2.4 Formulation of the constitutive tangent tensor 55
3.3 Finite element discretization - computational model 56
3.3.1 Discretization of the interfacial surface 57
3.4 Comparison with experimental studies 59
3.4.1 Mode I, mode II and mixed-mode I and II delamination 60
3.4.2 Skin-stiffener co-cured structure 66
3.5 Concluding remarks 70

4 Analysis of the mesh size influence 71
4.1 Introduction 71
4.2 Selection of cohesive zone model parameters 72
4.2.1 Cohesive zone model and FEM 72
4.2.2 Guidelines for the selection of the parameters of the interface with coarser meshes 78
4.3 Simulation of the double cantilever beam specimen 80
4.3.1 Effect of interface strength 84
4.3.2 Effect of interface stiffness 86
4.4 Simulation of free-edge delamination 87
4.4.1 Problem statement 87
4.4.2 Numerical predictions 89
4.5 Concluding remarks 93

II Delamination under fatigue loading 95

5 Fatigue in composite materials 97
5.1 Fatigue modeling 97
5.1.1 Fatigue life models 98
5.1.2 Fracture Mechanics models 99
5.1.3 Damage Mechanics models 101

5.2 Fatigue delamination of composite laminates 104
5.2.1 Introduction 104
5.2.2 Fatigue growth of interlaminar cracks 104
5.2.3 Simulation of fatigue delamination of composite laminates . . 109

6 Simulation of fatigue delamination 117

6.1 Introduction and motivation 117
6.2 Cohesive Zone Model approach 118
6.2.1 Numerical implementation of to the CZM 119
6.3 Constitutive model for high-cycle fatigue 120
6.3.1 Determination of the growth rate of the damaged area as a function of the number of cycles 121
6.3.2 Evolution of the damage variable under cyclic loading 123
6.3.3 Crack growth rate 123
6.3.4 Cycle jump strategy 126
6.4 Results and discussion 127
6.4.1 One element tests 128
6.4.2 Simulation of a DCB specimen under fatigue loading 130
6.4.3 Simulation of a 4ENF test 135
6.4.4 Simulation of mixed-mode loading 139
6.5 Conclusions 142

III Closure 143

7 Conclusions and Future Work 145

7.1 Conclusions 145
7.1.1 Cohesive zone model for the simulation of delamination under quasi-static loads 145

7.1.2 Cohesive zone model for the simulation of delamination under high-cycle fatigue . . . 147
7.2 Suggestions for Future Work . . . 148
7.2.1 Quasi-static Model . . . 148
7.2.2 Fatigue Model . . . 148
7.2.3 Environmental Effects . . . 149
7.2.4 Stochastic Distributions . . . 150

IV Appendices 151

A Cohesive element User Manual 153
A.1 Preface . . . 154
A.2 Introduction . . . 154
A.3 Formulation of the Element . . . 154
A.3.1 Basic element theory . . . 154
A.3.2 Element definition . . . 156
A.3.3 Implementation status . . . 157
A.4 Input into ABAQUS/Standard . . . 159
A.4.1 Element type . . . 159
A.4.2 Number of nodes and coordinates per node . . . 159
A.4.3 Element properties . . . 159
A.4.4 Number of solution-dependent variables . . . 161
A.5 Examples . . . 161
A.5.1 One element simulations . . . 162
A.5.2 Mode I, mode II and mixed-mode delamination growth for PEEK composites . . . 164

B Code 167

C Input files **181**

C.1 One element simulations 181

C.1.1 Input file for an 8-node decohesion element that connects two three dimensional continuum elements. 181

C.1.2 Input file for an 4-node decohesion element that connects two continuum plane strain element 184

C.1.3 Input file for an 4-node decohesion element that connects two continuum plane strain element. Rotated 90º. 186

C.2 Mode I, mode II and mixed-mode delamination 188

C.2.1 Input file for the DCB test. 188

C.2.2 Input file for the ENF test. 191

C.2.3 Input file for the MMB 80 test. 194

Bibliography **198**

List of Figures

1.1 *Building block integration of the certification methodology (Mil-Hbk-17 [1]) and reduction on the test requeriments through Virtual Mechanical Testing.* 16

2.1 *Internal delamination: (a) disposition across the laminate and (b) effect on the overall stability (Figure from Bolotin [6]).* 25

2.2 *Near-surface delamination: (a) open in tension; (b) closed in tension; (c) open buckled; (d) closed buckled; (e) edge buckled and (f) edge buckled with secondary crack (Figure from Bolotin [6]).* 26

2.3 *Mode I, mode II, and mode III crack propagation modes.* 27

2.4 *Formation and growth of a mode II delamination at the ply interface: (a) microcrack formation ahead of the crack tip; (b) microcrack growth and opening and (c) microcrack coalescence accompanied by shear cusps [9].* 28

2.5 *Calculation of the energy release rate using Virtual Crack Closure Technique.* 30

2.6 *Tractions in the cohesive zone ahead of the crack tip.* 32

2.7 *Equivalence between the physical cohesive model and the numerical cohesive model.* 35

2.8 *Traction-relative displacement curves employed in various models in the literature (Figure from Zou et al.[66]).* 37

3.1 *Restoration of the cohesive state for delamination propagation under variable mode-ratio.* 40

3.2 *Body Ω crossed by a material discontinuity Γ_d in the undeformed configuration.* 41

3.3 *Interfacial surface deformation.* 43

3.4 *Energy dissipation during damage evolution.* 46

3.5 *A bilinear constitutive equation for the cohesive element for a mixed-mode loading situation.* 49

3.6 *Comparison between Ye's criterion, a maximum traction criterion and the new proposed criterion.* 53

3.7 *Isodamage curves in the relative displacements space.* 54

3.8 *MMB test specimen.* 60

3.9 *Numerical and experimental results- pure mode I loading.* 63

3.10 *Numerical and experimental results- mixed-mode I and II loading with G_{II}/G_T=20%.* 63

3.11 *Numerical and experimental results- mixed-mode I and II loading with G_{II}/G_T=50%.* 64

3.12 *Numerical and experimental results- mixed-mode I and II loading with G_{II}/G_T=80%.* 64

3.13 *Numerical and experimental results- pure mode II loading.* 65

3.14 *Skin-stiffener test specimen.* 66

3.15 *Skin-Stiffener debonding.* 68

3.16 *Experimental and numerical load-extensometer displacement relations.* 69

4.1 *Influence of the cohesive surface on the deformation.* 73
4.2 *Distribution of tractions ahead of the crack tip at peak load.* 81
4.3 *Load-displacement curves using the nominal interface strength (τ^0=60MPa) for a DCB test with different mesh sizes.* 83

4.4 *Distribution of tractions ahead of the crack tip for an applied load of 30kN.* 84
4.5 *Load-displacement curves obtained for a DCB test with different mesh sizes with the interface strength modified to keep $N_e \geq 5$.* 85
4.6 *Maximum load obtained in a DCB test for two cases: a) with constant interfacial strength, b) with interfacial strength calculated according to Eq. (4.9).* 86
4.7 *Influence of the interface stiffness on the load-displacement curves.* . . 87
4.8 *Cross-section of the laminate.* 88
4.9 *Load-displacement curves obtained for a free-edge test with different mesh sizes using nominal interface strength properties.* 90

4.10 *Evolution of stresses during delamination onset and propagation of the two interior layers of the laminate.* 90

4.11 *Load-displacement curves obtained for a free-edge test with different mesh sizes and with the interface strength adjusted for N_e =5.* 92
4.12 *Load-displacement curves obtained for a free-edge test with different mesh sizes and with the interface strength adjusted for N_e =10.* 92
4.13 *Maximum load obtained in a free-edge test for three cases: a) with constant interfacial strength, b) and c) with interfacial strength calculated according to Eq.(4.9) with N_e equal to 5 and 10.* 93

5.1 *Typical crack growth rate pattern.* 101

5.2 *Delamination onset surface for IM7/8552 mixed-mode I/II fatigue failure [154].* 110

6.1 *Linear softening law for a cohesive zone model approach.* 119

6.2 *Equivalence between the physical (left) and numerical (right) constitutive equation of the CZM.* 120

6.3 *Schematic representation of the equivalence between the increase in the damaged area and the crack growth.* 122

6.4 *Variation of the energy release rate.* 125

6.5 *The load ratio effect is captured by the constitutive equations. The higher load ratios ($R_1 > R_2$) the smaller ΔG ($\Delta G_2 > \Delta G_1$).* 126

6.6 *Undeformed mesh with the boundary conditions and deformed mesh of one cohesive element tests.* 128

6.7 *Evolution of the interface traction in the constitutive equation for a displacement jump controlled high-cycle fatigue test.* 129

6.8 *Evolution of the interface traction and the maximum interface strength as a function of the number of cycles for a displacement jump controlled high-cycle fatigue test.* 130

6.9 *Loading pattern for Mode I specimen.* 131

6.10 *Detail of the FEM model of the DCB specimen. Two applied load P with opposite direction were applied to each arm. The applied moment is equal to the product between the applied load P and the thickness of the arm.* 132

6.11 *Comparison of the experimental data with the crack growth rate obtained from the numerical simulation for a Mode I DCB test.* 134

6.12 *Sensitivity of the model to the load ratio for a Mode I DCB test.* . . 135

6.13 *Sensitivity of the model to the load ratio for a Mode I DCB test.* . . 136

6.14 *Loading pattern for Mode II 4ENF specimen.* 136

6.15 *Detail of the FEM model of the 4ENF specimen.* 137

6.16 *Comparison of the experimental data with the crack growth rate obtained from the numerical simulation for a Mode II 4ENF test.* . . . 138

6.17 *Loading pattern for mixed-mode specimen.* 139

6.18 *Detail of the FEM model of the specimen mixed-mode loaded.* 140

6.19 *Comparison of the experimental data with the crack growth rate obtained from the numerical simulation for a mixed-mode test with* $G_I = G_{II}$. 141

A.1 Element node-numbering conventions 156

A.2 *A bilinear constitutive equation for the cohesive element for a mixed-mode loading situation* 158

A.3 Undeformed and deformed mesh of models with an 8-node cohesive element (left), and a 4-node cohesive element (center and right), connecting two continuum elements. 162

A.4 Load-displacement curve for models with one cohesive element 163

A.5 Undeformed and deformed mesh for the MMB simulation 165

A.6 Load-displacement curves for DCB, ENF and MMB 80% tests 165

List of Tables

3.1 *Ply properties.* 61

3.2 *Experimental data.* 61

3.3 *Maximum loads.* 65

3.4 *Material properties for IM6-3501-6 unidirectional graphite epoxy.* . . 67

3.5 *Interface properties for IM6-3501-6 unidirectional graphite epoxy.* . . 67

3.6 *Comparison between experimental and numerical results.* 68

4.1 *Interface stiffness K proposed by different authors (N/mm^3) and those calculated from Equation (4.4).* 75

4.2 *Length of the cohesive zone and equivalent value of the parameter M.* 77

4.3 *Mechanical and interface material properties of T300/977-2 [48],[110].* 81

4.4 *Mechanical properties of T300/934 Graphite Epoxy [111], [114].* . . . 88

4.5 *Summary of predicted and experimental values of tension tests on T300/934 laminates.* 91

6.1 *Properties used in the models with only one cohesive element.* 128

6.2 *Material properties for HTA/6376C carbon/epoxy [140, 167, 168].* . 131

6.3 *Fatigue material properties for HTA/6376C carbon/epoxy obtained from references [140, 168] and using Equations (6.20) to (6.22).* . . 133

Chapter 1

Introduction and objectives

The structural applications of polymer-matrix composite materials reinforced with continuous fibres are gradually expanding as a result of the mechanical properties of these materials (e.g. excellent stiffness/weight and strength/weight ratios, easy formability, and corrosion resistance). Aerospace and aeronautics can be considered to be the pioneering industries in the application of this type of composites, although nowadays composite materials are used as base materials in the most advanced products of many sectors such as naval engineering, civil engineering, automobile industry, sporting equipment, etc.

The application of composites in structural components (e.g. main load-bearing structures of aircraft) is still limited by the difficulty in predicting their service lives. In fact, whilst military aircrafts are mainly built with composite materials, civil aircrafts still use metals in several structural components. As the understanding of its behaviour improves, the use of composite materials spreads. However, the usual methodology for the determination of their reliability, which implies a large number of tests in real-size structural components, is only suitable in sectors with a large added value, such as aeronautics, that can afford the design and certification costs. Moreover, existing mechanical tests are not always able to reproduce all the possible circumstances that will be encountered during service life (environmental conditions, cyclic loads, load combination, etc.). To increase the reliability and to

decrease the the number of required tests to certify a composite structure (see Figure 1.1), efficient design tools are needed. These tools must be robust, efficient, and carefully validated against test data to ensure that they are capable of predicting consistently the response of components in service. Such capability to substitute some of the mechanical test with accurate computer simulations is referred to as "virtual mechanical testing". The development of this kind of tools needs a deep knowledge of the material behaviour.

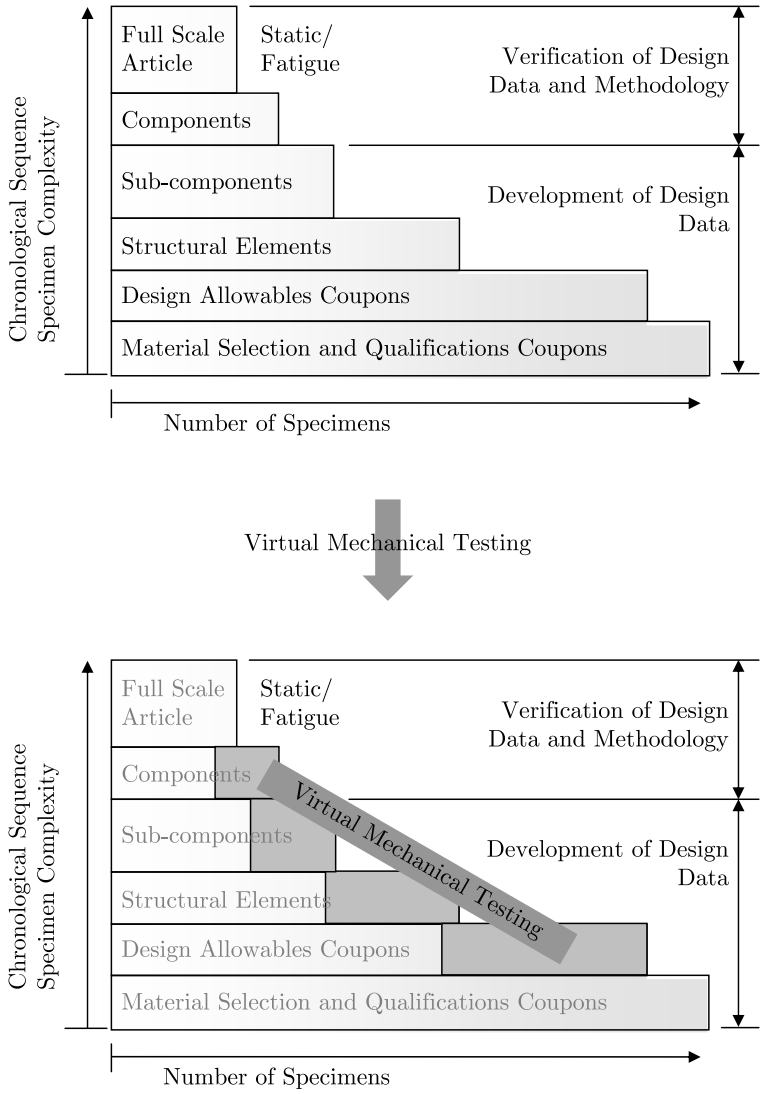

Figure 1.1: *Building block integration of the certification methodology (Mil-Hbk-17 [1]) and reduction on the test requeriments through Virtual Mechanical Testing.*

Moreover, the philosophy behind the design of advanced components differs from the conventional methodology to design structural components. While the conventional approach is based on a strength verification, i.e, the ability of the structure or the material to resist the damage occurrence; the new concepts are also based on a damage-tolerance verification besides the strength verification, i.e. the damaged material should maintain the functionality after damage occurrence. The damage-tolerance approach allows for the presence of subcritical cracks that will not grow to critical length between periodic inspections. The damage-tolerance concept provides quantitative guidance for balancing of the cost of repair or replacement of a damaged component against the possibility that continued service could lead to failure.

The strength-based design relies on the obtention of "design allowable values", generally obtained from a selected experimental tests and corrected by safety factors (or uncertainty factors). These uncertainty factors are used to consider the variations between the constraints considered in the design (variations in the material properties, environmental effects, load combination, etc.) and the real conditions of the component or structure in service. Usually, the design allowable values are obtained for static loading while fatigue loading is taken into account in the design through the increase of the safety factor.

However, the damage-tolerance approach requires the use of techniques that allow to predict both crack initiation and growth to verify that subcritical cracks will not grow to critical lengths between periodic inspections. In-service loads of the real components or structures are mostly of cyclic origin. Under these circumstances, damage-tolerance approach is especially important in real structures loaded under fatigue conditions, where the growth of subcritical cracks is the main cause of failure. The experimental characterization of the fatigue behavior of large components requires a large number of tests. Therefore, the development of complete and efficient design tools that take into account fatigue loading can significantly reduce the development costs. Moreover, damage-tolerance techniques allow to schedule the

maintenance or replacement of components before catastrophic failure.

The design of primary and secondary composite structures for aeronautical applications involves both concepts, strength and damage-tolerance. The development of specific tools for composites that are able to predict the strength and damage-tolerance is still a problem under investigation.

The special microstructural characteristics of composites (anisotropy, heterogeneity, the existence of a matrix/fibre interface with its own properties and the presence of defects) creates difficulties in the development of constitutive models to assist structural design.

The usual failure mechanisms in composites can be divided in: i) fibre failure modes, tensile fracture or local compressive kinking; ii) matrix failure modes, generally matrix cracking although other effects such as degradation caused by radiation or by moisture uptake should be taken into account; iii) fibre/matrix interface failure or fibre/matrix debonding; iv) inter-laminar interface failure, or cracks caused by the loss of adhesion between two consecutive laminae, normally called delamination. Among these different failure mechanisms, delamination is one of the most common types of damage in laminated fibre-reinforced composites due to their relatively weak interlaminar strengths. Delamination may arise under various circumstances, such as in the case of transverse concentrated loads caused by low velocity impacts. This damage mode is particularly important for the structural integrity of composite structures because it is difficult to detect during inspection. Furthermore, delamination causes a drastic reduction of the bending stiffness of a composite structure and, when compressive loads are present, promotes local buckling that can compromise the global stability of the structure.

The initiation of a delamination-like defect does not necessarily mean that a structural component is at, or even near, the end of its useful service life. An efficient design tool able to predict the initiation of a delamination could improve the design based on strength criteria. On the other hand, models of interlaminar crack growth improve the design oriented to damage-tolerance and provide decision

tools for the definition of the repair/subsitution of damaged structures [2].

Reliable and efficient design tools are needed to improve the design and decrease the development cost of a composite component. These tools need to be developed using the damage-tolerance approach to take into account all of the stages of the composite component during its lifetime. The design tools must take into account fatigue loading, which is the most typical nature of the in-service loads. The development of accurate and general design tools requires the study of delamination under static and fatigue loading. To facilitate the widespread use of advanced design tools, they have to be implemented in numerical methods normally used in the design of structures (such the Finite Element Method) and accessible to the majority of the designers.

The objective of this thesis is to develop an effective design tool to analyze delamination onset and growth in advanced composite materials under quasi–static and fatigue loading.

The methodology used to pursue this objective is structured as follows. The thesis is divided in two parts: the numerical tools to simulate delamination under quasi-static loading are described in Part I; the numerical tools to simulate delamination under fatigue loading are described in Part II.

Part I comprises Chapters 2 through 4, and it is structured as follows. Chapter 2 describes the phenomena of delamination under quasi-static loading and the different approaches used in the literature to deal with the problem. This information is essential to define the approach adopted: a finite element formulation of a cohesive element by means of the Cohesive Zone Model (CZM) approach. The literature reports a considerable number of approaches to the simulation of delamination under static or quasi-static loading. Several cohesive zone formulations present an inconsistency when the mode-ratio changes. Moreover, the application of the models present in the literature involve important mesh requirements to obtain accurate results. These mesh requirements are computationally heavy and can make the simulation of full-size components or structures intractable.

A thermodynamically consistent cohesive damage model that accounts for variations in the mode-ratio is presented in Chapter 3. The finite element discretization of the boundary value problem is also described. The model is validated with experimental data of standard tests and used to simulate the response of a skin-stringer configuration frequently used in aircraft structures.

Chapter 4 proposes a methodology to decrease the mesh size requirements in cohesive zone models. The chapter presents a methodology to use CZM in the simulation of delamination in large structures used in the industry where the requirements of extremely fine meshes cannot be met. By adjusting the parameters of the cohesive zone model, it is shown that it is possible to predict delamination accurately in specimens with and without pre-existing cracks by using coarser meshes than usual.

Part II comprises Chapters 5 and 6, and it is structured as follows. Chapter 5 first reviews the different approaches used to study the phenomena of fatigue. Then, the effect of fatigue delamination in composite materials is described and the different approaches present in the literature presented. This information is the basis for the definition of the approach adopted: a high-cycle fatigue model to simulate delamination under cyclic loading.

Chapter 6 describes the high-cycle fatigue model developed. The model is validated with experimental data, and the sensitivity of the model to load-dependent parameters like the stress ratio or the mode-ratio is analyzed.

The thesis is concluded in Chapter 7 with an overall assessment of its achievements and a discussion of possible avenues for future developments.

The models developed are implemented as a user-written element in the commercial finite element code ABAQUS©. The details of the code, some examples of input files and a User Manual are given in the Appendices.

Part I

Delamination under quasi-static loading

Chapter 2

Delamination in composite materials

2.1 Introduction

Delamination is one of the most common types of damage in laminated fibre-reinforced composites due to their relatively weak interlaminar strengths. Delamination can form during any moment of the life of the structure: manufacturing, transport, mounting and service.

2.1.1 Origin of delamination

According to Pagano and Schoeppner [3] the technological causes of the delamination can be grouped in two categories. The first category includes delamination due to curved sections, such as curved segments, tubular sections, cylinders and spheres, and pressurized containers. In all of these cases, the normal and shear stresses at the interface of two adjacent plies can originate the loss of adhesion and the initiation of an interlaminar crack.

The second category includes abrupt changes of section, such as ply drop-offs, unions between stiffeners and thin plates, free edges, and bonded and bolted joints.

A third category related to temperature and moisture effects can be added. The difference between the thermal coefficients of matrix and reinforcement results in differential contractions between the plies during the curing process of the laminate. The residual stresses originated by these differential contractions might be a source of delamination [4]. Similarly, the different expansion of the plies of the laminate during the absorption of moisture might be a cause for delamination [5].

Delamination may also originate during the manufacturing stage due to the shrinkage of the matrix during curing, or due to the formation of resin-rich areas that result from poor practices when laying the plies. [6, 7].

During service, delamination may arise under various circumstances, such as in the case of transverse concentrated loads caused by low velocity impacts. Impact is an important source of delamination in composite structures. Interlaminar cracks can originate from internal damage in the interface between adjacent plies as a consequence of impact, from the drop of a tool during production, mounting or repairing, or from ballistic impacts in military planes or structures.

2.1.2 Types of delamination

According to Bolotin [6, 7], two types of delamination can be considered: internal delaminations and near-surface delamination. Internal delamination originate in the inner ply interfaces of the laminate and can be due to the interaction of matrix cracks and ply interfaces. Delaminations originated by transverse matrix cracks in plies orthogonal to the tensile load are common examples of this type of delamination.

Internal delamination reduces considerably the load-capacity of composite structures. In particular, when compression loads are applied, the overall flexural behaviour of the laminate is significantly affected (as shown schematically in Figure 2.1). Although delamination separates the laminate in two parts, there is an interaction between the deformation of the one part of the laminate and the other. Due to this interaction, both parts of the laminate may deflect in a similar way.

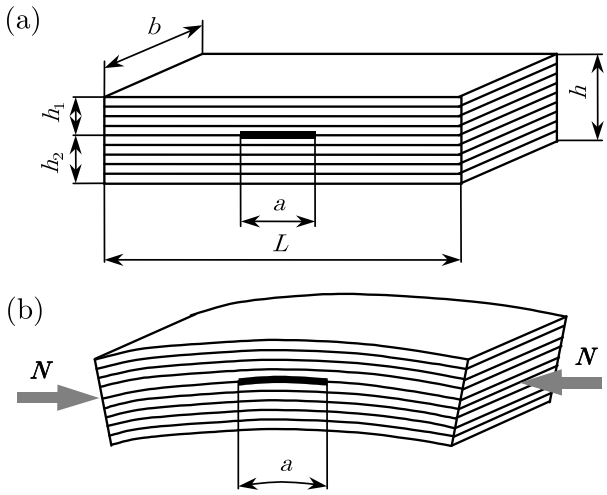

Figure 2.1: *Internal delamination: (a) disposition across the laminate and (b) effect on the overall stability (Figure from Bolotin [6]).*

Near-surface delaminations, as the name indicates, originate near the surface of the laminate and represent a more complex scenario than internal delaminations. The deformation of the delaminated part is less influenced by the deformation of the rest of the laminate. Therefore, the deformation of the near-surface delaminated part does not necessary follow the deformation of the rest of the laminate. Consequently, not only the growth of the near-surface delamination has to be taken into account but also its local stability. Bolotin [6, 7] classified the different types of near-surface delamination than can originate in plate composite components in different load conditions as shown in Figure 2.2.

After initiation, internal o r near-surface delaminations can propagate under either static or fatigue loads. In both cases, the reduction in strength and stability of the composite part to flexural loading is considerable. In addition, the delamination damage mode is particularly important for the structural integrity of composite structures because it is difficult to detect during inspection.

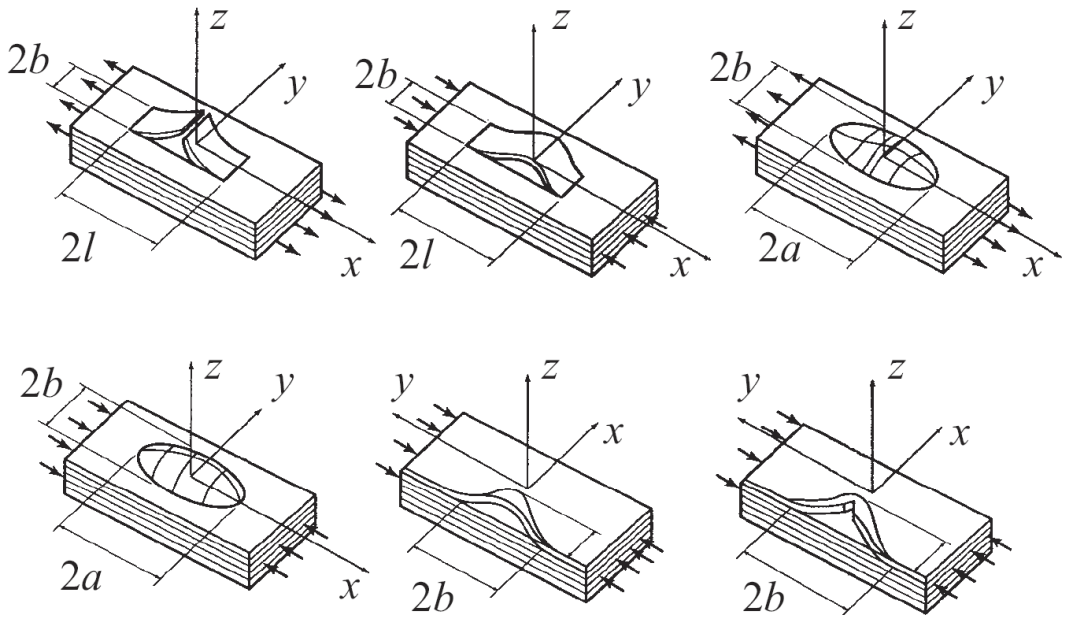

Figure 2.2: *Near-surface delamination: (a) open in tension; (b) closed in tension; (c) open buckled; (d) closed buckled; (e) edge buckled and (f) edge buckled with secondary crack (Figure from Bolotin [6]).*

2.2 Micromechanics of delamination

At the microscopic level, the growth of an interlaminar crack is preceded by the formation of a damage zone ahead of the crack tip. The size and shape at the deformation/damage zone is seen to be quite variable, depending on both the resin toughness and the state of stress (mode I, mode II, mode III or mixed-mode, see Figure 2.3). The damage zone ahead of the crack tip for mode II or mode III loading is greater than for mode I loading. A much slower decaying of the stress field ahead of the crack tip for the shear modes of loading is responsible for this difference. On the other hand, there are differences between systems with brittle or ductile matrices: the deformation/damaged zone for more brittle composites is much smaller.

For mode I loading in brittle systems, the zone ahead of the crack tip contains microcracks whose coalescence and growth results in crack advance. Sometimes,

crack advance occurs by fibre-matrix debonding before microcrack coalescence occurs. When debonding takes place, fibre bridging and fiber breakage are observed. For ductile systems, plastic deformation around the crack tip precedes crack advance. Crack advanc generally occurs by ductile tearing, but crack advance by interfacial debonding was also commonly observed in composites made with more ductile resins [8].

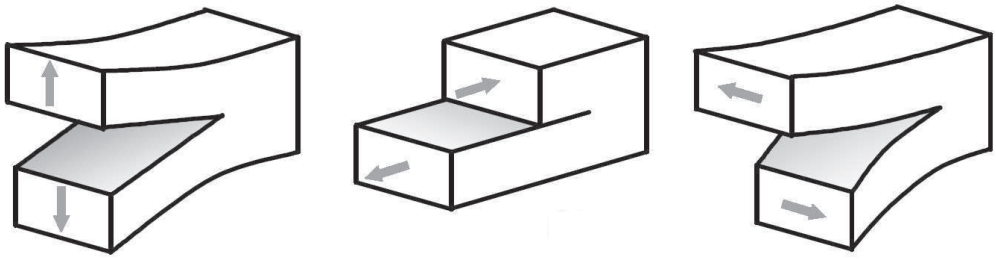

Figure 2.3: *Mode I, mode II, and mode III crack propagation modes.*

Shear mode delamination (mode II and/or mode III) of quasi-brittle systems occurs in a very distinctive way. Microcracks form from a considerable distance ahead of the crack tip, at a 45°-angle to the plane of the ply. These cracks grow until they reach the fibres, which bound the resin-rich region between plies. It sometimes appears that the cracks stop in the resin short of the nearest visible fiber. However there are certainly fibers just at the top or beneath the surface that are responsible for arresting these growing microcracks. Coalescence of these microcracks is required for macrocrack advance. This coalesce generally occurs at the fiber/matrix interface, giving a "corrugated roof appearance" along with the formation of "hackles" in the resin between fibers (see Figure 2.4). The fracture process for mode II delamination appears to be ductile rupture, with occasional fibre debonding.

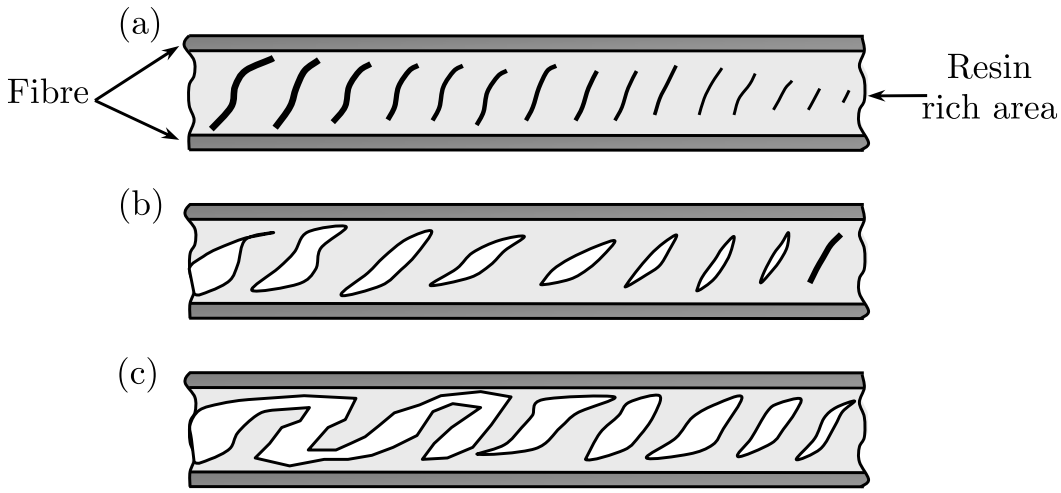

Figure 2.4: *Formation and growth of a mode II delamination at the ply interface: (a) microcrack formation ahead of the crack tip; (b) microcrack growth and opening and (c) microcrack coalescence accompanied by shear cusps [9].*

2.3 Approaches to delamination

Historically, the delamination mechanics was first studied by Obreimoff (1894-1981), a Soviet expert in the field of solid-state physics. In 1930, he published in an English journal a paper under the title "The Splitting Strength of Mica" [10]. Obreimoff estimated the specific work of interlaminar fracture, examining the detaching of a layer from a mica specimen under the action of a tearing force. The paper followed the series of pioneering papers by Griffith in 1920. From the early 1980's and up to the present day, the delamination mechanics has been a subject of ever-increasing interest. The number of studies in this field runs into thousands.

The procedures used for the numerical simulation of the delamination can be divided into two groups. The first group is based on the direct application of Fracture Mechanics, while the second formulates the problem within the framework of Damage Mechanics.

2.3.1 Fracture Mechanics approach

When other material non-linearities can be neglected, methods based on Linear Elastic Fracture Mechanics (LEFM) have been proven to be effective in predicting delamination growth. However, LEFM cannot be applied without an initial crack. In some situations, methods combining a stress analysis with a characteristic distance have been applied to predict the initiation of delamination [11, 12]. After delamination onset, LEFM can be used to predict delamination growth [13, 14]. Techniques such as the Virtual Crack Closure Technique (VCCT) [15]–[19], the J-integral method [20], the virtual crack extension [21] and stiffness derivative [22] have often been used to predict delamination growth. These techniques are used to calculate the components of the energy release rate. Delamination growth is predicted when a combination of the components of the energy release rate is equal to, or greater than, a critical value [23]. However, difficulties are also encountered when these techniques are implemented using finite element codes. The calculation of fracture parameters, e.g. stress intensity factors or energy release rates, requires nodal variable and topological information from the nodes ahead and behind the crack front. Such calculations can be done with some effort for a stationary crack, but can be extremely difficult when progressive crack propagation is involved.

Virtual Crack Closure Technique (VCCT)

The virtual crack closure technique is one of the most widely used procedures to predict crack propagation. This technique is based on Irwin's assumption that when a crack extends by a small amount, the energy released in the process is equal to the work required to close the crack to its original length. If the energy released per unit area is greater than or equal to the critical value, G_c, the crack will propagate. The mode I, mode II and mode III energy release rates, G_{I}, G_{II} and G_{III}, respectively, can be computed from the nodal forces and displacements obtained from the solution of a finite element model [18, 19].

In a finite element model such as shown in Figure 2.5, the energy released is the work done by the nodal forces required to close the crack tip, therefore:

$$G_{\mathrm{I}} = \frac{1}{2b\Delta a} F_{cd}^{y} \left(v_c - v_d\right) \tag{2.1}$$

$$G_{\mathrm{II}} = \frac{1}{2b\Delta a} F_{cd}^{x} \left(u_c - u_d\right) \tag{2.2}$$

$$G_{\mathrm{III}} = \frac{1}{2b\Delta a} F_{cd}^{z} \left(w_c - w_d\right) \tag{2.3}$$

where b is the specimen thickness, F_{cd}^{y}, F_{cd}^{x}, and F_{cd}^{z} are the magnitudes of nodal forces pairs at nodes c and d in the y,x and z direction, respecitvely. u_c, v_c, w_c and $u_d.v_d, w_d$ are the nodal displacements before nodes c and d are pulled together.

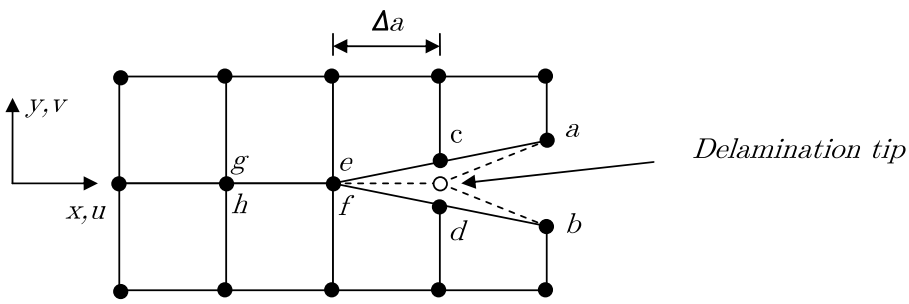

Figure 2.5: *Calculation of the energy release rate using Virtual Crack Closure Technique.*

The analysis can be done in two steps, using the first step to compute the values of the nodal forces F_{cd}^{y}, F_{cd}^{x} and F_{cd}^{z} necessary to hold the nodes c and d together, while the relative displacement components between nodes c and d are computed in the second step. However the analysis can be simplified using the assumption made by Rybicki and Kanninen [16], who suggested that the values of the nodal forces in equations (2.1), (2.2), and (2.3) can be replaced by the corresponding components of nodal forces F_{ef}^{y}, F_{ef}^{x} and F_{ef}^{z}.

After the calculation of $G_{\mathrm{I}}, G_{\mathrm{II}}$ and G_{III}, the total energy release rate reads:

$$G_T = G_{\mathrm{I}} + G_{\mathrm{II}} + G_{\mathrm{III}} \tag{2.4}$$

Crack propagation is predicted when the computed energy release rate is equal to the fracture toughness of the material, G_c:

$$G_T = G_c \tag{2.5}$$

One advantages of this form of calculation is that it is based on energy rather than stress. The main drawback of the VCCT technique is that it is based on the assumption of self-similar propagation, i.e. the forces F^i_{ef} and F^i_{cd} are the same. Therefore, crack initiation and the propagation of short cracks cannot be predicted.

only crack propagation could be predicted, regardless of crack initiation.

2.3.2 Cohesive or Damage Zone Models

Another approach for the numerical simulation of delamination can be developed within the framework of Damage Mechanics. Models formulated using Damage Mechanics are based on the concept of the cohesive crack model: a cohesive damage zone is developed near the crack front. The origin of the cohesive crack model goes back to Dugdale [24] who introduced the concept that stresses in the material are limited by the yield stress and that a thin plastic zone is generated in front of the notch. Barenblatt [25] introduced cohesive forces on a molecular scale in order to solve the problem of equilibrium in elastic bodies with cracks. Hillerborg et al. [26] proposed a model similar to Barenblatt's model, but where the concept of tensile strength was introduced. Hillerborg's model allowed for existing cracks to grow and, more importantly, also allowed for the initiation of new cracks.

Cohesive damage zone models relate tractions to displacement jumps at an interface where a crack may occur (see Figure 2.6). Damage initiation is related to the interfacial strength, i.e., the maximum traction τ^{o} in the traction-displacement jump

relation. When the area under the traction-displacement jump relation is equal to the fracture toughness G_c, the traction is reduced to zero and new crack surfaces are formed.

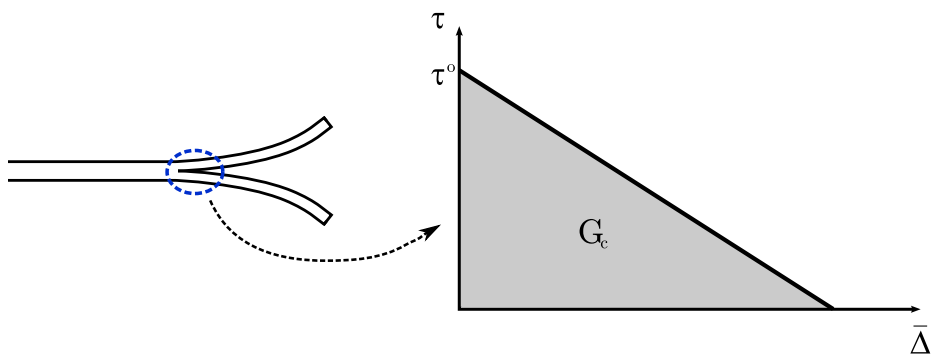

Figure 2.6: *Tractions in the cohesive zone ahead of the crack tip.*

The advantages of cohesive zone models are its simplicity and the unification of crack initiation and growth within one model. Although the cohesive damage models cannot be considered non-local damage models [27], they allow a mesh-independent representation of material softening, provided that the mesh is sufficiently refined. These aspects are discussed in more detail in Chapter 4.

Cohesive Zone Model formulations are more powerful than Fracture Mechanics approaches because they allow the prediction of both initiation and crack propagation, and thus, damage tolerance and strength analyses can be done with the same design tool.

Pure mode loading

Under pure mode I, mode II, or mode III loading, delamination initiation occurs when the corresponding interlaminar traction is equal to its respective maximum interfacial strength $(\tau_3^o, \tau_2^o, \tau_1^o)$

$$\tau_i = \tau_i^{\mathrm{o}} \tag{2.6}$$

Delamination propagation is predicted when the energy release rate (G_{I}, G_{II} or G_{III}) is equal the corresponding fracture toughness of the material (G_{Ic}, G_{IIc} or G_{IIIc}). Thus, equations (2.6) and (2.5) define the initiation and propagation criteria, respectively. The transition between the delamination initiation and delamination propagation is controlled by the constitutive equation.

Mixed-mode loading

For mixed-mode loading, the coupling effects between loading modes must be taken into account. For an undamaged interface, delamination starts when a scalar function of the interlaminar stresses reaches a limit. The conventional stress-based failure criterion is only suitable for predicting damage initiation:

$$\mathrm{f}_{initiation} = \mathrm{f}\left(\tau_i\right) - 1 = 0 \tag{2.7}$$

where $\mathrm{f}_{initiation}$ is the failure criterion and $\mathrm{f}\left(\tau_i\right)$ is a norm of the tractions. Few models take into account the interaction of the traction components in the prediction of damage onset. The models that account for the interaction of the traction components are usually based on Ye's criterion [28], using a quadratic interaction of the tractions:

$$\mathrm{f}_{initiation} = \left(\frac{\langle\tau_3\rangle}{\tau_3^o}\right)^2 + \left(\frac{\tau_2}{\tau_2^o}\right)^2 + \left(\frac{\tau_1}{\tau_1^o}\right)^2 - 1 = 0 \tag{2.8}$$

where $\langle\cdot\rangle$ is the MacAuley bracket defined as $\langle x\rangle = \frac{1}{2}\left(x + |x|\right)$.

The criterion for propagation is often formulated independently of the criterion for initiation. The failure criterion for delamination propagation can be expressed as:

$$\mathrm{f}_{propagation} = \mathrm{f}\left(G_i\right) - 1 = 0 \tag{2.9}$$

where $\mathrm{f}_{propagation}$ is a function of the pure mode fracture energies and $\mathrm{f}(G_i)$ is a norm of the energy release rates. There are different forms adopted in the literature to define the propagation criteria. One of these criteria is the power law expression:

$$\mathrm{f}_{propagation}(G_i) = \left(\frac{G_{\mathrm{I}}}{G_{\mathrm{I}}}\right)^{\alpha} + \left(\frac{G_{\mathrm{II}}}{G_{\mathrm{II}}}\right)^{\beta} + \left(\frac{G_{\mathrm{III}}}{G_{\mathrm{III}}}\right)^{\gamma} - 1 = 0 \tag{2.10}$$

where G_{I}, G_{II} or G_{III} are the individual components of energy release rate, and α, β, and γ are parameters to be fit with experimental data. The values $\alpha = \beta = \gamma = 1$ or $\alpha = \beta = \gamma = 2$ are frequently chosen when no experimental data is available. The values $\alpha = \beta = \gamma = 1$ correspond to a linear failure criterion, and $\alpha = \beta = \gamma = 2$ correspond to a quadratic failure criterion.

Kenane and Benzeggagh [29] proposed a failure criterion which, in some cases, fits experimental results more accurately:

$$\mathrm{f}_{propagation} = \frac{G_T}{G_c} - 1 = 0 \tag{2.11}$$

where G_T is obtained with Equation (2.4) and G_c is

$$G_c = G_{\mathrm{Ic}} + (G_{\mathrm{IIc}} - G_{\mathrm{Ic}}) \left(\frac{G_{\mathrm{I}} + G_{\mathrm{I}}}{G_T}\right)^{\eta} \tag{2.12}$$

where η is a parameter found by fitting Equation (2.12) to the experimental data. Kim [30] proposes a modification of Equation (2.13):

$$G_c = 2G_{\mathrm{Ic}} + (G_{\mathrm{IIc}} - G_{\mathrm{Ic}}) \left(\frac{G_{\mathrm{I}} + G_{\mathrm{I}}}{G_T}\right)^{\eta} \tag{2.13}$$

Numerical implementation of Cohesive Zone Model

Cohesive Zone formulations are well-suited to be implemented in finite element codes. However, the traction-displacement jump relation presented in Figure 2.6

has to be modified to be implemented in a Finite Element code by means of standard interface elements. An elastic path is introduced in the constitutive equation as shown in Figure 2.7 before damage initiation. This linear elastic part introduces a very high stiffness to the interface before damage initiation.

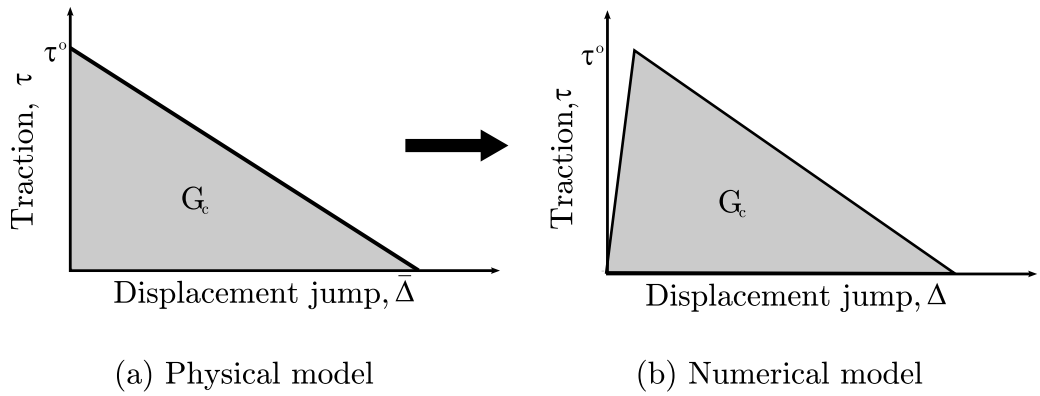

(a) Physical model (b) Numerical model

Figure 2.7: *Equivalence between the physical cohesive model and the numerical cohesive model.*

There are two main strategies in the literature to implement cohesive zone formulations: discrete interelement cracks and discrete intralement cracks.

In the first strategy, the crack extends between elements and remeshing is necessary when the crack path is not known in advance. This approach has been used to model cohesive crack growth in concrete [31]-[33] and to model crack growth in ductile materials [34, 35]. Xu et al. [36] and Camacho et al. [37] placed the cohesive zone as an interelement in between each pair of neighboring elements in the mesh. This idea is widely used in the simulation of delamination in multilayered materials using interface or so-called cohesive elements [38]-[49].

The intraelement approaches are based on the concept of the strong discontinuity approach [50]–[56]. It can be shown that the introduction of strong discontinuity kinematics in a continuum medium, ruled by continuum (stress–strain) constitutive equations with strain softening, induces the fulfillment of specific traction–separation

constitutive laws at a discrete set of propagating cohesive surfaces [57]. These formulations allow the incorporation of a discontinuous mode on an element level, by exploiting the partition-of-unity property of the finite element shape functions [58]. A crack is modeled as a jump in the displacement field of the continuum elements, the magnitude of the jump is determined by an extra set of degrees of freedom, which are added to existing nodes of the finite element mesh. Remmers et al. [59] used this approach to formulate a solid-like shell element for the simulation of delamination. However, the requirement of an extra set of degrees of freedom complicate the implementation of these formulations in commercial finite element codes.

Definition of the constitutive equation

The definition of the constitutive equation that relates tractions to displacement jumps at an interface can be done using a phenomenological or a mechanistic approach.

The mechanistic approach to define the constitutive equation uses methods that derive directly the constitutive equation. There exist several methods in the literature, using the direct tension test [60, 61], from measures using the J-integral and the final crack opening [62, 63] or using the fractal theory [64].

The phenomenological calibration of the constitutive equation is achieved using the results obtained in experimental tests. Constitutive equations are determined comparing the response of a test specimen (load-total displacement curve) with the results given with prediction models using different parameters. There are basically two groups of analysis to adjust the constitutive equation using experimental data [65]:

The first group are techniques that use a softening curve defined a prior by N parameters, which are best fitted by an optimization algorithm to the experimental data.

The second group uses characteristic points, or properties of the load-displacement curve (peak load or area under curve, for example). Several of such models have been

proposed. The simplest uses a bilinear constitutive equation [43]–[47]. In addition to the bilinear constitutive equation, there are different shapes of the constitutive equation formulated in the literature [34, 40, 43, 67] some of which are shown in Figure 2.8.

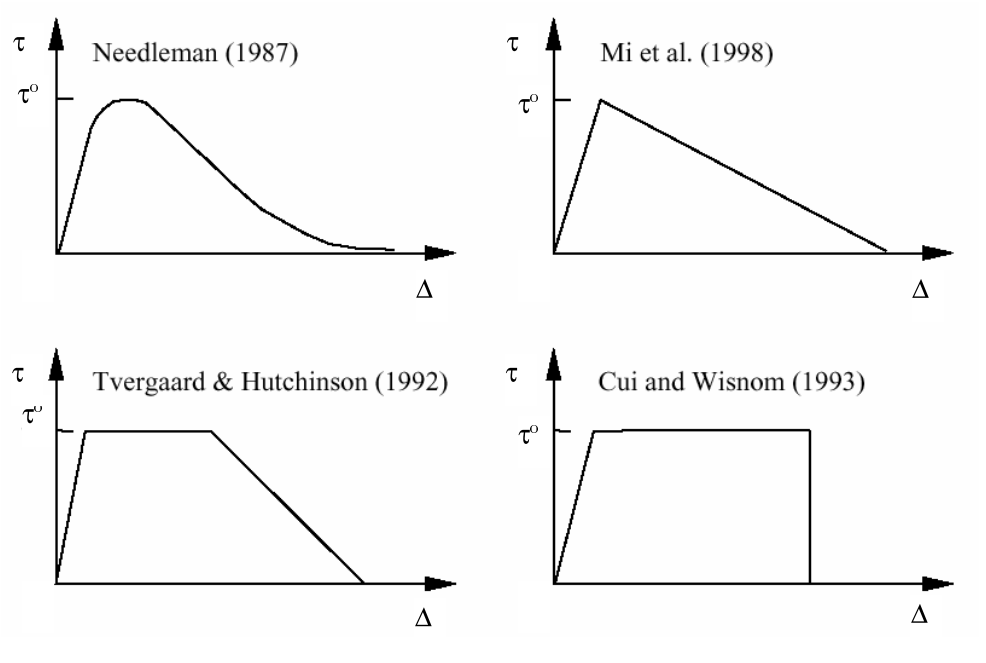

Figure 2.8: *Traction-relative displacement curves employed in various models in the literature (Figure from Zou et al.[66]).*

Alfano [68] investigated the influence of the shape of the constitutive law comparing a bilinear, trapezoidal, exponential and linear–parabolic laws under static tests. For a typical double-cantilever-beam test, the solution was found to be practically independent of the shape of the interface law. An influence of the interface law was found on the algorithmic numerical performance and on the degree of accuracy achieved; in particular, the trapezoidal law gave the worst results both in terms of numerical stability and in terms of convergence of the finite-element solution to the exact solution. The exponential law was found to be optimal in terms of accuracy while the bilinear law represented the best compromise between computational cost and accuracy.

Chapter 3

Variable mode-ratio interface damage model

3.1 Introduction

It was shown in the previous chapter that Cohesive Zone Models (CZM) are suitable to simulate delamination because they can be used for both damage-tolerance and strength analysis. To become an eficient and robust design tool, the cohesive zone model formulation needs to predict the mode-ratio of crack propagation accurately. It is important to control the energy dissipation during delamination growth in order to avoid the restoration of the cohesive state, i.e., it is necessary to assure that the model satisfies the Clausius-Duhem inequality even while the mode-ratio changes during crack growth. There are several models in the literature that can be used under constant mode-ratio conditions [43, 45]-[47, 69]-[74]. However, the models proposed generally do not satisfy the Clausius-Duhem inequality under variable mode loading. Most of the models cited above define the damage threshold parameter as the maximum displacement. This assumption may lead to the violation of the Clausius-Duhem inequality when the crack grows in a varying mode.

The restoration of the cohesive state when the mode changes is illustrated in Fig-

ure 3.1. This Figure represents the traction (τ)-relative displacement (Δ) relation for two different mode-ratios, $G_{\mathrm{II}}/\left(G_{\mathrm{II}}+G_{\mathrm{I}}\right)=A$ (Figure 3.1 a)) and $G_{\mathrm{II}}/\left(G_{\mathrm{II}}+G_{\mathrm{I}}\right)=B$ (Figure 3.1 b)), where G_{I} and G_{II} are the components of the energy release rate. If the mode-ratio changes from A to B during delamination growth, there is a restoration of the cohesive state. This effect is clearly inconsistent with the thermodynamical principles.

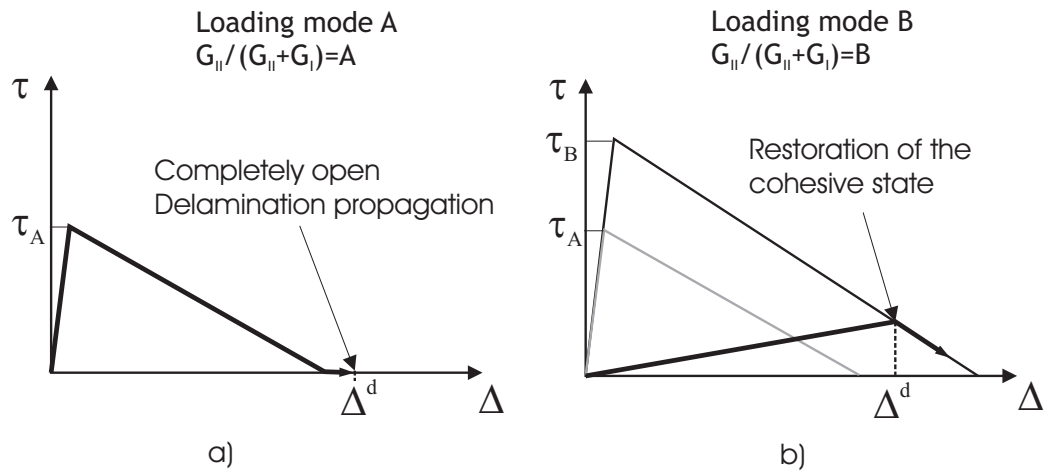

Figure 3.1: *Restoration of the cohesive state for delamination propagation under variable mode-ratio.*

A damage model for the simulation of delamination under variable mode is presented in this thesis. A new delamination initiation criterion is proposed in order to ensure the consistency of energy dissipation rate under variable mode-ratio. The delamination onset criterion stems from the expression of the critical energy release rate for delamination propagation under mixed-mode loading proposed by Benzeggagh and Kenane [29].

This chapter is structured as follows: first, the formulation of the damage model for the simulation of delamination onset and growth model is presented. The finite

element discretization of the boundary value problem is described. Finally, the numerical predictions are compared with experimental results obtained in composite test specimens and composite structural components.

3.2 Model for delamination onset and propagation

The boundary value problem, the kinematic equations, and the constitutive relations are presented for the formulation of the model for delamination onset and delamination propagation.

3.2.1 Boundary value problem

Consider a domain Ω, as shown in Figure 3.2(a), containing a crack Γ_c. The part of the crack on which a cohesive law is active is denoted by Γ_{coh} and is called the fracture process zone (FPZ).

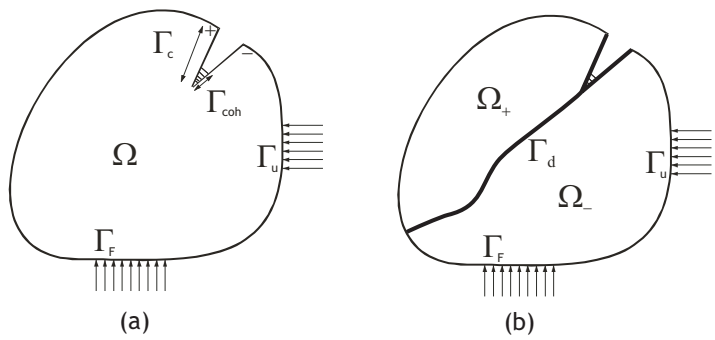

Figure 3.2: *Body Ω crossed by a material discontinuity Γ_d in the undeformed configuration.*

Prescribed tractions, t_i, are imposed on the boundary Γ_F, whereas prescribed displacements are imposed on Γ_u. The stress field inside the domain, σ_{ij}, is related

to the external loading and the closing tractions τ_j^+, τ_j^- in the cohesive zone through the equilibrium equations:

$$\sigma_{ij,j} + \rho b_i = 0 \text{ in } \Omega \tag{3.1}$$

$$\sigma_{ij} n_j = t_i \text{ on } \Gamma_F \tag{3.2}$$

$$\sigma_{ij} n_j^+ = \tau_i^+ = -\tau_i^- = -\sigma_{ij} n_j^- \text{ on } \Gamma_{coh} \tag{3.3}$$

where b_i are the body forces, ρ is the density of the material, and n_j is the vector normal to the surface.

3.2.2 Kinematics of the interfacial surface

To develop the necessary kinematic relationships, consider the crack Γ_c shown in Figure 3.2(a) as part of a material discontinuity, Γ_d, which divides the domain Ω into two parts, Ω_+ and Ω_- (Figure 3.2(b)).

The displacement jump across the material discontinuity Γ_d, $[\![u_i]\!]$, can be written as:

$$[\![u_i]\!] = u_i^+ - u_i^- \tag{3.4}$$

where $u_i^\pm$ denotes the displacement of the points on the surface of the material discontinuity Γ_d of the parts $\Omega_\pm$ of the domain.

The fundamental problem introduced by the interfacial surface Γ_d is how to express the virtual displacement jumps associated to the surfaces $\Gamma_{d^\pm}$ as a function of the virtual displacements. Consider a three-dimensional space with Cartesian coordinates X_i, $i = 1, 2, 3$. Let the Cartesian coordinates $x_i^\pm$ describe the position of the upper and lower surfaces $\Gamma_{d^\pm}$ in the deformed configuration. Considering Figure 3.3, any material point on $\Gamma_{d^\pm}$ in the deformed configuration is related to its undeformed configuration through:

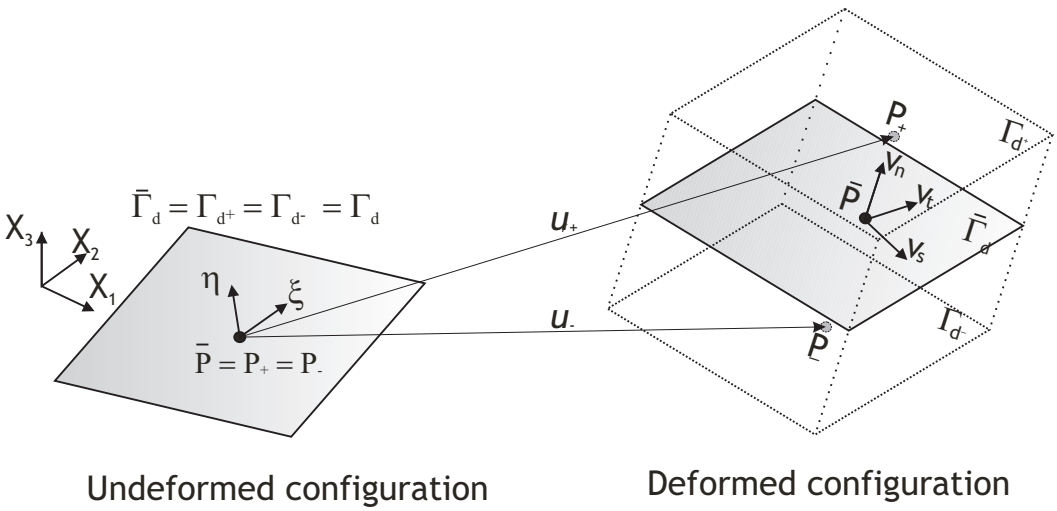

Figure 3.3: *Interfacial surface deformation.*

$$x_i^{\pm} = X_i + u_i^{\pm} \tag{3.5}$$

where $u_i^{\pm}$ are the displacements with respect to the fixed Cartesian coordinate system. The coordinates $\bar{x}_i$ of the midsurface can be written as [76]:

$$\bar{x}_i = X_i + \frac{1}{2}\left(u_i^{+} + u_i^{-}\right) \tag{3.6}$$

The components of the displacement jump vector are evaluated at the midsurface $\bar{\Gamma}_d$, which is coincident with Γ_d in the undeformed configuration (see Figure 3.3). The midsurface coordinate gradients define the components of the two vectors, v_{η_i} and v_{ξ_i}, that define the tangential plane at a given point, $\bar{P}$:

$$v_{\eta_i} = \bar{x}_{i,\eta} \tag{3.7}$$

$$v_{\xi_i} = \bar{x}_{i,\xi} \tag{3.8}$$

where η, ξ are curvilinear coordinates on the surface $\bar{\Gamma}_d$. Although v_{η_i} and v_{ξ_i} are generally not orthogonal to each other, their vector product defines a surface normal. Therefore, the local normal coordinate vector is obtained as:

$$\mathbf{v}_n = \mathbf{v}_\xi \times \mathbf{v}_\eta \left\| \mathbf{v}_\xi \times \mathbf{v}_\eta \right\|^{-1} \tag{3.9}$$

The tangential coordinates are then obtained as:

$$\mathbf{v}_s = \mathbf{v}_\xi \left\| \mathbf{v}_\xi \right\|^{-1} \tag{3.10}$$

$$\mathbf{v}_t = \mathbf{v}_n \times \mathbf{v}_s \tag{3.11}$$

The components of $\mathbf{v}_n, \mathbf{v}_s$ and $\mathbf{v}_t$ represent the direction cosines of the local coordinate system in the global coordinate system at a material point $\bar{P} \in \bar{\Gamma}_d$. The direction cosines define an orthogonal rotation tensor Θ_{mi} relating the local coordinate system to the fixed coordinate system.

Using the rotation tensor, the normal and tangential components of the displacement jump tensor expressed in terms of the displacement field in global coordinates are:

$$\Delta_m = \Theta_{mi} \left[\!\left[u_i \right]\!\right] \tag{3.12}$$

where Δ_m is the displacement jump tensor in the local coordinate system.

3.2.3 Constitutive laws

A constitutive law relating the cohesive tractions, τ_j, to the displacement jump in the local coordinates, Δ_i, is required for modeling the behavior of the material discontinuity. The constitutive laws in the material discontinuity may be formally written as:

$$\tau_j = \tau \left(\Delta_i \right) \tag{3.13}$$

$$\dot{\tau}_j = D_{ji}^{\tan} \dot{\Delta}_i \tag{3.14}$$

where $D_{ji}^{\tan}$ is the constitutive tangent stiffness tensor.

A new constitutive model relating the displacement jumps to the tractions, and based on Damage Mechanics is proposed. The model follows the general formulation of Continuum Damage Models proposed by Simo and Ju [77, 78] and Mazars [79].

The free energy per unit surface of the interface is defined as:

$$\psi\left(\Delta, \mathsf{d}\right) = \left(1 - \mathsf{d}\right)\psi^{0}\left(\Delta\right) \tag{3.15}$$

where d is a scalar damage variable, and ψ^0 is a convex function in the displacement jump space defined as:

$$\psi^{0}\left(\Delta\right) = \frac{1}{2}\Delta_i D_{ij}^{0}\Delta_j \qquad i = 1, 3; \quad j = 1, 3 \tag{3.16}$$

Negative values of Δ_3 do not have any physical meaning because interpenetration is prevented by contact. Therefore, a modification of Equation (3.15) is proposed to prevent interfacial penetration of the two adjacent layers after complete decohesion. The expression for the free energy proposed is:

$$\psi\left(\Delta, \mathsf{d}\right) = \left(1 - \mathsf{d}\right)\psi^{0}\left(\Delta_i\right) - \mathsf{d}\psi^{0}\left(\delta_{3i}\left\langle -\Delta_3\right\rangle\right) \tag{3.17}$$

where $\langle\cdot\rangle$ is the MacAuley bracket defined as $\langle x\rangle = \frac{1}{2}\left(x + |x|\right)$ and δ_{ij} is the Kronecker delta. The constitutive equation for the interface is obtained by differentiating the free energy with respect to the displacement jumps:

$$\tau_i = \frac{\partial\psi}{\partial\Delta_i} = \left(1 - \mathsf{d}\right)D_{ij}^{0}\Delta_j - \mathsf{d}D_{ij}^{0}\delta_{3j}\left\langle -\Delta_3\right\rangle \tag{3.18}$$

The undamaged stiffness tensor, D_{ij}^{0}, is defined as:

$$D_{ij}^{0} = \delta_{ij}K \tag{3.19}$$

where the scalar parameter K is a penalty stiffness. The constitutive equation can be written in Voigt notation as:

$$\tau = \begin{Bmatrix} \tau_1 \\ \tau_2 \\ \tau_3 \end{Bmatrix} = (1 - \mathsf{d})\, K \begin{Bmatrix} \Delta_1 \\ \Delta_2 \\ \Delta_3 \end{Bmatrix} - \mathsf{d}K \begin{Bmatrix} 0 \\ 0 \\ \langle -\Delta_3 \rangle \end{Bmatrix} \tag{3.20}$$

The model must ensure positive energy dissipation during damage evolution. The specific energy dissipated during the damage evolution, Ξ , is represented in Figure 3.4 for single-mode loading and can be obtained from:

$$\Xi = \int_t^{t+1} -\frac{\partial \psi}{\partial \mathsf{d}} \dot{\mathsf{d}} dt \geq 0 \tag{3.21}$$

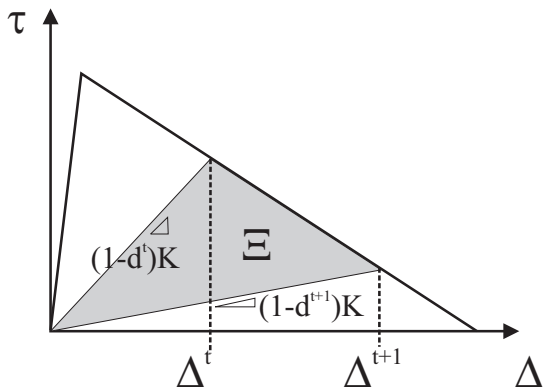

Figure 3.4: *Energy dissipation during damage evolution.*

The model defined by Equation (3.18) is fully determined if the value of the damage variable d is evaluated at every time step of the deformation process. For that purpose, it is necessary to define a suitable norm of the displacement jump tensor, a damage criterion, and a damage evolution law, as will be described in the following sections.

Norm of the displacement jump tensor

The norm of the displacement jump tensor is denoted as λ and is also called *equivalent displacement jump norm.* It is used to compare different stages of the displacement jump state so that it is possible to define such concepts as 'loading', 'unloading' and 'reloading'. The equivalent displacement jump is a non-negative and continuous function, defined as:

$$\lambda = \sqrt{\langle \Delta_3 \rangle^2 + (\Delta_{\text{shear}})^2} \tag{3.22}$$

where Δ_3 is the displacement jump in mode I, i.e., normal to midplane, and Δ_{shear} is the Euclidean norm of the displacement jump in mode II and in mode III:

$$\Delta_{\text{shear}} = \sqrt{(\Delta_1)^2 + (\Delta_2)^2} \tag{3.23}$$

Damage criterion

The damage criterion is formulated in the displacement jump space. The form of this criterion is:

$$F\left(\lambda^t, r^t\right) := \lambda^t - r^t \leq 0 \qquad \forall t \geq 0 \tag{3.24}$$

where t indicates the actual time and r^t is the damage threshold for the current time. If r^0 denotes the initial damage threshold, then $r^t \geq r^0$ at every point in time. Damage initiation is produced when the displacement jump norm, λ, exceeds the initial damage threshold, r^0, which is a material property.

A fully equivalent expression for Equation (3.24) that is more convenient for algorithmic treatment is [80]:

$$\bar{F}\left(\lambda^t, r^t\right) := \mathsf{G}\left(\lambda^t\right) - \mathsf{G}\left(r^t\right) \leq 0 \qquad \forall t \geq 0 \tag{3.25}$$

where $\mathsf{G}(\cdot)$ is a suitable monotonic scalar function ranging from 0 to 1. The function $\mathsf{G}(\cdot)$ will define the evolution of the damage value, and will be presented in the following section.

Damage evolution law

The evolution laws for the damage threshold and the damage variable must be defined in the damage model. These laws are defined by the rate expressions [77, 78, 79]:

$$\dot{r} = \dot{\mu} \tag{3.26}$$

$$\dot{\mathsf{d}} = \dot{\mu}\frac{\partial \bar{F}\left(\lambda, r\right)}{\partial \lambda} = \dot{\mu}\frac{\partial \mathsf{G}\left(\lambda\right)}{\partial \lambda} \tag{3.27}$$

where $\dot{\mu}$ is a damage consistency parameter used to define loading-unloading conditions according to the Kuhn-Tucker relations:

$$\dot{\mu} \geq 0 \quad ; \quad \bar{F}\left(\lambda^t, r^t\right) \leq 0 \quad ; \quad \dot{\mu}\bar{F}\left(\lambda^t, r^t\right) = 0 \tag{3.28}$$

From the previous equations, it is easy to prove that the evolution of the internal variables can be integrated explicitly [77]:

$$r^t = \max\left\{r^0, \max_s \lambda^s\right\} \qquad 0 \leq s \leq t \tag{3.29}$$

$$\mathsf{d}^t = \mathsf{G}\left(r^t\right) \tag{3.30}$$

which fully describes evolution of the internal variables for any loading-unloading-reloading situation. The scalar function $\mathsf{G}\left(\cdot\right)$ defines the evolution of the damage value. Using a bilinear constitutive equation, for a given mode-ratio, β, the function G is defined as:

$$\mathsf{G}\left(\lambda\right) = \frac{\Delta^f\left(\lambda - \Delta^o\right)}{\lambda\left(\Delta^f - \Delta^o\right)} \tag{3.31}$$

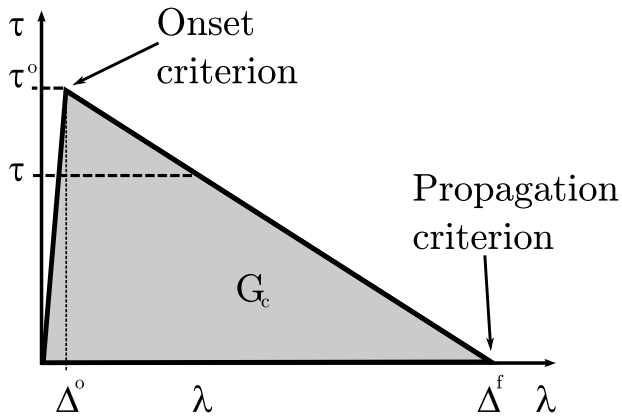

Figure 3.5: *A bilinear constitutive equation for the cohesive element for a mixed-mode loading situation.*

Equation (3.31) defines the damage evolution law by means of a bilinear constitutive equation (see Figure 3.5), where Δ^o is the onset displacement jump, and it is equal to the initial damage threshold r^0. The initial damage threshold is obtained from the formulation of the initial damage surface or initial damage criterion. Δ^f is the final displacement jump, and it is obtained from the formulation of the propagation surface or propagation criterion.

It is therefore necessary to establish the delamination onset and propagation surfaces for the complete definition of the damage model. Delamination onset and propagation surfaces and the damage evolution law fully define the constitutive equations.

The law proposed here is a bilinear relation between the tractions and the displacement jumps [43, 47, 82]. The bilinear law is the most commonly used cohesive law due to its simplicity. One drawback of the bilinear law is that the traction-displacement jump relation is discontinuous at the peak value of the traction. The discontinuity in the traction-displacement jump relation can be avoided using continuous functions. However, even for such continuous functions, the discontinuity is unavoidable when modeling loading-unloading cycles.

For a given mode-ratio, β, defined as:

$$\beta = \frac{\Delta_{\text{shear}}}{\Delta_{\text{shear}} + \langle \Delta_3 \rangle} \tag{3.32}$$

the bilinear constitutive equation is defined by a penalty parameter, K, the damage value, d, the mode damage initiation, Δ^o, and the total decohesion parameter, Δ^f. These last two values are given by the formulation of the onset and the propagation criterion which takes into account the interaction between different modes, and their value depends on the mode-ratio β. The penalty parameter K assures a stiff connection between two neighboring layers before delamination initiation. The penalty parameter should be large enough to provide a reasonable stiffness but small enough to avoid numerical problems, such as spurious traction oscillations [83], in a finite element analysis.

Propagation criterion

The criteria used to predict delamination propagation under mixed-mode loading conditions are usually established in terms of the components of the energy release rate and fracture toughness. It is assumed that when the energy release rate, G, exceeds the critical value, the critical energy release rate G_c, delamination grows.

The most widely used criterion to predict delamination propagation under mixed-mode loading, the "power law criterion" is normally established in terms of a linear or quadratic interaction between the energy release rates [84]. However, Camanho et al. [47] have shown that the expression proposed by Benzeggagh and Kenane [29] for the critical energy release rate for a mode-ratio is more accurate for epoxy and PEEK composites. Delamination growth is produced when the total energy release rate G is greater or equal than the critical value G_c:

$$G \geq G_c \tag{3.33}$$

The energy release rate under mixed-mode loading is $G = G_{\text{I}} + G_{\text{shear}}$ where

$G_{\text{shear}} = G_{\text{II}} + G_{\text{III}}$ is the energy release rate for shear loading proposed by Li [86, 87].

The propagation surface in the displacement jump space is defined through the final displacements, which are obtained from the pure mode fracture toughness (G_{IC}, G_{IIC}, G_{IIIC}) considering that the area under the traction-displacement jump curves is equal to the corresponding fracture toughness, i.e.:

$$G_c = \frac{1}{2} K \Delta^o \Delta^f \tag{3.34}$$

Using Equation (3.34) in Equation (2.13) the propagation criterion is obtained in the displacement jump space as:

$$\Delta^f = \frac{\Delta_3^o \Delta_3^f + \left(\Delta_{\text{shear}}^o \Delta_{\text{shear}}^f - \Delta_3^o \Delta_3^f\right) \left(\frac{G_{\text{shear}}}{G_{\text{T}}}\right)^\eta}{\Delta^o} \tag{3.35}$$

where Δ_3^o and Δ_{shear}^o are the pure mode onset displacement jumps and Δ_3^f and Δ_{shear}^f are the pure mode final displacement jumps. It is necessary to obtain the ratio $\frac{G_{\text{shear}}}{G_{\text{T}}}$ to fully define the final displacement jump. For a given mode-ratio, β, the energy release rates are obtained from:

$$G_{\text{I}} = \frac{1}{2} K \left(\Delta_3^o(\beta)\, \Delta_3^f(\beta) - \Delta_3 \Delta_3^f(\beta)\right) \tag{3.36}$$

$$G_{\text{shear}} = \frac{1}{2} K \left(\Delta_{\text{shear}}^o(\beta)\, \Delta_{\text{shear}}^f(\beta) - \Delta_{\text{shear}} \Delta_{\text{shear}}^f(\beta)\right) \tag{3.37}$$

where $\Delta_{\text{shear}}^o(\beta)$ and $\Delta_3^o(\beta)$ are respectively the shear and normal displacement jump corresponding to the onset of softening under mixed-mode loading, $\Delta_{\text{shear}}^f(\beta)$ and $\Delta_3^f(\beta)$ are the shear and normal displacement jump corresponding to the total decohesion under mixed-mode loading, and Δ_{shear} and Δ_3 are the components of the current displacement jump.

From (3.32):

$$\Delta^o_{\text{shear}}(\beta) = \Delta^o_3(\beta)\frac{\beta}{1-\beta} \tag{3.38}$$

$$\Delta^f_{\text{shear}}(\beta) = \Delta^f_3(\beta)\frac{\beta}{1-\beta} \tag{3.39}$$

$$\Delta_{\text{shear}} = \Delta_3\frac{\beta}{1-\beta} \tag{3.40}$$

Using equations (3.38), (3.39), and (3.40) in (3.36) and (3.37), the ratio between $\frac{G_{\text{shear}}}{G_{\text{T}}}$ can be established in terms of β. Since the ratio $\frac{G_{\text{shear}}}{G_{\text{T}}}$ is only a function of the mode-ratio β, henceforward this ratio is named as B:

$$B = \frac{G_{\text{shear}}}{G_{\text{T}}} = \frac{\beta^2}{1+2\beta^2-2\beta} \tag{3.41}$$

Initial damage surface

Under pure mode I, mode II or mode III loading, delamination onset occurs when the corresponding interlaminar traction exceeds its respective maximum interfacial strength, $\tau^o_3, \tau^o_2, \tau^o_1$. Under mixed-mode loading, the interaction between modes must be taken into account. Few models take into account the interaction of the traction components in the prediction of damage onset. As explained in previous chapter, the models that account for the interaction of the traction components are usually based on Ye's criterion [28], using the quadratic interaction of the tractions given in Equation (2.10). However, experimental data for the initiation of delamination under mixed-mode loading is not readily available and, consequently, failure criteria that can predict the initiation have not been fully validated.

The criterion for propagation is often formulated independently of the criterion for initiation. In this work, a link between propagation and initiation is proposed. Since delamination is a fracture process, the interaction between modes in the initiation criterion is assumed to be the same as for the propagation criterion. The initiation criterion evolves from the propagation criterion and the damage evolution law. The isodamage surface for a damage value equal to 1 corresponds to the propagation surface obtained from Equation (2.13). Then, the isodamage surface for a

damage value equal to 0 is the initial damage surface. With these assumptions, the criterion for delamination initiation proposed here is:

$$(\tau^o)^2 = (\tau_3)^2 + (\tau_1)^2 + (\tau_2)^2 = (\tau_3^o)^2 + \left((\tau_{\text{shear}}^o)^2 - (\tau_3^o)^2\right) B^\eta \tag{3.42}$$

In the displacement jump space, the criterion becomes:

$$(\Delta^o)^2 = (\Delta_3)^2 + (\Delta_1)^2 + (\Delta_2)^2 = (\Delta_3^o)^2 + \left((\Delta_{\text{shear}}^o)^2 - (\Delta_3^o)^2\right) B^\eta \tag{3.43}$$

The initiation criterion developed here and summarized by Equation (3.42) is compared with Ye's criterion and with a maximum traction criterion that does not take into account interaction between the tractions.

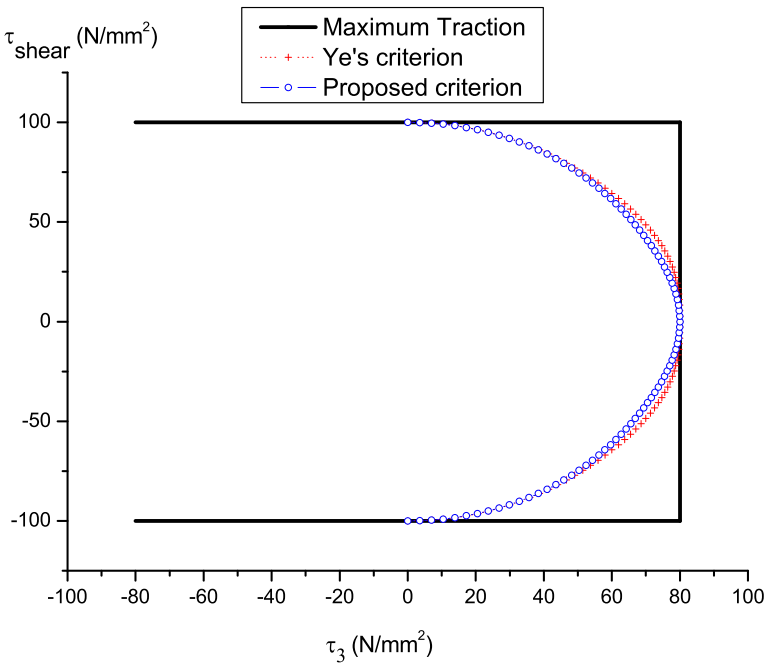

Figure 3.6: *Comparison between Ye's criterion, a maximum traction criterion and the new proposed criterion.*

The surfaces obtained by the different criteria are represented in Figure 3.6 for a material with the properties given in Table 3.1. The values predicted by the new criterion are very close to Ye's criterion, which has been successfully used in previous investigations [47].

The present formulation ensures a smooth transition for all mode ratios between the initial damage surface and the propagation surface through damage evolution. If the loading mode changes, the formulation avoids the restoration of the cohesive state and ensures that the energy dissipation is always positive.

The isodamage surfaces between the damage initiation surface and the propagation surface, for positive values of displacement jumps, are represented in Figure 3.7 using the material properties given in Table 3.1.

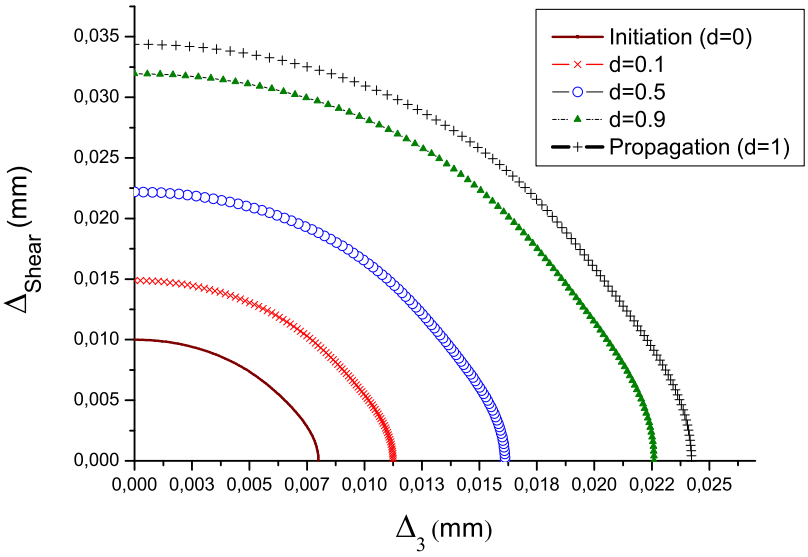

Figure 3.7: *Isodamage curves in the relative displacements space.*

3.2.4 Formulation of the constitutive tangent tensor

The constitutive tangent tensor needs to be defined for the numerical implementation of the proposed model. The constitutive tangent tensor is obtained from the differentiation of the secant Equation (3.18):

$$\dot{\tau}_i = D_{ij}\dot{\Delta}_j - \delta_{ij}K\left[1 + \delta_{3j}\frac{\langle -\Delta_j \rangle}{\Delta_j}\right]\Delta_j\dot{\mathsf{d}} \tag{3.44}$$

where D_{ij} is defined as:

$$D_{ij} = \delta_{ij}K\left[1 - \mathsf{d}\left(1 + \delta_{3j}\frac{\langle -\Delta_j \rangle}{\Delta_j}\right)\right] \tag{3.45}$$

Using the definition of the initiation and propagation surfaces proposed in the previous subsection, the final displacement jump Δ^f and the onset displacement jump Δ^o are mode dependent. Therefore, the function $\mathsf{G}(\lambda)$ used to define the evolution of the damage variable $\dot{\mathsf{d}}$, depends on the mode-ratio β. This means that the evolution of the damage variable with the mode-ratio needs to be derived. However, in most practical analyses of real structures the variation of the mode-ratio is gradual and very slow and, consequently, it is assumed that the variations of the onset and final displacement jump are not significant with respect to the time increment taken. Therefore, the evolution of the damage variable $\dot{\mathsf{d}}$ given by Equations (3.27) and (3.28) can be re-written as:

$$\dot{\mathsf{d}} = \begin{cases} \dot{\mathsf{G}}(\lambda) = \frac{\partial \mathsf{G}(\lambda)}{\partial \lambda}\dot{\lambda} & , r < \lambda < \Delta^f \\ 0 & , r > \lambda \text{ or } \Delta^f < \lambda \end{cases} \tag{3.46}$$

where the variation of the function G is from (3.31):

$$\frac{\partial \mathsf{G}(\lambda)}{\partial \lambda} = \frac{\Delta^f \Delta^o}{\Delta^f - \Delta^o}\frac{1}{\lambda^2} \tag{3.47}$$

The evolution of the displacement norm is obtained from Equation (3.22):

$$\dot{\lambda} = \frac{\partial \lambda}{\partial \Delta_k} \dot{\Delta}_k = \frac{\Delta_k}{\lambda} \left(1 + \delta_{3k} \frac{\langle -\Delta_k \rangle}{\Delta_k} \right) \dot{\Delta}_k \tag{3.48}$$

Using Equations (3.46) through (3.48), Equation (3.44) can be written as:

$$\dot{\tau}_i = D_{ij}^{tan} \dot{\Delta}_j \tag{3.49}$$

$$D_{ij}^{\tan} = \begin{cases} \left\{ D_{ij} - K \left[1 + \delta_{3j} \frac{\langle -\Delta_j \rangle}{\Delta_j} \right] \left[1 + \delta_{3i} \frac{\langle -\Delta_i \rangle}{\Delta_i} \right] H \Delta_i \Delta_j \right\} & , r < \lambda < \Delta^f \\ D_{ij} & , r > \lambda \text{ or } \Delta^f < \lambda \end{cases} \tag{3.50}$$

where H is a scalar value given by:

$$H = \frac{\Delta^f \Delta^o}{\Delta^f - \Delta^o} \frac{1}{\lambda^3} \tag{3.51}$$

3.3 Finite element discretization - computational model

To transform the strong form of the boundary value problem into a weak form better suited for finite element computations, the velocities v_i must belong to the set $\mathcal{U}$ of the kinematically admissible velocity field which allows for discontinuous velocities across the boundary Γ_d of the delamination.

The spaces for the test functions and trial functions are defined as:

$$\delta v_i (\mathbf{X}) \in \mathcal{U}_0, \quad \mathcal{U}_0 = \left\{ \delta v_i | \delta v_i \in C^0 (\mathbf{X}), \delta v_i = 0 \ \ on \ \ \Gamma_{v_i} \right\} \tag{3.52}$$

$$v_i (\mathbf{X}, t) \in \mathcal{U}, \quad \mathcal{U} = \left\{ v_i | v_i \in C^0 (\mathbf{X}), v_i = \bar{v}_i \ \ on \ \ \Gamma_{v_i} \right\} \tag{3.53}$$

The space of velocities in $\mathcal{U}$ are the kinematically admissible velocities or compatible velocities. The space $\mathcal{U}$ satisfies the continuity conditions required for compatibility and the displacement boundary conditions.

The weak form of the momentum equation (Equation 3.1) is obtained as:

$$\sum_{\Omega_\pm} \int_{\Omega_\pm} \left(\frac{\partial \sigma_{ij}}{\partial x_j} + \rho b_i \right) \delta v_i d\Omega_\pm = 0 \ \forall v_i \in \mathcal{U} \tag{3.54}$$

Using the decomposition of the velocity gradient and the traction continuity condition, the weak form of the momentum equation in an updated Lagrangian formulation is obtained as:

$$\begin{aligned} \int_{\Gamma_d} t_i \delta \left[\!\left[v_i \right]\!\right] d\Gamma_d + \sum_{\Omega_\pm} \int_{\Omega_\pm} \delta D_{ij} \sigma_{ij} d\Omega_\pm \quad &= \\ \sum_{\Gamma_\pm} \int_{\Gamma_\pm} n_j \left(\delta v_i \sigma_{ji} \right) d\Gamma_\pm + \sum_{\Omega_\pm} \int_{\Omega_\pm} \delta v_i \rho b_i d\Omega_\pm \quad \forall v_i \quad &\in \quad \mathcal{U} \end{aligned} \tag{3.55}$$

where t_i is the traction tensor, σ_{ij} is the Cauchy stress tensor, and D_{ij} is the rate of deformation tensor. From Equation (3.55), it is clear that the tractions occurring at the cohesive interface are work-conjugate with the displacement jumps.

The discretization of the domain is performed by the discretization of the whole domain Ω with standard volume elements. However, the surfaces surrounding the potential delamination Γ_d are discretized with cohesive elements [47]. The discretized formulation is divided in the two domains considering no formal coupling between the continuous and the discontinuous parts of the deformation in the expression for the free energy of the interface [88].

3.3.1 Discretization of the interfacial surface

The displacements and displacement gradients for the cohesive elements are approximated as:

$$u_i|_{\Omega_e} = N_K^e q_{Ki}^e \tag{3.56}$$

$$\left[\!\left[u_i \right]\!\right] |_{\Omega_e} = \overline{N}_K^e q_{Ki}^e \tag{3.57}$$

with:

$$\bar{N}_K^e = \begin{cases} N_K^e & K \in \Gamma_d^+ \\ -N_K^e & K \in \Gamma_d^- \end{cases} \tag{3.58}$$

where q_{Ki}^e is the displacement in the i direction of the K node of the element e, N_K^e are standard Lagrangian shape functions [89]. $\bar{N}_K^e$ are Lagrangian shape functions defined for the cohesive elements [47].

According to Equation (3.56), the displacement field, u_i, and the undeformed material coordinate, X_i, associated with the surfaces $\Gamma_{d^\pm}$ are interpolated as follows:

$$u_i^\pm = N_K q_{Ki}^\pm \tag{3.59}$$

$$X_i^\pm = N_K p_{Ki}^\pm \tag{3.60}$$

where $q_{Ki}^\pm$ are the nodal displacement vectors and $p_{Ki}^\pm$ are the undeformed material nodal coordinate vector. Note that the values of p_{Ki}^- and p_{Ki}^+ can be different in the case that an initial crack exists. Using these equations, the material coordinates of the interfacial midsurface are:

$$\bar{x}_i = \frac{1}{2} N_{Ki} \left(p_{Ki}^+ + p_{Ki}^- + q_{Ki}^+ + q_{Ki}^- \right) \tag{3.61}$$

The components of the two vectors that define the tangential plane can be written as:

$$v_{\eta_i} = \bar{x}_{i,\eta} = N_{Ki,\eta} \frac{1}{2} \left(p_{Ki}^+ + p_{Ki}^- + q_{Ki}^+ + q_{Ki}^- \right) \tag{3.62}$$

$$v_{\xi_i} = \bar{x}_{i,\xi} = N_{Ki,\xi} \frac{1}{2} \left(p_{Ki}^+ + p_{Ki}^- + q_{Ki}^+ + q_{Ki}^- \right) \tag{3.63}$$

Using (3.57) and (3.12), the displacement jump can then be obtained in local coordinates as:

$$\Delta_m = \Theta_{im}\bar{N}_K q_{Ki} = \bar{B}_{imK} q_{Ki} \tag{3.64}$$

with $\bar{B}_{inK} = \Theta_{in}\bar{N}^e_K$.

The contribution of a cohesive element for the internal load vector is given by:

$$f^{int}_{iK} = \int_{\Gamma_d} \tau_n \bar{B}_{inK} d\Gamma_d \tag{3.65}$$

The softening nature of the cohesive element constitutive equation causes difficulties in obtaining a converged solution for the non-linear problem when using Newton-Raphson iterative method. In particular, quadratic convergence is not assured because the residual vector is not continuously differentiable with respect to the nodal displacements.

The tangent stiffness matrix stems from the linearization of the internal force vector and it is obtained using Taylor's series expansion about the approximation q_{Ki} [48]. Taking into account that the calculation of the geometric terms of the tangent stiffness matrix is computationally very intensive, these terms are neglected. The tangent stiffness matrix, K_{rZiK}, for the cohesive element is therefore approximated as:

$$K_{rZiK} \approx \int_{\Gamma_d} \bar{B}_{jrZ} D^{\tan}_{nj} \bar{B}_{inK} d\Gamma_d \tag{3.66}$$

where $D^{\tan}_{ij}$ is the material tangent stiffness matrix, or constitutive tangent tensor defined in 3.2.4.

3.4 Comparison with experimental studies

The formulation proposed here was implemented in the ABAQUS Finite Element code [75] as a user-written element subroutine (UEL).

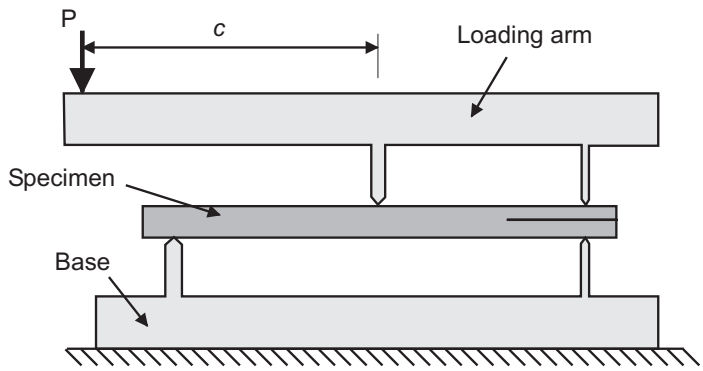

Figure 3.8: *MMB test specimen.*

To verify the element under different loading conditions, the numerical predictions were compared with experimental data obtained for composite test specimens and aircraft subcomponents. The double cantilever beam (DCB) test, the end notched flexure (ENF) test, and mixed-mode bending (MMB) tests in PEEK/AS4, a thermoplastic matrix composite material, were simulated.

The debonding of a composite co-cured skin-stiffener subcomponent loaded under tension was simulated, and the numerical results were compared with experimental data.

3.4.1 Mode I, mode II and mixed-mode I and II delamination growth for a PEEK composite

The most widely used specimen for mixed-mode fracture is the mixed-mode bending (MMB) specimen shown in Figure 3.8, which was proposed by Reeder and Crews [90]–[92].

The main advantages of the MMB test method are the possibility of using virtually the same specimen configuration as for mode I tests, and the capability of obtaining different mode-ratios, ranging from pure mode I to pure mode II, by changing the length c of the loading lever shown in Figure 3.8.

An 8-node cohesive element is used to simulate DCB, ENF and MMB tests in unidirectional AS4/PEEK carbon-fiber reinforced composite. The specimens simulated are 102-mm-long, 25.4-mm-wide, with two 1.56-mm-thick arms. The material properties are shown in Table 3.1, and a stiffness $K = 10^6$ N/mm^3 is used.

Table 3.1: *Ply properties.*

E_{11}	$E_{22} = E_{33}$	$G_{12} = G_{13}$	G_{23}	$\nu_{12} = \nu_{13}$
122.7 GPa	10.1 GPa	5.5 GPa	3.7 GPa	0.25
ν_{23}	G_{IC}	G_{IIC}	τ_3^o	$\tau_2^o = \tau_1^o$
0.45	0.969 kJ/m^2	1.719 kJ/m^2	80 MPa	100 MPa

The experiments used to assess the accuracy of the model proposed were performed by Reeder and Crews [90]-[92]. The experimental tests were performed at different $\frac{G_{\mathrm{II}}}{G_{\mathrm{T}}}$ ratios, ranging from pure mode I loading to pure mode II loading. The initial delamination length of the specimens (a_0) and the mixed-mode fracture toughness obtained experimentally are shown in Table 3.2.

Table 3.2: *Experimental data.*

$G_{\mathrm{II}}/G_{\mathrm{T}}$	0% (DCB)	20%	50%	80%	100% (ENF)
G_c (kJ/m^2)	0.969	1.103	1.131	1.376	1.719
a_0 (mm)	32.9	33.7	34.1	31.4	39.2

Models using 150 cohesive elements along the length of the specimens, and 4 cohesive elements along the width, were created to simulate the ENF and MMB test cases. The initial size of the delamination is simulated by placing open cohesive elements along the length corresponding to the initial delamination of each specimen

(see Table 2). These elements are capable of dealing with the contact conditions occurring for mode II or mixed-mode I and II loading, therefore avoiding interpenetration of the delamination faces. The model of the DCB test specimen uses 102 cohesive elements along the length of the specimen.

The different $G_{\mathrm{II}}/G_{\mathrm{I}}$ ratios are simulated by applying different loads at the middle and at the end of the test specimen. The analytical determination of the middle and end loads for each mode-ratio is presented in [47].

The experimental results relate the load to the displacement of the point of application of the load P in the lever (load-point displacement, Figure 3.8). Since the lever is not simulated, it is necessary to determine the load-point displacement from the displacement at the end and at the middle of the specimen using the analytical procedure described in [47].

The B-K parameter, $\eta = 2.284$, is calculated by applying a least-squares fit to the experimental data shown in Table 3.2.

Figures 3.9 to 3.13 show the numerical predictions and the experimental data for all the test cases simulated.

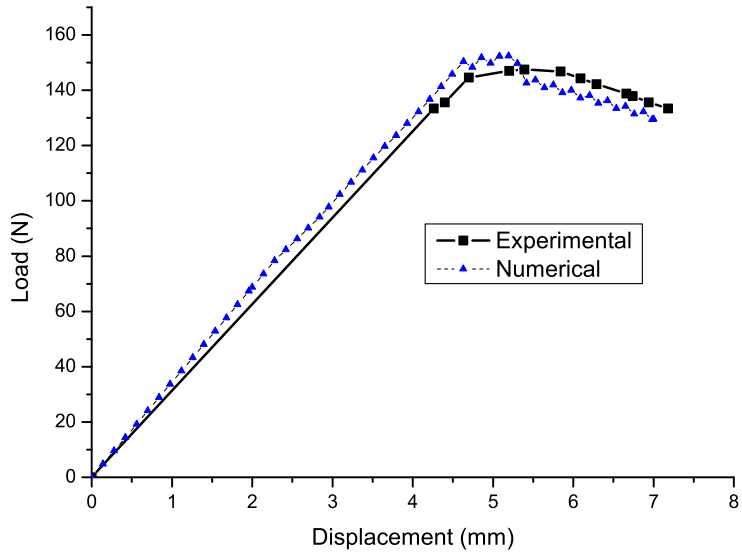

Figure 3.9: *Numerical and experimental results- pure mode I loading.*

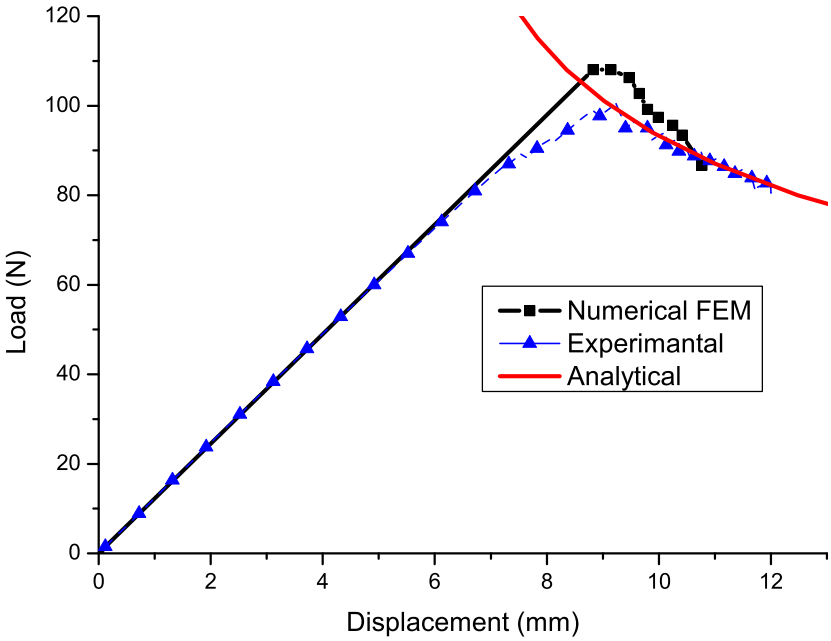

Figure 3.10: *Numerical and experimental results- mixed-mode I and II loading with* G_{II}/G_T*=20%.*

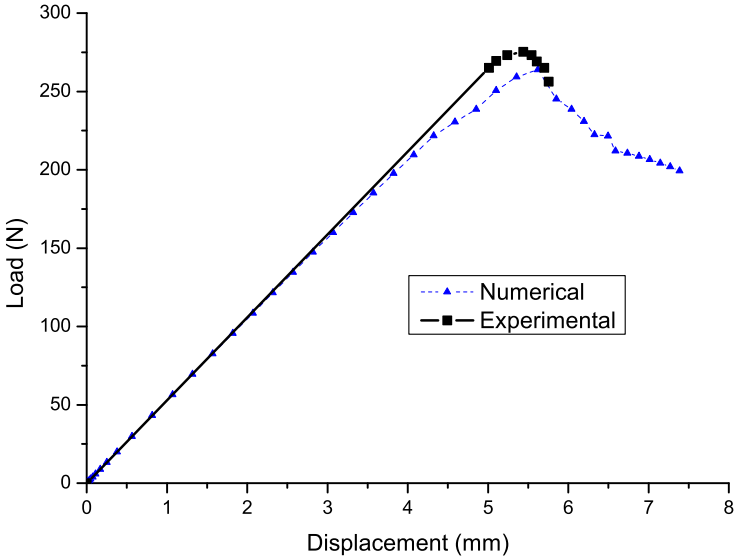

Figure 3.11: *Numerical and experimental results- mixed-mode I and II loading with* G_{II}/G_T*=50%.*

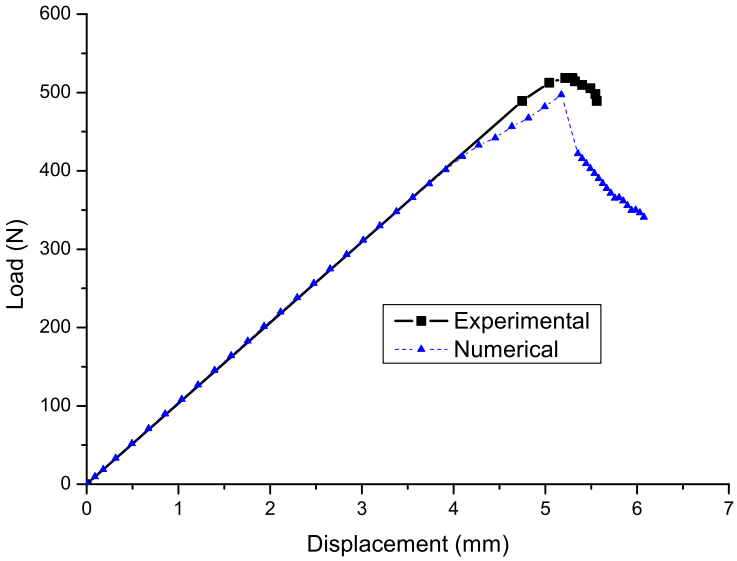

Figure 3.12: *Numerical and experimental results- mixed-mode I and II loading with* G_{II}/G_T*=80%.*

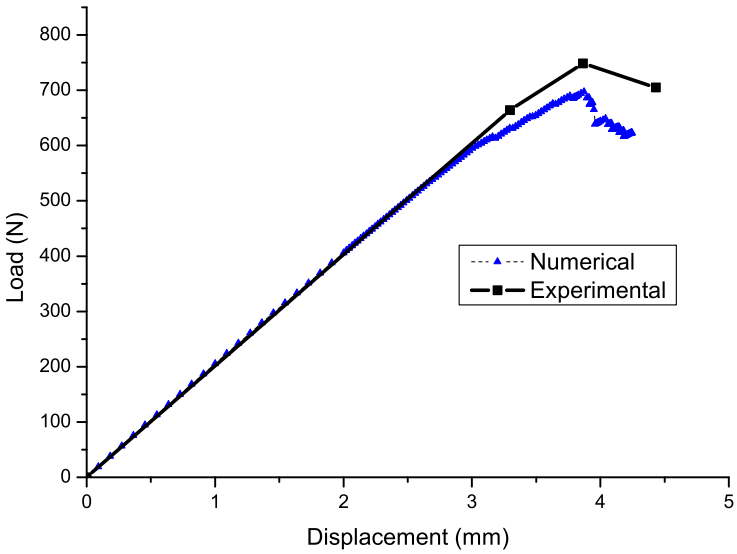

Figure 3.13: *Numerical and experimental results- pure mode II loading.*

Table 3.3 shows the comparison between the predicted and experimentally determined maximum loads.

Table 3.3: *Maximum loads.*

$G_{\mathrm{II}}/G_{\mathrm{T}}$	Predicted (N)	Experimental (N)	Error (%)
0% (DCB)	152.4	147.5	3.4
20%	99.3	108.1	-8.1
50%	263.9	275.3	-4.2
80%	496.9	518.7	-4.2
100% (ENF)	697.1	748.4	-6.9

It can be concluded that a good agreement between the numerical predictions and the experimental results is obtained. The largest difference (-8.1%) corresponds to the case of an MMB test specimen with $\frac{G_{\mathrm{II}}}{G_{\mathrm{T}}} = 20\%$. This fact is not surprising,

since the largest difference between the fracture toughness experimentally measured and the one predicted using the B-K criterion occurs for $\frac{G_{\mathrm{II}}}{G_{\mathrm{T}}} = 20\%$.

3.4.2 Skin-stiffener co-cured structure

Most composite components in aerospace structures are made of panels with co-cured or adhesively bonded frames and stiffeners. Testing of stiffened panels has shown that bond failure at the tip of the stiffener flange is a common failure mode. Comparatively simple specimens consisting of a stringer flange bonded onto a skin have been developed by Krueger et al. to study skin/stiffener debonding [93]. The configuration of the specimens studied by Krueger is shown in Figure 3.14.

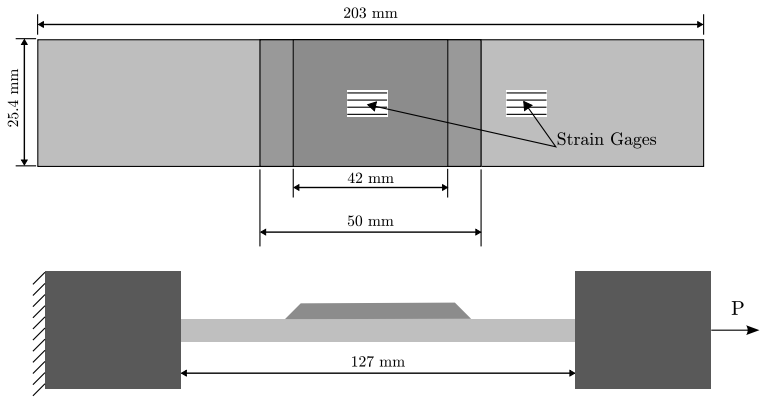

Figure 3.14: *Skin-stiffener test specimen.*

The specimens are 203 mm-long, 25.4 mm-wide. Both skin and flange were made from IM6/3501-6 graphite/epoxy prepreg tape with a nominal ply thickness of 0.188 mm. The skin lay-up consisting of 14 plies was $(0°/45°/90°/\text{-}45°/45°/\text{-}45°/0°)_S$ and the flange lay-up consisting of 10 plies was $(45°/90°/\text{-}45°/0°/90°)_S$.

The properties of the unidirectional graphite/epoxy and the properties of the interface reported in reference [93] are shown in Tables 3.4 and 3.5, respectively.

The parameter for the B-K criterion is taken from test data for AS4/3501-625 as η=1.45, and a stiffness $K = 10^6$ N/mm^3 is used.

Table 3.4: *Material properties for IM6-3501-6 unidirectional graphite epoxy.*

E_1 (GPa)	E_2=E_3 (GPa)	$\nu_{12} = \nu_{13}$	ν_{23}	G_{12}=G_{13} (GPa)	G_{23} (GPa)
144.7	9.6	0.3	0.45	5.2	3.4

Table 3.5: *Interface properties for IM6-3501-6 unidirectional graphite epoxy.*

G_{IC} (kJ/m^2)	G_{IIC} (kJ/m^2)	τ_3^o (MPa)	τ_{shear}^o (MPa)	η
0.075	0.547	61	68	1.45

To keep the modeling difficulties low and the approach applicable to larger problems, the model that was developed uses only two brick elements through the thickness of the skin, and another two through the flange. The complete model consists of 1002 three-dimensional 8-node elements and 15212 degrees of freedom. To prevent delamination from occurring at both ends of the flange simultaneously, model symmetry was reduced by modeling the tapered ends of the flange with a refined mesh on one side and a coarser mesh on the other. Unlike the previous analyses of this construction, this model does not contain any pre-existing delaminations.

Residual thermal effects in the composite plies are simulated by performing a thermal analysis step before the mechanical loads are applied. The same coefficients of thermal expansion (α_{11}=-2.4x10^{-8} /°C and α_{22}=3.7x10^{-5} /°C) are applied to the skin and the flange, and the temperature difference between the room and curing temperatures is ΔT=-157 °C. The flange has more 90° plies than 0° plies, and the skin is quasi-orthotropic, so it is expected that residual thermal stresses are present at their interface at room temperature.

Deformed plots of the finite element model immediately before and after flange separation are shown in Figure 3.15. It can be observed that only the refined end of the flange separates. It is worth noticing that the debond growth is not symmetric across the width: the debond initiates on the left corner of the flange shown on the bottom left of Figure 3.15 due to the lack of symmetry introduced by the terminated

plies at the flange tapered ends. This behavior was also observed in the experiments [93].

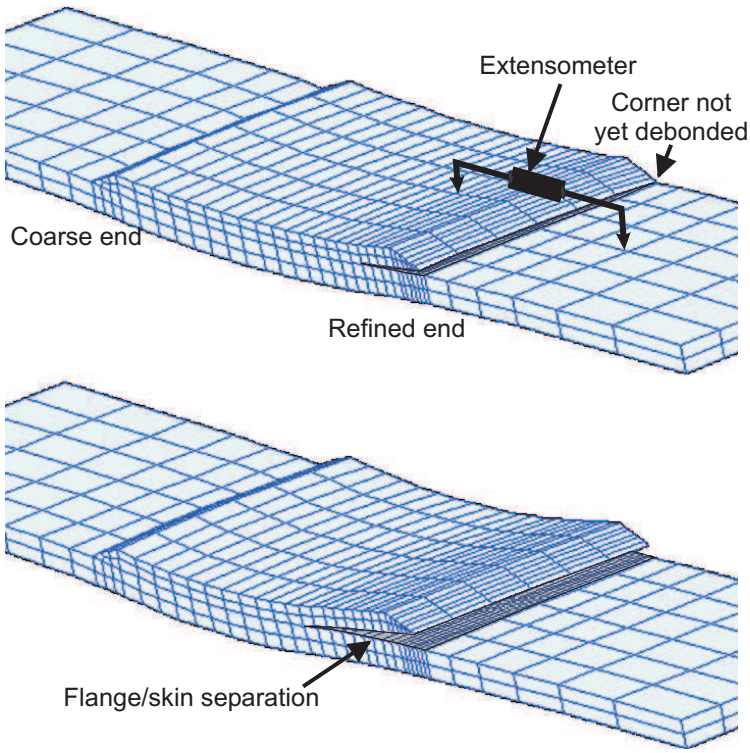

Figure 3.15: *Skin-Stiffener debonding.*

Figure 3.16 shows the load-extensometer measurement relation obtained in four experiments and the corresponding numerical prediction. Debond is detected in the experiments by the discontinuities in the load-displacement relation.

Table 3.6 compares the average of the measured debond loads with the numerical predictions.

Table 3.6: *Comparison between experimental and numerical results.*

	Experimental (kN)	Predicted (kN)	Error (%)
Flange debond load	22.7	21.0	-7.5

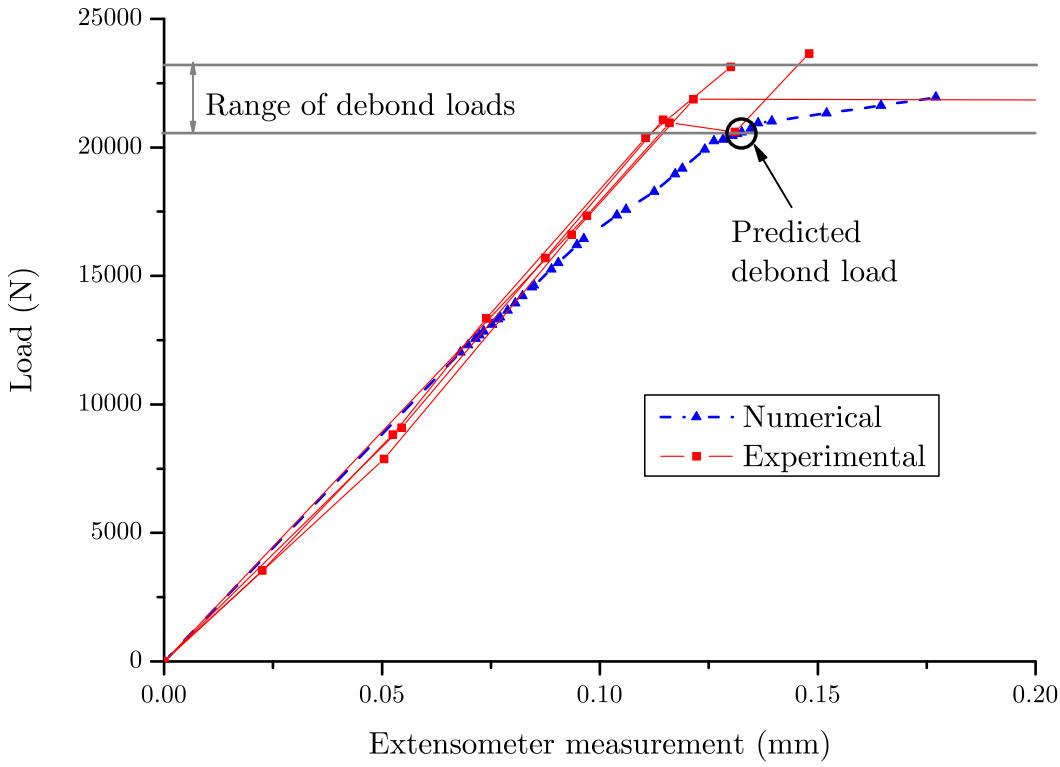

Figure 3.16: *Experimental and numerical load-extensometer displacement relations.*

It can be observed that good accuracy in the prediction of the debond loads is obtained. The predicted stiffness of the specimen is also in good agreement with the experimental data. The stiffening effect detected in the experiments, Figure 3.16, is due to the extensometer rotation as a result of specimen bending. Although specimen bending is properly represented by the numerical model, the extensometer measurement calculated from the numerical model does not account for the rotation of the extensometer.

3.5 Concluding remarks

A thermodynamically consistent model for the simulation of progressive delamination based on Damage Mechanics was presented. A constitutive equation for the interface was derived from the free energy of the interface. The resulting damage model simulates delamination onset and delamination propagation. The constitutive equation proposed uses a single scalar variable to track the damage at the interface under general loading conditions. A new initiation criterion that evolves from the Benzeggagh-Kenane propagation criterion has been developed to assure that the model accounts for changes in the loading mode in a thermodynamically consistent way and avoids restoration of the cohesive state. The damage model was implemented in a finite element model. The material properties required to define the element constitutive equations are the interlaminar fracture toughnesses, the penalty stiffness, and the strengths of the interface. In addition, a material parameter η, which is determined from standard delamination tests, is required for the Benzeggagh-Kenane mode interaction law.

Two examples were presented that test the accuracy of the method. In the first example, the simulations of the DCB, ENF and MMB tests represent cases of single-mode and mixed-model delamination. A composite skin-stiffener co-cured sub-component was also simulated, and the model predictions were compared with available experimental data.

The examples analyzed are in good agreement with the test results, and they indicate that the proposed formulation can predict the strength of composite structures that exhibit progressive delamination.

Chapter 4

Analysis of the mesh size influence

4.1 Introduction

The simulation of progressive delamination using cohesive elements poses numerical difficulties related to the proper definition of the stiffness of the cohesive layer, the requirement of extremely refined meshes, and the convergence difficulties associated with problems involving softening constitutive models.

A procedure to determine the optimal value of the penalty stiffness of a cohesive element is proposed in this Chapter. A closed-form expression for the interface stiffness is developed, replacing the empirical definitions of the stiffness of the cohesive layer that are normally used. In addition, a solution that allows the use of coarse meshes in the simulation of delamination is proposed. The procedure is based on an artificial increase of the cohesive zone length that it is obtained by lowering the interfacial strength while keeping the fracture toughness constant. It is shown that it is possible to predict the propagation of delamination accurately in specimens with pre-existing cracks by using coarse meshes and their correspondingly adjusted constitutive models.

The methodologies proposed here are relevant for the use of cohesive zone models in the simulation of delamination in large composite structures used in the industry

where the requirements of extremely fine meshes cannot be met.

4.2 Selection of cohesive zone model parameters

4.2.1 Cohesive zone model and FEM

In a finite element model using the CZM approach, the complete material description is separated into fracture properties, captured by the constitutive model of the cohesive surface, and the properties of the bulk material, captured by the continuum regions.

To obtain a successful FEM simulation using CZM [94], two conditions must be met: (a) The cohesive contribution to the global compliance before crack propagation should be small enough to avoid the introduction of a fictitious compliance to the model [95, 96], and (b) the element size must be less than the cohesive zone length [43, 97, 98].

(a) *Stiffness of the cohesive zone model*

Different guidelines have been proposed for selecting the stiffness of the interface. Daudeville et al. [99] calculated the stiffness in terms of the thickness and the elastic modulus of the interface. The resin-rich interface between plies is of the order of 10^{-5}m. Therefore, the interface stiffness obtained from the Daudeville et al. equations is very high. Zou et al. [100], based on their own experience, proposed a value for the interface stiffness between 10^4 and 10^7 times the value of the interfacial strength per unit length. Camanho et al. [47] obtained accurate predictions for Graphite/Epoxy specimens using a value of 10^6N/mm^3.

The effective elastic properties of the whole laminate depend on the properties of both the cohesive surfaces and the bulk constitutive relations of the plies. Although the compliance of the cohesive surfaces can contribute to the global deformation, the only purpose of the cohesive surfaces is to simulate fracture. Moreover, the elastic

properties of the cohesive surfaces are mesh-dependent because the surface relations exhibit an inherent length scale that is absent in homogeneous deformations [101].

If the cohesive contribution to the compliance is not small enough compared to that of the volumetric constitutive relation, a stiff connection between two neighboring layers before delamination initiation is not assured. The effect of compliance of the interface on the bulk properties of a laminate is illustrated in the one-dimensional model shown in Figure 4.1. The equilibrium condition requires:

$$\sigma = E_3\varepsilon = K\Delta \tag{4.1}$$

where σ is the traction on the surface, t is the thickness of an adjacent sublaminate, $\varepsilon = \frac{\delta t}{t}$ is the transverse strain, K is the interface stiffness that relates the resulting tractions at the interface with the opening displacement Δ, and E_3 is the through-the-thickness Young's modulus of the material. For a transversely isotropic material $E_3 = E_2$.

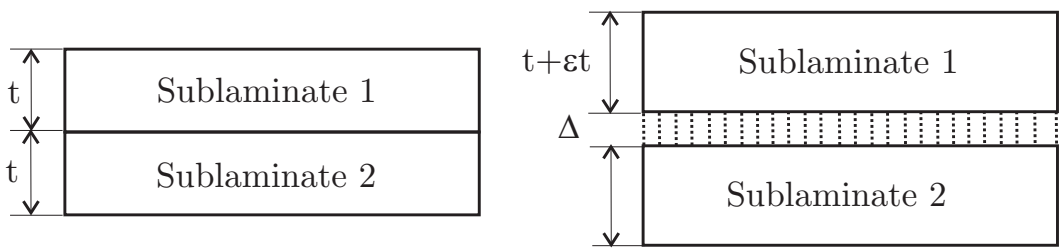

Figure 4.1: *Influence of the cohesive surface on the deformation.*

The effective strain of the composite is:

$$\varepsilon_{\text{eff}} = \frac{\delta t}{t} + \frac{\Delta}{t} = \varepsilon + \frac{\Delta}{t} \tag{4.2}$$

Since the equilibrium condition requires that $\sigma = E_{\text{eff}}\varepsilon_{\text{eff}}$, the equivalent Young's modulus E_{eff} can be written as a function of the Young's modulus of the material, the

mesh size, and the interface stiffness. Using Equations (4.1) and (4.2), the effective Young's modulus can be written as:

$$E_{\text{eff}} = E_3 \left(\frac{1}{1 + \frac{E_3}{Kt}} \right) \tag{4.3}$$

The effective elastic properties of the composite will not be affected by the cohesive surface whenever $E_3 \ll Kt$, i.e:

$$K = \frac{\alpha E_3}{t} \tag{4.4}$$

where α is a parameter much larger than 1 ($\alpha \gg 1$). However, large values of the interface stiffness may cause numerical problems, such as spurious oscillations of the tractions [41]. Thus, the interface stiffness should be large enough to provide a reasonable stiffness but small enough to reduce the risk of numerical problems such as spurious oscillations of the tractions in an element. For values of α greater than 50, the loss of stiffness due to the presence of the interface is less than 2%, which is sufficiently accurate for most problems.

Equation (4.4) is valid for mode I opening. For shear mode (mode II or mode III) the corresponding shear modulus should be used instead of E_3 . However, since the cohesive damage model is formulated assuming the same interface stiffness for all mode-ratios, Equation (4.4) is used to compute the interface stiffness independently of the mode-ratio.

The use of Equation (4.4) is preferable to the guidelines presented in previous works [47, 99, 100] because it results from mechanical considerations, and the resulting value of K does not significantly affect the compliance of the composite.

The spurious oscillations of the tractions resulting from an excessively stiff interface and Gauss integration scheme [102] are avoided by calculating the interface stiffness using Equation (4.4), using linear shape functions and Newton-Cotes integration scheme [102].

The values of the interface stiffness obtained with Equation (4.4) and those used by other authors for a carbon/epoxy composite are shown in Table 4.1. The material's transverse modulus is 11GPa, its nominal interfacial strength is τ^o = 45MPa, and α is taken as 50.

Table 4.1: *Interface stiffness K proposed by different authors (N/mm^3) and those calculated from Equation (4.4).*

t(mm)	0.125	1	2	3	5
Equation (4.4)	4.43x10^6	5.5x10^5	2.75x10^5	1.83x10^5	1.1x10^5
Zou et al. [100]		4.5x10^5	$\leq$ K $\leq$	4.5x10^8	
Camanho et al. [47]	10^6	10^6	10^6	10^6	10^6

Equation (4.4) gives a range of the interface stiffness between 10^5 and 5x10^{6}N/mm^3 for a sub-laminate thickness between 0.125mm and 5mm. These values are close to the interface stiffness proposed by Camanho and Dávila and the values obtained from Zou's guidelines (between 4.5x10^5 and 4.5x10^{8}N/mm^3).

(b) *Length of the cohesive zone*

Under single-mode loading, interface damage initiates when the traction reaches the maximum nominal interfacial strength, τ^o. For mixed-mode loading, damage onset is predicted by a criterion established in terms of the normal and shear tractions. Crack propagation occurs when the energy release rate reaches a critical value G_c. The CZM approach prescribes the interfacial normal and shear tractions that resist separation and relative sliding at an interface. The tractions, integrated to complete separation, yield the fracture energy release rate, G_c. The length of the cohesive zone l_{cz} is defined as the distance from the crack tip to the point where the maximum cohesive traction is attained

Different models have been proposed in the literature to estimate the length of the cohesive zone. Irwin [103] estimated the size of the plastic zone ahead of a crack in a ductile solid by considering the crack tip zone where the von Mises equivalent stress exceeds the tensile yield stress. Dugdale [24] estimated the size of the yield zone ahead of a mode I crack in a thin plate of an elastic-perfectly plastic solid by idealizing the plastic region as a narrow strip extending ahead of the crack tip that is loaded by the yield traction. Barenblatt [25] provided an analogue for ideally brittle materials of the Dugdale plastic zone analysis. Hui et al. [104] estimated the length of the cohesive zone for soft elastic solids, and Falk et al. [94] and Rice [105] estimated the length of the cohesive zone as a function of the crack growth velocity. The expressions that result from these models for the case of plane stress are presented in Table 4.2. The relation between the critical stress intensity factor K_c and the critical energy release rate G_c can be expressed as $K_c^2 = G_c E$.

All of the models described above predict the cohesive zone length l_{cz} in an infinite body under uniform remote loading and have the form:

$$l_{cz} = ME\frac{G_c}{(\tau^o)^2} \tag{4.5}$$

where E is the Young's modulus of the material, G_c is the critical energy release rate, τ^o is the maximum interfacial strength, and M is a parameter that depends on each cohesive zone model. The most commonly used models in the literature are Hillerborg's model [26] and Rice's model [105]. In these models, the parameter M is either close or exactly equal to unity. A summary of the different models commonly used in the literature, and the equivalent parameter M for plane stress are shown in Table 4.2. In this work, Rice's model is used in the following analysis.

For the case of orthotropic materials with transverse isotropy, the value of the Young's modulus in Equation (4.5) is the transverse modulus of the material, E_3.

Table 4.2: *Length of the cohesive zone and equivalent value of the parameter M.*

	l_{cz}	M
Hui et al. [104]	$\frac{2}{3\pi}E\frac{G_c}{(\tau^o)^2}$	0.21
Irwin [103]	$\frac{1}{\pi}E\frac{G_c}{(\tau^o)^2}$	0.31
Dugdale [24], Barenblatt [25]	$\frac{\pi}{8}E\frac{G_c}{(\tau^o)^2}$	0.40
Rice [105], Falk et al.[94]	$\frac{9\pi}{32}E\frac{G_c}{(\tau^o)^2}$	0.88
Hillerborg et al. [26]	$E\frac{G_c}{(\tau^o)^2}$	1.00

For delamination in slender bodies, the cohesive zone length is a material and structural property [106]. For constitutive models that prescribe non-zero tractions when the displacement jump is zero, for a centered mode I crack in a slender beam, the length of the cohesive zone can be estimated as [106]:

$$l_{cz} = \left[E\frac{G_c}{(\tau^0)^2}\right]^{1/4} t^{3/4} \tag{4.6}$$

The constitutive model used here prescribe zero tractions when the displacement jump is zero. Therefore, the length of the cohesive zone predicted by Equation (4.6) will be smaller than the effective cohesive length.

In order to obtain accurate FEM results using CZM, the tractions in the cohesive zone must be represented properly by the finite element spatial discretization. The number of elements in the cohesive zone is:

$$N_e = \frac{l_{cz}}{l_e} \tag{4.7}$$

where l_e is the mesh size in the direction of crack propagation.

When the cohesive zone is discretized by too few elements, the distribution of tractions ahead of the crack tip is not represented accurately. Therefore, a minimum number of elements, N_e, is needed in the cohesive zone to get successful FEM results.

However, the minimum number of elements needed in the cohesive zone is not well established: Moës and Belytschko [107], based on the work of Carpinteri et al. [31], suggested using more than 10 elements. However, Falk et al. [94] used between 2 and 5 elements in their simulations. Mi et al. [43] also suggested to use at least 2 elements in the cohesive zone. In the parametric study by Dávila and Camanho et al. [108], the minimum element length for predicting the delamination in a double cantilever beam (DCB) specimen was 1 mm, which leads, using Equation (4.5) with $M = 1$, to a length of the cohesive zone of 3.28 mm. Therefore, 3 elements in the cohesive zone were sufficient to predict the propagation of delamination in mode I.

4.2.2 Guidelines for the selection of the parameters of the interface with coarser meshes

One of the drawbacks in the use of cohesive zone models is that very fine meshes are needed to assure a reasonable number of elements in the cohesive zone. The length of the cohesive zone given by Equation (4.5) is proportional to the fracture energy release rate (G_c) and to the inverse of the square of the interfacial strength τ^o. For typical graphite-epoxy or glass-epoxy composite materials, the length of the cohesive zone is smaller than one or two millimeters. Therefore, according to Equation (4.7), the mesh size required in order to have more than two elements in the cohesive zone should be smaller than half a millimeter. The computational requirements needed to analyze a large structure with these mesh sizes may render most practical problems intractable.

Alfano and Crisfield [45] observed that variations of the maximum interfacial strength do not have a strong influence in the predicted delamination propagation results, but that lowering the interfacial strength can improve the convergence rate of the solution. The result of using a lower interfacial strength is that the length of the cohesive zone and the number of elements in the cohesive zone increase. Therefore, the representation of the softening response of the fracture process ahead

of the crack tip is more accurate with a lower interface strength although the stress distribution in the regions near the crack tip might be altered [45].

It is possible to develop a strategy to adapt the length of the cohesive zone to a given mesh size. The procedure consists of determining the value $\overline{\tau}^0$ of the interfacial strength required for a desired number of elements (N_e^o) in the cohesive zone. From Equations (4.5) and (4.7), the required interface strength is:

$$\overline{\tau}^0 = \sqrt{\frac{9\pi E G_c}{32 N_e^o l_e}} \tag{4.8}$$

Finally, the interfacial strength is chosen as:

$$T = \min\left\{\tau^0, \overline{\tau}^0\right\} \tag{4.9}$$

The interfacial strength is computed for each loading mode, replacing the values of the fracture toughness in Equation (4.8) and of the ultimate traction in Equation (4.9) by the values corresponding to the loading mode.

The effect of a reduction of the interfacial strength is to enlarge the cohesive zone, and thus, the model is better suited to capture the softening behaviour ahead of the crack tip. Although the stress concentrations in the bulk material near the crack tip are less accurate when using a reduced interfacial strength value, the mechanics of energy dissipation are properly captured, which ensures the proper propagation of the crack front. Moreover, if Equation (4.4) is used to compute the interface stiffness, the interface stiffness will be large enough to assure a stiff connection between the two neighboring layers and small enough to avoid spurious oscillations.

The strategy of lowering the interfacial strength whilst keeping the fracture toughness constant was also proposed by Bažant and Planas [109] in a different context. The procedure developed by Bažant and Planas is used in the numerical implementation of crack band models where the energy dissipated is a function of the volume of the finite element [109]. In this case, it is necessary to modify the

constitutive model including a characteristic element length to assure that the computed fracture energy is independent of the discretization. The reduction of the maximum stress is used to avoid snap-back of the modified constitutive model of large elements.

Using cohesive models, there is no need to adjust the size of the element in order to compute the correct energy dissipated. It is, however, necessary to have a sufficient number of elements in the cohesive zone to capture the correct distribution of tractions. Therefore, the critical dimension of the finite element is along the crack propagation path.

When using crack band models in the simulation of delamination using coarse meshes, the strength must be adjusted taking into account the dimension of the element in the direction perpendicular to the crack plane (Bažant's model [109]), and also the dimension of the element in the crack propagation path using the method proposed here.

4.3 Simulation of the double cantilever beam specimen

The influence of mesh size, interface stiffness, interface strength, and the selection of the parameters of the constitutive equation according to the proposed methodology were investigated by analyzing the mode I delamination test (double cantilever beam, DCB). The DCB specimen was fabricated with a unidirectional T300/977-2 carbon-fiber-reinforced epoxy laminate. The specimen was 150-mm-long, 20.0 mm-wide, with two 1.98-mm-thick arms, and it had an initial crack length of 55mm. The material properties are shown in Table 4.3 [48].

Table 4.3: *Mechanical and interface material properties of T300/977-2 [48],[110].*

E_{11}	$E_{22} = E_{33}$	$G_{12} = G_{13}$	G_{23}
150.0GPa	11.0GPa	6.0GPa	3.7GPa
$\nu_{12} = \nu_{13}$	ν_{23}	G_{IC}	τ_3^o
0.25	0.45	0.352N/mm	60MPa

The FEM model is composed of two layers of four-node 2D plane strain elements connected together with four-node cohesive elements. The cohesive elements were implemented using a user-written subroutine in the finite element code ABAQUS [75].

Several sets of simulations were performed. A very refined mesh using an element length of 0.0125mm was used in the simulation of a DCB specimen to predict the

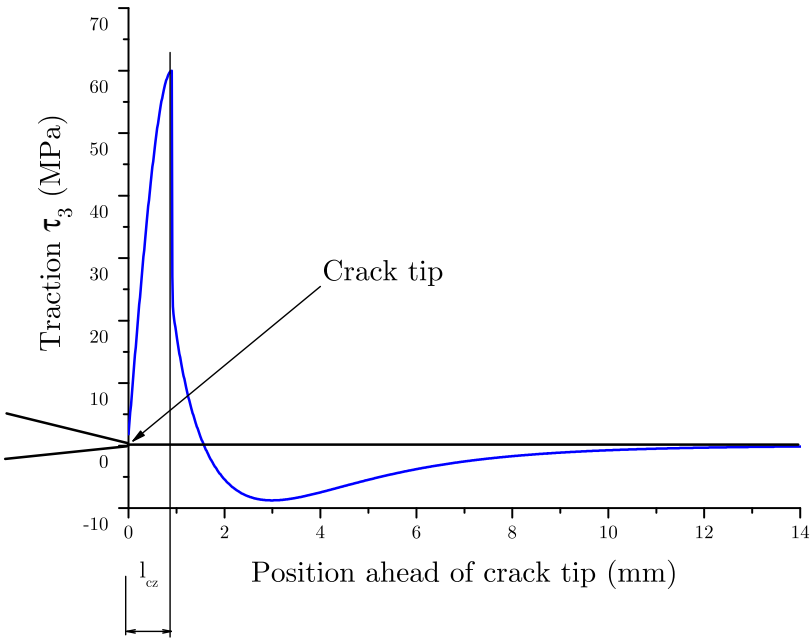

Figure 4.2: *Distribution of tractions ahead of the crack tip at peak load.*

distribution of tractions ahead of the crack tip and the corresponding length of the cohesive zone.

The distribution of tractions ahead of the crack tip at the peak load of DCB specimen is shown in Figure 4.2.

The length of the cohesive zone obtained from the analysis results shown in Figure 4.2 is 0.9mm. Using the material parameters shown in Table 4.3 and Equation (4.5), the parameter M is calculated as 0.84. This value is closest to Rice's model (0.88), shown in Table 4.2.

Other DCB tests were simulated with different levels of mesh refinement using the material properties shown in Table 4.3 and interfacial stiffness of K=10^6N/mm^3. Equations (4.4) and (4.7) were used to calculate an adjusted interfacial strength and interface stiffness. Finally, a set of simulations with a constant mesh size using different interface stiffnesses were performed in order to investigate the influence of the stiffness on the calculated results.

To study the effects of mesh refinement, several analyses were carried out for element sizes ranging between 0.125mm and 5mm. The corresponding load-displacement curves, the analytical solution, and one of the results of the experimental tests are shown in Figure 4.3. The results indicate that a mesh size of $l_e \leq 0.5$mm is necessary to obtain converged solutions. The predictions made with coarser meshes overpredict significantly the analytical and the experimental results shown in Figure 4.3. Using Equation (4.5) with Rice's model, the length l_{cz} of the cohesive zone for the material given in Table 4.3 is 0.95mm. Therefore, for a mesh size greater than 0.47mm, fewer than two elements would span the cohesive zone, which is not sufficient for an accurate representation of the fracture process [31, 108].

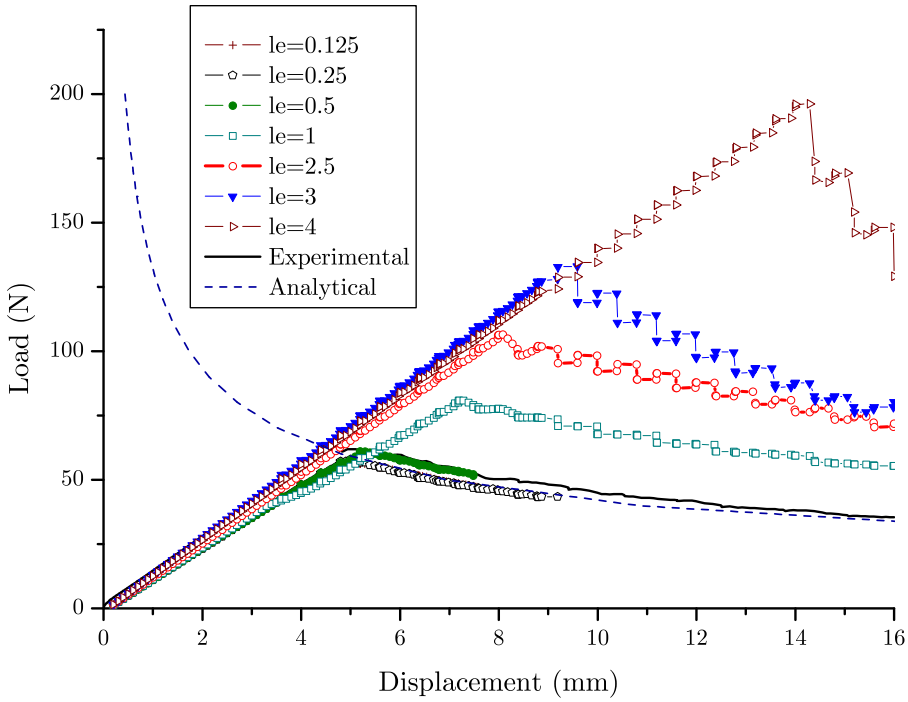

Figure 4.3: *Load-displacement curves using the nominal interface strength (τ^0=60MPa) for a DCB test with different mesh sizes.*

The error obtained from using a coarse mesh in the simulation of delamination in a DCB test specimen is related with the representation of the contact tractions ahead of the crack tip. The predicted distributions of the normal tractions ahead of the crack tip at 30kN using a fine mesh (element length of 0.0125mm) and a coarse mesh (element length of 1mm) are shown in Figure 4.4.

For an applied load of 30kN, the fine-mesh model captures the softening region ahead of the crack tip while the coarse-mesh model does not.

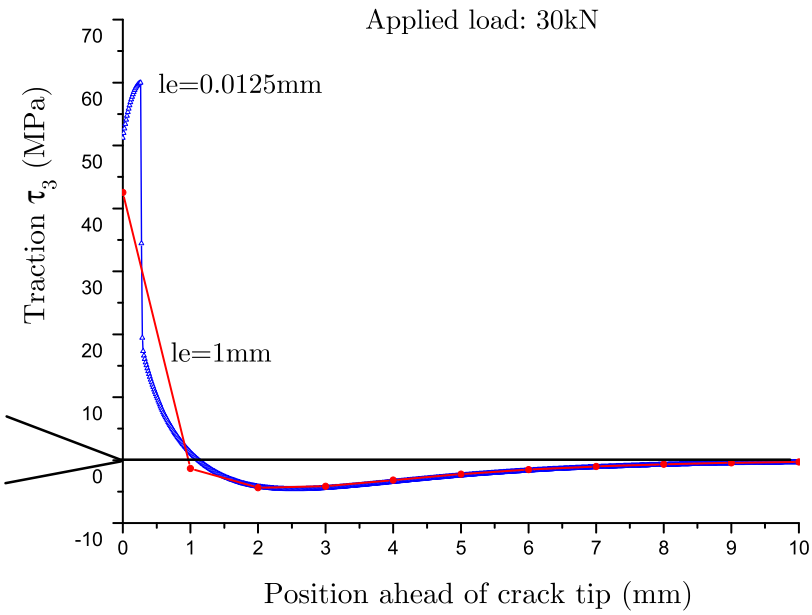

Figure 4.4: *Distribution of tractions ahead of the crack tip for an applied load of 30kN.*

4.3.1 Effect of interface strength

To verify the effect of the interface strength on the numerical results, simulations were performed by specifying the desired number of elements within the cohesive zone to be $N_0 = 5$ and reducing the interface strength according to Equation (4.9). The load-displacement curves obtained for several levels of mesh refinement are shown in Figure 4.5. Accurate results are obtained for mesh sizes smaller than 2.5mm.

A comparison of the maximum loads predicted using the nominal interface strength and the strength obtained from Equation (4.9) is shown in Figure 4.6. The failure load obtained by keeping the maximum interfacial strength constant increases with the mesh size. Mesh dependence is especially strong for mesh sizes greater than 2mm. However, the failure loads predicted by modifying the interfacial strength according to Equation (4.9) are nearly constant for element sizes smaller

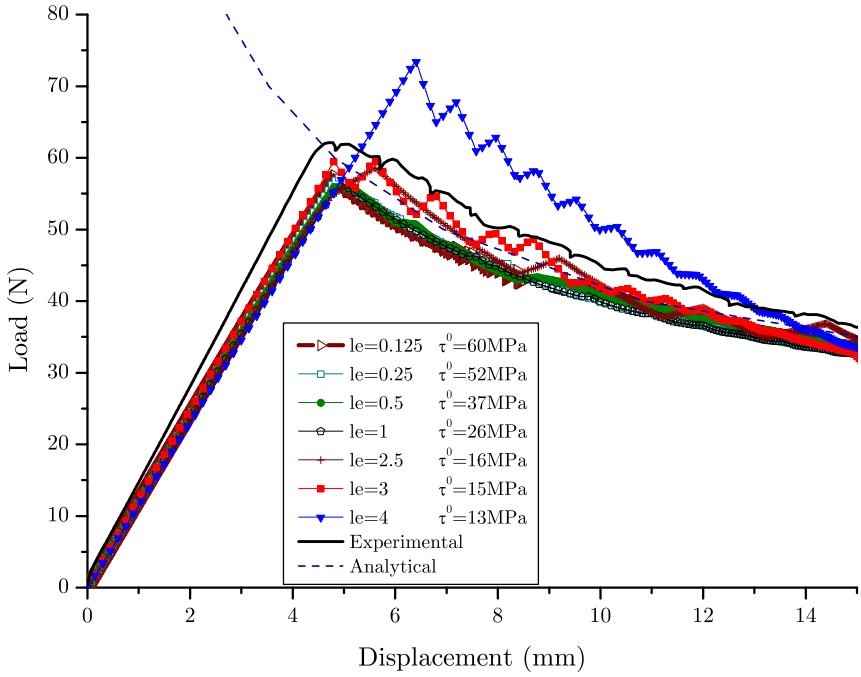

Figure 4.5: *Load-displacement curves obtained for a DCB test with different mesh sizes with the interface strength modified to keep* $N_e \geq 5$.

than 3mm. In addition, the finite element results shown that the global deformation and the crack tip position are also nearly independent from mesh refinement.

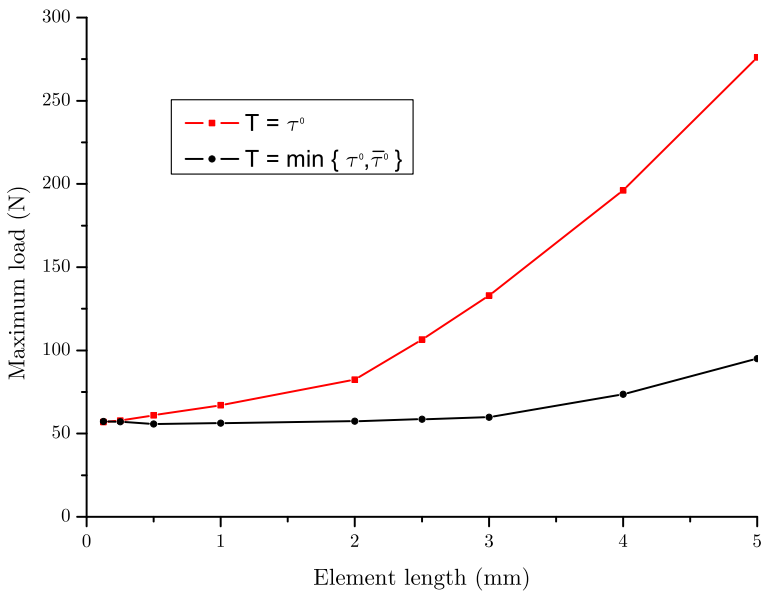

Figure 4.6: *Maximum load obtained in a DCB test for two cases: a) with constant interfacial strength, b) with interfacial strength calculated according to Eq. (4.9).*

4.3.2 Effect of interface stiffness

The DCB test was simulated with a mesh size of 2.5mm for various values of the interface stiffness in order to investigate the influence of the stiffness on the predicted failure load. The results of the simulations are presented in Figure 4.7.

The load-displacement response curves obtained from simulations using an interface stiffness greater than 10^4N/mm^3 are virtually identical. However, smaller values of the interface stiffness have a strong influence on the load-displacement curves, since a stiff connection between the two neighboring layers is not assured. Moreover, the number of iterations needed for the solution when using an interface stiffness smaller than 10^4N/mm^3 is greater than the number of iterations needed for a range of the interface stiffness between 10^6 and 10^{10}N/mm^3. For values of the interface stiffness significantly greater than 10^{10}N/mm^3, the number of iterations needed for the solution increases. The stiffness that results from Equation (4.4)

with $\alpha = 50$ is $K = 5.55\text{x}10^5\text{N/mm}^5$, which is ideal for a good convergence of the solution procedure.

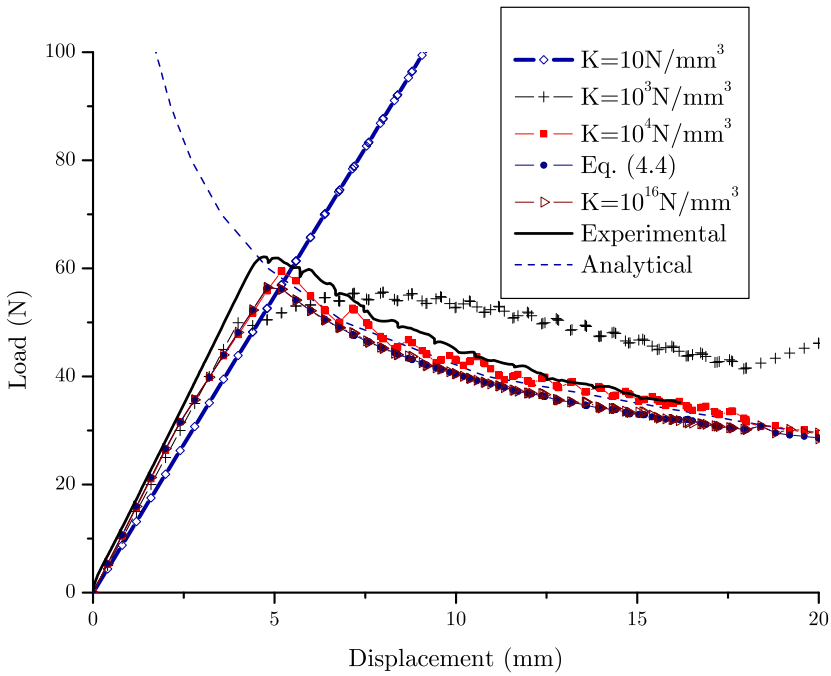

Figure 4.7: *Influence of the interface stiffness on the load-displacement curves.*

4.4 Simulation of free-edge delamination

Free-edge delamination is a typical mode of damage initiation in specimens without pre-existing cracks [111]–[113]. To examine the effect of mesh size on a problem in which crack initiation is the critical issue, analyses were performed to predict the initiation of free edge delaminations of $[\pm 25°/90°]_s$ laminates studied by Crossman et al. [112].

4.4.1 Problem statement

The $[\pm 25°/90°]_s$ graphite-epoxy laminates investigated by Crossman et al. were subjected to uniaxial strain. The laminates were fabricated from Fiberite T300/934

prepreg tape using an autoclave. The cross-section of the specimen was 25.0-mm-wide and 0.792-mm-thick (see Figure 4.8). No initial cracks were induced in the laminate. The material properties are shown in Table 4.4 [111, 114].

Tensile tests were performed by applying a controlled displacement in the x-direction. Due to the stacking sequence, the through the thickness free-edge stress distribution produces high σ_{zz} in the 90° ply. Therefore, high tractions occur at the 90°/90° interface, leading to the onset of delamination at the free-edge.

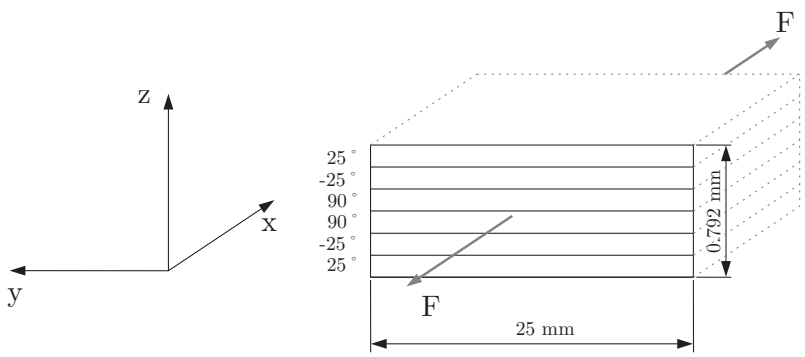

Figure 4.8: *Cross-section of the laminate.*

Table 4.4: *Mechanical properties of T300/934 Graphite Epoxy [111], [114].*

E_{11}	$E_{22} = E_{33}$	$G_{12} = G_{13}$	G_{23}	$\nu_{12} = \nu_{13}$	ν_{23}
140.0GPa	11.0GPa	5.5GPa	3.61GPa	0.29	0.52

4.4.2 Numerical predictions

A FEM model was developed using six layers of 4-node generalized plane strain elements [115, 116]. The generalized plane strain model developed calculates the out-of-plane components of the stress tensor that cause delamination onset. The 90°/90° interface was modeled with the 4-node cohesive elements presented in previous sections. The elastic properties of each layer were defined by means of the 3D stiffness matrix. Due to the symmetry of the laminate, only half of the cross-section was modeled.

Two sets of simulations were performed. First, tensile tests were simulated with different levels of mesh refinement. Then, equations (4.7) and (4.4) were used to calculate the interface strength and the interface stiffness.

Several analyses were carried out for mesh sizes ranging between 0.05mm and 0.5mm. The load-displacement curves obtained are shown in Figure 4.9. An interfacial stiffness of K=10^6N/mm^3, an interface strength of 51.7MPa, a critical energy release rate of 0.175N/mm [111], and the material properties shown in Table 4.4 were used. The length of the cohesive zone obtained with these properties, using Equation (4.5), is 0.63mm. A mesh size smaller than 0.2mm is needed in order to have three or more elements in the cohesive zone.

The predictions obtained using different levels of mesh refinement are shown in Figure 4.9. Using meshes coarser than 0.2mm, the experimental result is significantly overpredicted. For a mesh size equal to 0.5mm the maximum applied load is greater than two times the maximum load obtained with meshes smaller than 0.1mm.

The ultimate tensile strength calculated using a mesh size of 0.1mm is 404MPa. Delamination onset occurs when a point in the interface is not able to carry any traction, which changes the stress distribution. The stress distribution of the two interior layers of the laminate in a plane perpendicular to the interface and normal to the load direction are represented in Figure 4.10 for three stages of deformation. At the first stage, before delamination onset, the stresses σ_{zz} near the free edge are

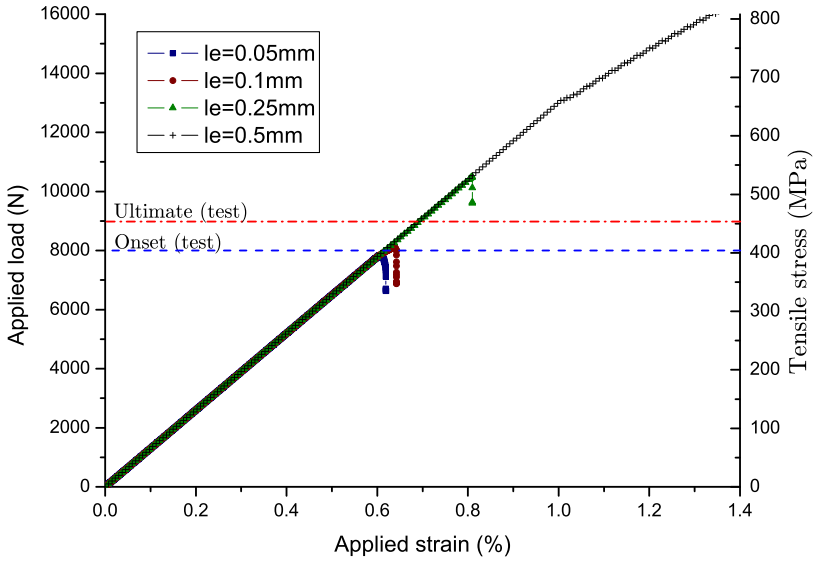

Figure 4.9: *Load-displacement curves obtained for a free-edge test with different mesh sizes using nominal interface strength properties.*

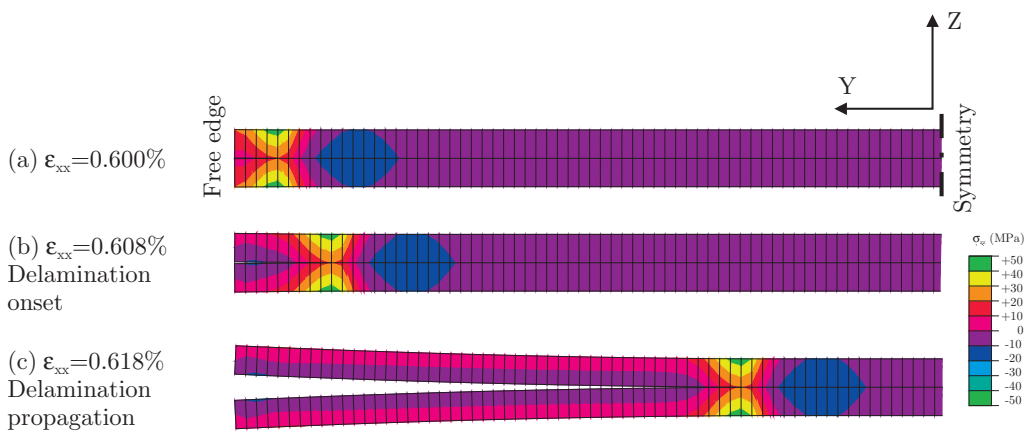

Figure 4.10: *Evolution of stresses during delamination onset and propagation of the two interior layers of the laminate.*

tensile due to the mismatch effect of the Poisson's ratio (red-lighter zones in Figure 4.10). At delamination onset, a region of the free edge is unable to carry load and

the stresses become compressive, as shown in Figure 4.10(b) (blue-darker zones).

Table 4.5: *Summary of predicted and experimental values of tension tests on T300/934 laminates.*

	Predicted	Experimental	Difference
Strain at delamination onset (%)	0.6	0.59	2%
Stress at delamination onset (MPa)	392	404	-3%
Ultimate strain (%)	0.6183	0.66	-6%
Ultimate strength (MPa)	409	459	-10%

The predicted onset of delamination is $\varepsilon_{xx} = 0.6\%$, and the corresponding stress is 392MPa. The experimental results obtained by Crossman and Wang [112] reported a delamination onset tensile stress of 409MPa and an ultimate tensile strength of 459MPa. The predicted and experimental onset and failure stresses and strains are summarized in Table 4.5. Unstable delamination propagation and the corresponding structural collapse occurs at a strain of 0.6183%.

To verify the effect of interface strength on the predicted results, simulations were performed by specifying the desired number of elements spanning the cohesive zone to be $N_e = 5$ and reducing the interface strength according to Equation (4.9). The load-displacement curves obtained for several levels of mesh refinement are shown in Figure 4.11.

A similar study of mesh size effect was repeated by selecting the desired number of elements spanning the cohesive zone to be $N_e = 10$. Although the results presented in Figures 4.12 and 4.13 for $N_e = 10$ are more accurate than those for $N_e = 5$, the improvement is insignificant when the element is smaller than 0.25mm.

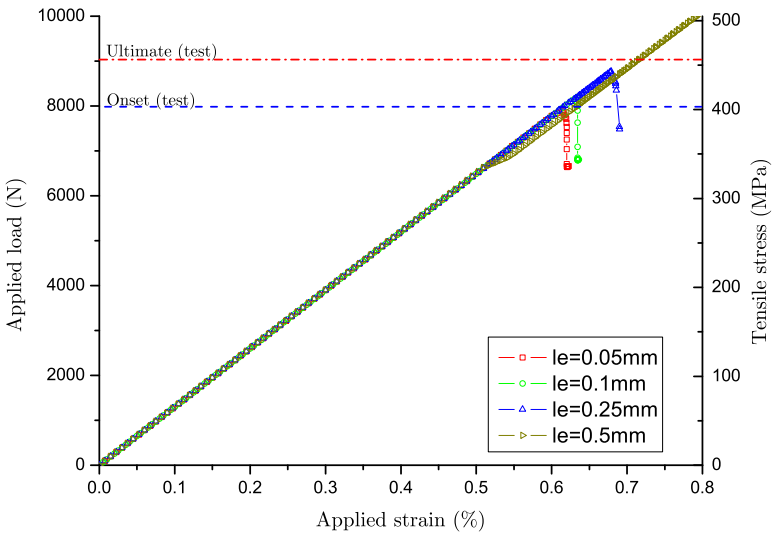

Figure 4.11: *Load-displacement curves obtained for a free-edge test with different mesh sizes and with the interface strength adjusted for* N_e *=5.*

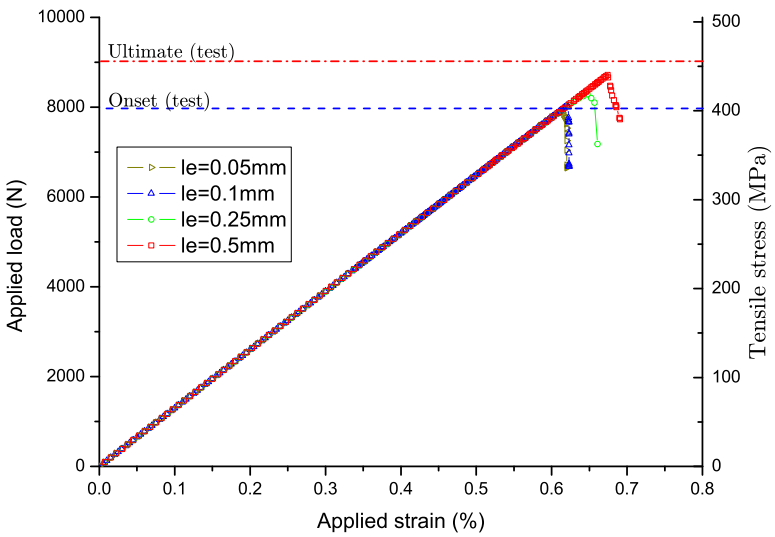

Figure 4.12: *Load-displacement curves obtained for a free-edge test with different mesh sizes and with the interface strength adjusted for* N_e *=10.*

Figures 4.12 and 4.13 show that the maximum load predicted by the numerical model converges to the same value when decreasing the element length. The maximum load predicted differs 12% of the experimental value. This difference can be justified by the increase of the fracture toughness associated with fiber bridging that is not taken into account in the model.

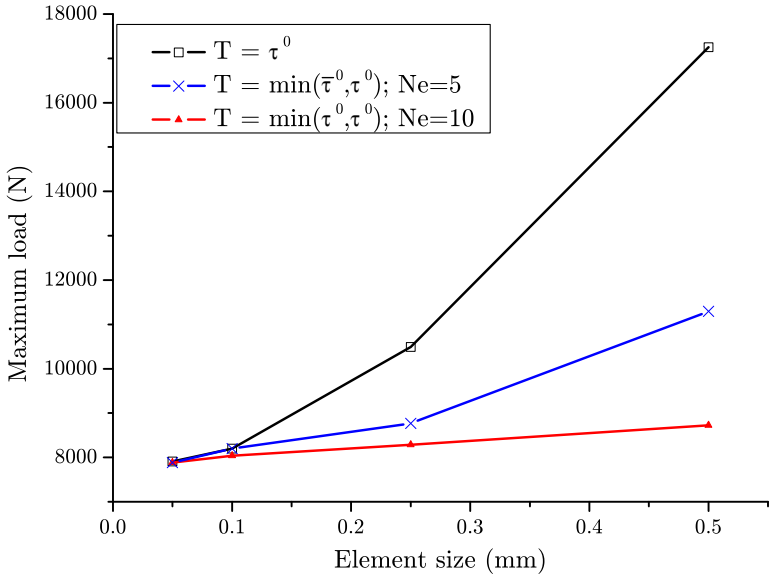

Figure 4.13: *Maximum load obtained in a free-edge test for three cases: a) with constant interfacial strength, b) and c) with interfacial strength calculated according to Eq.(4.9) with N_e equal to 5 and 10.*

4.5 Concluding remarks

An engineering solution for the simulation of delamination using coarse meshes was developed. Two new guidelines for the selection of the parameters for the constitutive equation used for the simulation of delamination were presented.

First, a new equation for the selection of the interface stiffness parameter K was derived. The new equation is preferable to previous guidelines because it results from

mechanical considerations rather than from experience. The approach provides an adequate stiffness to ensure a sufficiently stiff connection between two neighboring layers, while avoiding the possibility of spurious oscillations in the solution caused by overly stiff connections.

Finally, an expression to adjust the maximum interfacial strength used in the computations with coarse meshes was presented. It was shown that a minimum number of elements within the cohesive zone is necessary for accurate simulations. By reducing the maximum interfacial strength, the cohesive zone length is enlarged and the cohesive zone spans more elements. The results obtained by reducing the maximum interfacial strength show that accurate results can be obtained with a mesh ten times coarser than by using the nominal interface strength. The drawback in using a reduced interfacial strength value is that the stress concentrations in the bulk material near the crack tip are less accurate.

Part II

Delamination under fatigue loading

Chapter 5

Fatigue in composite materials

5.1 Fatigue modeling

Engineering components and structures often operate under cyclic, or fatigue, loading. Usually, fatigue loading is a result of sinusoidal stress cycles of nearly constant amplitude. The behaviour of composite materials is more complicated than the one of homogenous and isotropic materials such as metals. The inhomogeneity and anisotropy of their microstructure leads to complex damage mechanisms (e.g. fibre breakage, matrix cracking and yielding, fibre-matrix debonding and delamination). As a consequence, there are several differences between the fatigue behaviour of metals and fibre reinforce-composites [117].

In metals, a stage of gradual invisible deterioration spans nearly the complete life time without significant reduction of the stiffness. The final stage of the fatigue process starts with the formation of small cracks, which are the only form of a macroscopically observable damage. Gradual growth and coalescence of these cracks quickly produces a large crack and final failure of the structural component. As the stiffness of a metal remains almost unaffected, the linear relation between stress and strain remains valid and the fatigue process can be simulated in most common cases by a linear elastic analysis and linear elastic fracture mechanics.

In a fibre-reinforced composite material, damage starts very early and the extent of the damage zone grows steadily while the damage type in these zones may change (e.g. small matrix cracks leading to large size delaminations). The gradual deterioration of a fibre-reinforced composite– with a loss of stiffness in the damaged zones– leads to a continuous redistribution of stress and a reduction of stress concentrations inside the structural component.

There are diverse approximations to study the fatigue phenomena in composite materials. Introductions to this subject were presented in the reviews of Talreja [118, 119], Reifsnider [120], Sendeckyj, [121], Andersons [122], and Van Paepegem [117] can be useful. A classification of fatigue models and life time prediction methodologies for fatigue loading is difficult. Among other classifications [117, 121, 123], the classification used in this work defines three major categories: i) fatigue life models, which do not take into account the actual degradation mechanisms and use S-N curves or Goodman-type diagrams with some sort of fatigue failure criterion; ii) fracture mechanics models, which basically study the crack growth, and finally, iii) damage mechanics models which use one or more damage variables related to measurable manifestations of damage. Clearly, this classification is very concise and some of the models present in the literature may not be classified in any of these categories. The aim of this introduction is to present the most representative approaches which are useful to understand, and later develop, the new fatigue model.

5.1.1 Fatigue life models

Fatigue life models extract information from the S-N curves or Goodman-type diagrams and propose a fatigue failure criterion. Fatigue life models do not take into account damage accumulation, and predict the number of cycles corresponding to fatigue failure under fixed loading conditions. The first fatigue failure criteria were proposed by Hashin and Rotem [124]. The authors distinguished a fibre failure and a matrix-failure mode:

$$\sigma_{11} = S_1^u$$
$$\left(\frac{\sigma_{22}}{S_2^u}\right)^2 + \left(\frac{\tau_{12}}{S_{12}^u}\right)^2 = 1 \tag{5.1}$$

where σ_{11} and σ_{22} are the stresses along the fibres and transverse to the fibres, τ_{12} is the shear stress and S_1^u, S_2^u, and S_{12}^u are the ultimate tensile, transverse and shear stresses, respectively. The ultimate strengths are function of the fatigue stress level, stress ratio and number of cycles. Most of these fatigue life models are expressed by means of a failure criterion that is function of the ultimate strengths S_i. The evolution of the ultimate strengths can be written as [123]:

$$\frac{\partial S_i}{\partial N} = -\mathsf{f}\left(\sigma, R, S_i, N\right) \tag{5.2}$$

where R is a load-dependent parameter. The negative sign indicates that the ultimate strength always decreases. The function f is derived from the S-N curves that must be determined experimentally for each ply configuration.

5.1.2 Fracture Mechanics models

Fracture Mechanics models relate the variation of the energy release rate G -or of the stress intensity factor K- with the crack growth. Usually, fatigue loading is related to sinusoidal stress cycles of constant amplitude. These stress cycles are commonly characterized using the frequency, the mean stress value, and the load ratio of a load-dependent index, R, which is defined as the ratio of the minimum stress to the maximum stress during the loading cycle. The stress intensity factor range and the energy release rate range may be defined respectively as:

$$\begin{aligned} \Delta K &= K^{\max} - K^{\min} = (1-R)K^{\max} \\ \Delta G &= G^{\max} - G^{\min} = (1-R^2)G^{\max} \end{aligned} \tag{5.3}$$

Crack growth rate is defined as the crack extension per number of cycles. The fatigue crack propagation rate is denoted by $\frac{\partial A}{\partial N}$, where A is the crack area. The correlation of the fatigue crack growth rate with the amplitude of the energy release rate (or stress intensity factor) is commonly represented in a log-log diagram where it displays a sigmoidal trend, as shown in Figure 5.1. The curve can be divided into three zones or regions according to the curve shape. In Region I there is a threshold value, K_{th} or G_{th}, below which cracks do not propagate or additional crack growth is negligible. Above this value, the crack growth increases relatively quickly. Region II defines a stable crack growth zone generally characterized by a linear part of the curve in a log-log plot. Finally, in Region III the crack growth rate curve rises to an asymptote that corresponds to the critical fracture toughness values, K_c or G_c, where static fracture is achieved.

There are some empirical or semi-empirical attempts to describe all regions of the crack propagation rate curve by different crack growth laws. However, only the Paris law [125, 126] is widely used and accepted. Paris law describes only the linear portion of the curve (Region II). According to this law, the crack growth rate is related to the energy release rate range by a power law that can be expressed as[127]:

$$\frac{\partial A}{\partial N} = C\left(\frac{\Delta G}{G_c}\right)^m \tag{5.4}$$

where the parameters C and m depend on the mode-ratio and they must be determined experimentally. The energy release rate range, ΔG, depends on the loading conditions, and G_c is the fracture toughness of the material.

Alternatively, the crack growth rate may be expressed in terms of the stress intensity factor, ΔK, or the J-integral range ΔJ [128, 129].

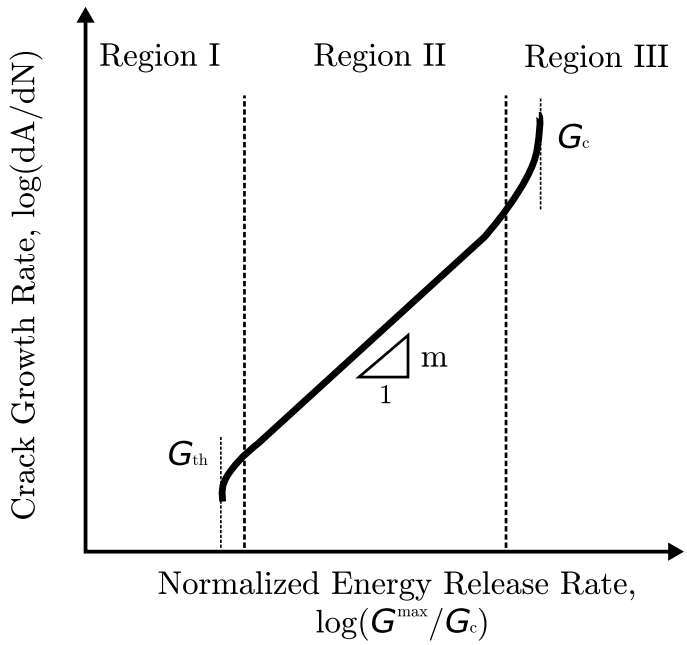

Figure 5.1: *Typical crack growth rate pattern.*

5.1.3 Damage Mechanics models

Damage Mechanics methods to analyze fatigue use a damage variable that evolves with the number of cycles. This is the case for cohesive zone models, as that used in this work. The material separation under cyclic loading is described by a constitutive equation formulated in the context of the thermodynamics of irreversible processes. Among other classifications, the models developed in the Damage Mechanics context can be classified in two different groups [130]: high-cycle fatigue models and low-cycle fatigue models.

Low-cycle fatigue

According to Lemaitre et al. [130], low-cycle fatigue occurs when the damage is localized in domains of stress concentrations but it can be measured and evaluated at the mesoscale. The number of cycles to failure is smaller than 10^4.

Low-cycle fatigue models account for fatigue damage evolution on a cycle by

cycle analysis defining, in most of the models, an evolution of the damage variables during the unloading paths.

Within the context of the cohesive zone model (CZM), there exist several attempts to extend cohesive laws for monotonic loading into forms suitable for cyclic loading. Yang et al. [131] developed a cohesive law that describes separately unloading and reloading, which artificially creates a hysteresis loop between unloading and reloading paths. Roe and Siegmund [132] describe fatigue crack growth by incorporating a damage evolution equation due to cyclic loading. Nguyen et al. [133] developed a cohesive zone model in which the irreversible material degradation is due to a degradation of the stiffness of the cohesive zone during the unloading path. In a similar way, Vinay et al. [134] extended their cohesive constitutive law previously developed [48] to account for fatigue damage accumulation during the unloading path. In all of these references, the fatigue damage accumulation is accounted for in a cycle-by-cycle analysis.

High-cycle fatigue

According to Lemaitre et al. [130], high-cycle fatigue occurs when the damage is localized at the microscale as a few micro-cracks. The number of cycles to failure is greater than 10^4.

For high-cycle fatigue, a cycle-by-cycle analysis is computationally impractical. Therefore, a two scale computation is usually adopted [135, 136]: The damage evolution is first calculated and later extrapolated for a given number of cycles. With this strategy (also called cycle-jump strategy), the computation of the whole load history is reduced to a selected number of cycles and extrapolated for the rest of the load history. Thus, an evolution law of the damage variable (or mechanical properties) as a function of the number of cycles has to be initially established, to later extrapolate it and jump a given number of cycles. In summary, in the formulation of a high-cycle fatigue model a cycle-jump strategy and an evolution law of the damage variable (or for the mechanical properties) as a function of the

number of cycles have to be defined.

- Cycle jump strategy

  The cycle-jump strategy has to control the accuracy of the solution by means of the length of the cycle jump. There are different approaches in the literature to control the accuracy of the solution. For instance: Van Paepegem, [137] computed the cycle-jump length by limiting the maximum increment of the damage variable at each cycle-jump. Mayugo [123] developed a similar cycle jump strategy were the evolution of the mechanical properties is controlled before cycle-jump until a constant evolution is assured. Cocojaru [138] presented a similar model with an improved control of the cycle jump length.

- Fatigue damage evolution law

  There are several expressions relating the damage variable (or mechanical properties) to the number of cycles. Most of the models use a phenomenological law established a priori and formulated as a function of the number of cycles. The damage evolution law is a function of several parameters that have to be adjusted to calibrate the numerical model with experimental results, usually by trial and error. An example of these models is the Peerling's law [139]:

$$\frac{\partial \mathsf{d}}{\partial N} = C e^{\Lambda \mathsf{d}} \varepsilon_a^{\beta} \tag{5.5}$$

  where C, Λ and β are parameters to be determined by means of experimental data and ε_a is a norm of strains.

  This law has been adapted successfully to simulate high cycle fatigue by means of an irreversible cohesive zone model [140, 141], but it has shown that the use of Peerling's model is only valid to simulate Region II crack growth regimes, and it is not sensitive to stress ratio variations. Robinson and co-workers [141] recently improved Peerling's law to account for variations in the stress ratio.

5.2 Fatigue delamination of composite laminates

5.2.1 Introduction

Few models have been developed to simulate delamination propagation under cyclic loading. This is apparently due to the complexity of the problem: the material at the crack tip vicinity is strongly inhomogeneous and anisotropic. Moreover, a common feature at the crack tip in polymer-matrix composites is the development of a damage zone accompanying the macrocrack. The damage zone consists of fibre debonds, side cracks, and a process zone of intense matrix microcracking at the crack tip. Such a feature provides the grounds for speculation that a certain level of damage is actually needed for the delamination to propagate. Thus, delamination under fatigue conditions basically involves the same micro mechanisms and processes that occur under static loading: there is an initiation or onset process of the delamination and a crack growth or propagation process due to the fatigue loading. Most of the studies are devoted to the issue of the interlaminar crack propagation; fatigue delamination onset has received less attention. One of the studies focused on fatigue delamination onset is the work of O'Brien [142] in which a $[35/-35/0/90]_s$ AS4 graphite-reinforced PEEK thermoplastic matrix composite (a toughened composite) was compared to various untoughened composites of the same lay-up. Delamination onset that always occurred at the 0/90 interface was characterized at different cyclic load levels. The results show how the critical energy release rate for the delamination onset reduce as a function of cycles.

5.2.2 Fatigue growth of interlaminar cracks

As previously mentioned, most of the fatigue delamination studies are devoted to the progressive growth of interlaminar cracks under cyclic loading. The crack growth is studied as a function of the number of cycles for a certain stress ratio, R. Usually, the Paris law, commonly used for fatigue of metals and progressive crack growth,

is used to describe the delamination growth rate as a power law function of the applied energy release rate range. The exponent m of the Paris law Equation (5.4) for composite materials can be about an order of magnitude larger than most metallic materials [143, 150]. Therefore, the predicted propagation rate is very sensitive to the accuracy of the estimated energy release rates. In Equation (5.4), ΔG does not discriminate the individual contribution of the different modes. For pure modes (mode I, II and even III) experimental individual propagation parameters must be determined. For mixed-modes, either the parameters are determined experimentally or they are inferred from the propagation parameters for pure modes. As in the static case, the DCB test is the most used experimental method for the study of fatigue delamination in pure mode I. However, O'Brien [142] used a multidirectional free edge specimen to characterize the critical energy release rate under fatigue loading.

Load ratio effect

The rate of delamination growth depends on the load ratio, R, defined as the ratio of the minimum to the maximum stress intensity factors (or the energy release rate) values during load cycle [144, 146]. Several empirical relations have been developed to account for the R effect in delamination fatigue. The proposed relations can be divided in two groups: either an effective loading parameter is sought in terms of which crack rate data at different stress ratios form a mastercurve, or explicit expressions for Paris law parameters as a function of R are developed. Some references for both categories are shortly described in the following.

Gustafson and Hojo [144] studied the fatigue propagation of interlaminar cracks for various stress ratios under mode I and mixed-mode I/II. The existence of fatigue thresholds was observed, which was almost constant for mode I and R-dependent for mixed–mode. The mode I crack propagation rate data for the three different stress ratios considered showed a great R-dependence when plotted versus $G^{\max}$. However, the crack propagation data could be fitted by a single curve when plotted against ΔG. The mixed–mode data deviated from a power law function when plotted versus

$G^{\max}$, but showed a mild R-dependence when plotted against ΔG.

Hojo et al. [145] studied the delamination crack growth in mode I of two different graphite/epoxy laminates at room temperature. The authors used the DCB test to study the effect of the stress ratio, R, on the fatigue propagation of the crack. The experimental crack propagation rate data was plotted versus the stress intensity range, ΔK, the maximum value of the energy release rate, $G^{\max}$, and the energy release rate range, ΔG, for various R ratios. Different power laws were obtained for values above the thresholds. It was shown that the growth rate increased with increasing R values when correlated to ΔK. The observed tendency was reversed if the experimental growth rates were correlated to $G^{\max}$. On the other hand, the plots showed that the effect of R was smaller if the crack propagation rates were correlated to ΔG, especially for one of the considered materials. Nevertheless, some dependence was still observed. Therefore, in the representation of the crack growth rate versus ΔK, $G^{\max}$ and ΔG, different curves could be adjusted for different values of R. A common trend could not be inferred. The fractographic analysis of the fracture surfaces revealed that for one of the laminates the fracture was matrix dominated because no fibre bridging was observed. No significant differences between static and fatigue fracture surfaces were appreciable. On other laminate, the fracture process was dominated by interfacial debonding. The interfacial debonding was more pronounced for static fracture surfaces than in fatigue fracture surfaces. On the basis of these fractographic evidences, a new parameter was defined for a better correlation of the experimental data. The so-called equivalent stress intensity factor range, ΔK_{eq}, was given by:

$$\Delta K_{eq} = \Delta K \left(1 - R\right)^{-\gamma} = \Delta K^{1-\gamma} K_{max}^{\gamma} \tag{5.6}$$

where γ, the stress-ratio-effect parameter, is an empirical factor ranging from 0 to 1. The parameter γ indicates the relative contribution of the maximum stress to the cyclic stress in determining the crack growth rate. When the value of γ is near zero, ΔK is the fracture controlling parameter. For values of γ near the unity,

the fracture controlling parameter is $G^{\max}$. The results show that $G^{\max}$ dominated the fractures, which would explain the slight differences between static and fatigue fracture surfaces. The results clearly show the existence of a unique curve for all the R values considered for each material when the crack propagation rate is represented versus ΔK_{eq}.

Matsuda et al. [147] investigated the fatigue crack growth behaviour under mode II for various stress ratios in a carbon/epoxy interlayer-toughened laminate. The fatigue thresholds were found to be higher than fatigue thresholds of conventional carbon/epoxy laminates. The value of the stress-ratio-effect parameter, γ, was almost zero near the threshold and increased with increasing the crack growth rate. The maximum value of γ was 0.3, indicating that the fracture mechanism was controlled by ΔK. The analysis of the fracture surfaces showed very rough surfaces with traces of peeled out fibres and hackles for the static case. The features of the fatigue surfaces depended on the propagation rate. The differences in the surfaces between high propagation rates and quasi-static tearing were small. Near the thresholds, rather flat fracture surfaces were observed.

Tanaka and Tanaka [148] studied the dependence of the fatigue crack growth rate under mixed-mode loading on R. For all the stress ratios considered on the study, the exponent of the Paris law increased with increasing values of R. The authors also found that at high propagation rates the dominant parameter is $G^{\max}$, and ΔG controlled the fracture process near the fatigue thresholds. In a later study [149], the authors investigated the effect of the stress ratio on the propagation behaviour of mode II fatigue delaminations. The value of the threshold increased with increasing values of R.

Schön [150] proposed a model for the calculation of fatigue propagation of laminate delaminations. The model is based on the determination of the two parameters of the Paris law. Therefore, two points of the fatigue delamination growth rate curve must be determined experimentaly. One of the points corresponds to the threshold, which was found to occur for a constant change in energy release rate. The

second point is related to the static interlaminar fracture. In total, five different material parameters are needed for the model. The parameters of the Paris law were formulated for any energy release rate mode and stress ratio. The model was formulated in such a way that the Paris law exponent decreases with decreasing R values and increases with mode II contributions. This behaviour was found to be in good agreement with experimental results from the literature.

Andersons et al. [151] deduced a one-dimensional model for the prediction of fatigue delamination under mixed-mode loading conditions. The proposed model relates the fatigue delamination growth to the damage process ahead of the crack tip. Fatigue damage accumulation was taken into account by means of the Miners rule. The authors considered that the stress ratio in mode I is limited to tension-tension loading, $0 < R < 1$, while the range of interest in mode II admits load reversals, $-1 < R < 1$. Then, the dependence of the Paris law parameters on the stress ratio was approximated by a linear Goodman diagram. The crack growth rate model was proposed as a function of the stress intensity factors where the mixed-mode parameters must be determined from the mode I and mode II parameters. According to the authors, the model is formulated as a function of K because plasticity effects can be neglected for brittle matrix composites and the stress within the process zone ahead of the crack tip can be taken proportional to K. Moreover, if fibre bridging appears, the effects can be included by reducing the value of K.

A new one-dimensional empirical model was proposed by Andersons et al.[152] to account for the stress ratio effect on the fatigue crack growth rate on composite laminates. As in the previous model, the same Miners accumulation rule was used to relate the crack propagation rate with the damage accumulation ahead of the crack tip. Furthermore, the dependence of the Paris law parameters on the stress ratio was also approximated by a linear Goodman diagram. The model was also formulated in terms of K for the same reasons exposed before. However, Anderson's model only considers pure mode loading and two different power law expressions for the crack growth rate were derived for mode I and mode II. The expression for mode I crack

growth was formulated in function of R and the value of the stress intensity factor range at the threshold. The expression for mode II propagation was also formulated in function of the stress intensity factor range at the threshold. However, the authors considered that the effect of R on the stress intensity factor range at the threshold is negligible and the latter function does not depend on the value of the stress ratio. Experimental crack growth rate data of brittle and toughened epoxy and tough PEEK matrix laminates obtained from the literature were compared to both power laws and good agreement was encountered.

5.2.3 Simulation of fatigue delamination of composite laminates

There are several models to simulate fatigue delamination of composite laminates. The most representative models classified in the three three categories cited above (fatigue life models, fracture mechanics models, and damage mechanics models) are described in the following subsections:

Fatigue life models

There are few fatigue life models available in the open literature. The most representative is the work done by Krueger et al. [153, 154] for delamination onset under fatigue loading. The methodology is based in the creation of a failure surface relating the total energy release rate, G^{max}, the mode-ratio, $\frac{G_{\mathrm{II}}}{G_{\mathrm{T}}}$, and the number of cycles to delamination onset, N (Figure 5.2). The failure surface was fitted through data from fatigue experiments.

Once this failure surface was created the total energy release rate and the mode-ratio was determined for an arbitrary maximum cyclic load using the Virtual Crack Closure Technique (VCCT) [19]. The associated fatigue life, N, for delamination onset was obtained directly from the fatigue failure surface.

This methodology can be useful for strength analysis but it is not appropiated to

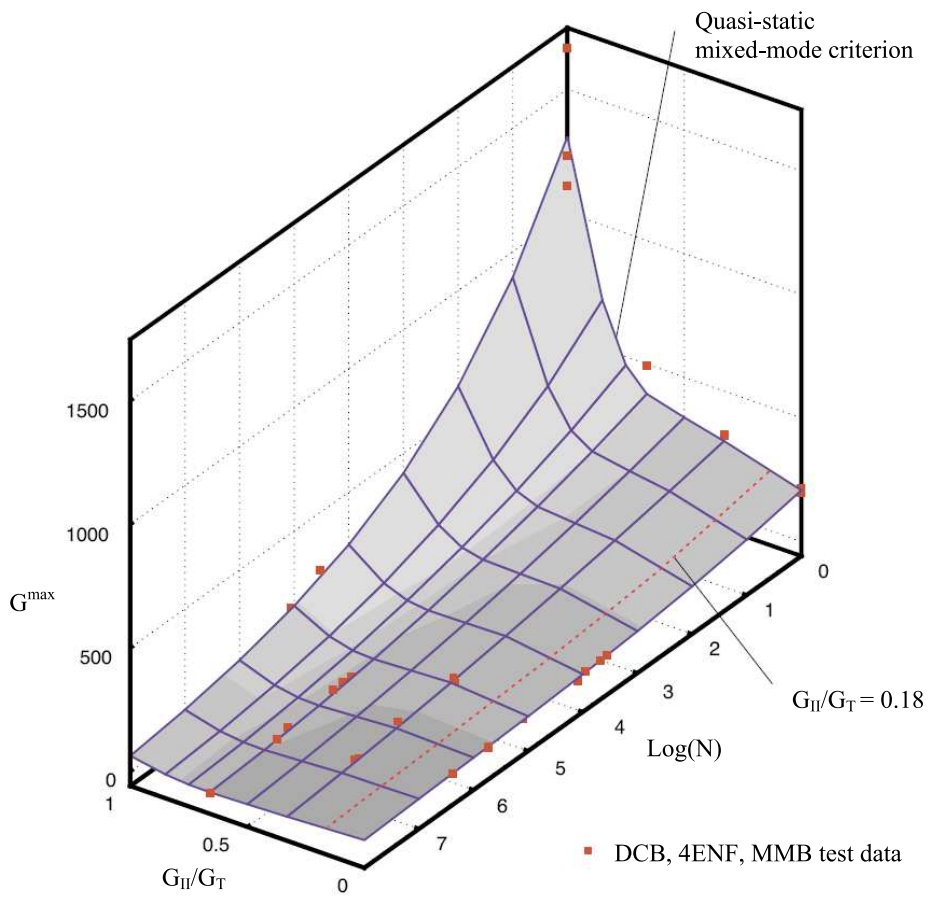

Figure 5.2: *Delamination onset surface for IM7/8552 mixed-mode I/II fatigue failure [154].*

analyze the damage tolerance of the structure. Moreover, the methodology assumes linear elastic behaviour of the material before delamination onset and it is not able to capture changes in the mechanical behaviour during the loading history before the fatigue life is achieved.

Fracture Mechanics models

Most of the descriptions of the fatigue delamination in laminated composites use the Paris Equation (5.4) to represent the fatigue crack growth rates. However, the Paris equation is limited to delamination growth in Region II. Moreover, the Paris law parameters strongly depend on mode-ratio and load ratio. Thus, the

predictive capability of the model is restricted to the same loading conditions as those used to obtain the experimental data used to fit the Paris law. To extend the range of validity of the law, several equations have been proposed. The different approximations to the description of the crack growth rate accounting for mixed-mode loading can be classified into three groups: a) crack growth rate description of the fatigue propagation of the interlaminar crack by the addition of the individual propagations in mode I and mode II [144, 155]; b) crack growth rate description of the interlaminar crack propagation by a function of the individual propagations in mode I and mode II [156, 157]; c) crack growth rate description of the interlaminar crack by a monotonic function of the mixed-mode critical energy release rate [151, 158]-[162].

A fatigue crack growth rate description that assumes that the mode I and mode II contributions of crack growth rate are additive was proposed by Ramkumar and Whitcomb [155] as well as Gustafson and Hojo [144]. Ramkumar and Whitcomb proposed the following equation to describe the mixed-mode dependence:

$$\frac{\partial A}{\partial N} = C_{\mathrm{I}} \left(\frac{G_{\mathrm{I}}}{G_{\mathrm{I}c}} \right)^{m_{\mathrm{I}}} + C_{\mathrm{II}} \left(\frac{G_{\mathrm{II}}}{G_{\mathrm{II}c}} \right)^{m_{\mathrm{II}}} \tag{5.7}$$

where C_i and m_i are the propagation parameters in mode I and mode II and G_i indicates the maximum energy release rate in mode I and mode II. Gustafson and Hojo [144] proposed a similar equation replacing $\frac{G_i}{G_{ic}}$ by ΔG_i. However, these descriptions do not correlate well with experimental data under mixed-mode loading conditions.

A model for fatigue propagation of the interlaminar crack based on a function of the individual propagations in mode I and mode II was proposed by Russell and Street [156], who suggested a rule of mixtures relation linking the Paris law parameters under single-mode and mixed-mode loading, and using relative energy release rates, G_{I}/G_T and G_{II}/G_T as weight factors:

$$\frac{\partial A}{\partial N} = \frac{G_{\mathrm{I}}}{G_T} C_{\mathrm{I}} + \frac{G_{\mathrm{II}}}{G_T} C_{\mathrm{II}} \left(\frac{\Delta G_{\mathrm{I}}}{G_{\mathrm{I}c}} + \frac{\Delta G_{\mathrm{II}}}{G_{\mathrm{II}c}} \right)^{\frac{G_{\mathrm{I}}}{G_T} m_{\mathrm{I}} + \frac{G_{\mathrm{II}}}{G_T} m_{\mathrm{II}}} \tag{5.8}$$

Another description was proposed by Dhalen and Springer [157], which is based on a semi-empirical model to estimate the fatigue crack growth under mixed-mode. The model also employed a rule of mixtures type of relationship, but based their semi-empirical relations on a dimensional analysis using the Buckingham π theorem.

The third group, where the crack growth rate description of the interlaminar crack is described by a monotonic function of the mixed-mode critical energy release rate, comprises additional references. Kardomateas and co-workers [158, 159] proposed that the crack rate equation parameters be expressed in terms of mode-ratio following the same form as that for the fracture toughness

$$\frac{\partial A}{\partial N} = C_m \frac{\left(\frac{\Delta G}{G_c}\right)^{m_{\mathrm{m}}}}{1 - \frac{G}{G_c}} \tag{5.9}$$

$$G_c = G_{\mathrm{I}c} \left(1 + \left(\frac{G_{\mathrm{I}c}}{G_{\mathrm{II}c}} - 1 \right) \sin^2 \psi \right)^{-1} \tag{5.10}$$

$$C_m = C_{\mathrm{I}} \left(1 + \left(\frac{C_{\mathrm{II}}}{C_{\mathrm{I}}} - 1 \right) \sin^2 \psi \right) \tag{5.11}$$

$$m_{\mathrm{m}} = b_I \left(1 + \left(\frac{m_{\mathrm{II}}}{m_{\mathrm{I}}} - 1 \right) \sin^2 \psi \right) \tag{5.12}$$

where ψ indicates the mixed-mode angle defined as [161]:

$$\psi = \tan^{-1} \frac{K_{II}}{K_I} \tag{5.13}$$

Kenane and Benzeggagh [162] proposed a semi-empirical fatigue criterion based on a description of the Paris Law parameters, C and m, as a function of the mode-ratio:

$$\log C_{\mathrm{m}} = \log C_{\mathrm{II}} + (\log C_{\mathrm{I}} - \log C_{\mathrm{II}}) \left(1 - \frac{G_{\mathrm{II}}}{G} \right)^b \tag{5.14}$$

$$m_{\mathrm{m}} = m_{\mathrm{II}} + (m_{\mathrm{I}} - m_{\mathrm{II}}) \left(\frac{G_{\mathrm{II}}}{G} \right)^{b_1} \tag{5.15}$$

where G is the mixed-mode energy release rate, and b and b_1 are material parameters that must be determined experimentally.

Andersons et al. [151] suggested a similar model, with a modified Paris Law equation written as a function of the stress intensity factors:

$$\frac{\partial A}{\partial N} = C_{\mathrm{m}} \left(\left(\frac{K_I}{K_{Ic}} \right)^2 + \left(\frac{K_{II}}{K_{IIc}} \right)^2 \right)^{\frac{m_{\mathrm{m}}}{2}} \tag{5.16}$$

where

$$C_{\mathrm{m}} = \frac{m_{\mathrm{m}}}{m_{\mathrm{m}} - 2} \frac{\frac{m_{\mathrm{I}}-2}{m_{\mathrm{I}}} \left(\frac{\sin\psi}{K_{Ic}} \right)^2 m_{\mathrm{I}} + \frac{m_{\mathrm{II}}-2}{m_{\mathrm{II}}} \left(\frac{\cos\psi}{K_{IIc}} \right)^2 m_{\mathrm{II}}}{\left(\frac{\sin\psi}{K_{Ic}} \right)^2 + \left(\frac{\cos\psi}{K_{IIc}} \right)^2} \tag{5.17}$$

and

$$m_{\mathrm{m}} = \frac{\frac{m_{\mathrm{I}}-2}{m_{\mathrm{I}}} \left(\frac{\sin\psi}{K_{Ic}} \right)^2 m_{\mathrm{I}} + \frac{m_{\mathrm{II}}-2}{m_{\mathrm{II}}} \left(\frac{\cos\psi}{K_{IIc}} \right)^2 m_{\mathrm{II}}}{\frac{m_{\mathrm{I}}-2}{m_{\mathrm{I}}^2} \left(\frac{\sin\psi}{K_{Ic}} \right)^2 m_{\mathrm{I}} + \frac{m_{\mathrm{II}}-2}{m_{\mathrm{II}}^2} \left(\frac{\cos\psi}{K_{IIc}} \right)^2 m_{\mathrm{II}}} \tag{5.18}$$

More recently, Blanco et al. [9, 163] proposed a new model similar to Kenane and Benzeggagh [162], but with a polynomial description of the variation of the Paris Law parameters with the mode-ratio that describes more accurately the experimental data of mixed-mode dependency:

$$\log C = \log C_{\mathrm{I}} + \left(\frac{G_{\mathrm{II}}}{G} \right) \log C_{\mathrm{m}} + \left(\frac{G_{\mathrm{II}}}{G} \right)^2 \log \frac{C_{\mathrm{II}}}{C_m C_{\mathrm{I}}} \tag{5.19}$$

$$m = m_{\mathrm{I}} + m_{\mathrm{m}} \left(\frac{G_{\mathrm{II}}}{G} \right) + (m_{\mathrm{II}} - m_{\mathrm{I}} - m_{\mathrm{m}}) \left(\frac{G_{\mathrm{II}}}{G} \right)^2 \tag{5.20}$$

Note that all of these laws represent the dependency of the parameters of the Paris Law equation with the mode mixity, but they do not take into account the stress ratio effect previously reported.

Damage Mechanics models

Few damage models have been proposed to simulate fatigue delamination of laminated composites. Andersons et al. [151] deduced a one-dimensional model for the prediction of fatigue delamination under mixed-mode loading conditions. The proposed model relates the fatigue delamination growth to the damage process ahead of the crack tip. Fatigue damage accumulation was taken into account by means of the Miner's rule.

$$\frac{\partial \mathsf{d}}{\partial N} = \frac{1}{N\left(\sigma_m, \Delta\sigma\right)} \tag{5.21}$$

where the function $N\left(\sigma_m, \Delta\sigma\right)$ is the S-N curve, and relates to the microcrack initiation in the interlaminar region. The authors used an exponential function:

$$N\left(\sigma_m, \Delta\sigma\right) = B\sigma_{ef}^{-b} \tag{5.22}$$

where B and b are parameters that must be fitted to experimental data and σ_{ef} is a stress norm of the stresses over one load cycle.

Goyal et al. [134] extended their cohesive-decohesive constitutive law [48] to account for interfacial damage accumulation due to fatigue loading, which was assumed to accumulate during unloading. They assumed that crack growth rate per cycle is equal to the damage growth rate per cycle:

$$\frac{\partial A}{\partial N} = \frac{\partial \mathsf{d}}{\partial N} \tag{5.23}$$

Fatigue damage degradation is introduced in the model during the unloading parts of the cycle: During the loading part of a load cycle, the damage evolution is simulated with the quasi-static model, while the damage evolution due to fatigue loading is accounted for during the unloading part of the loading cycle with the following equation:

$$\frac{\partial \mathsf{d}}{\partial N} \approx \mathsf{d}_{N+1} - \mathsf{d}_N = C\left(\Delta^{\max} - \Delta^{\min}\right)^m \tag{5.24}$$

where C and m are parameters that must be fit with experimental data.

Robinson and co-workers [140], as mentioned above, successfully adapted Perlings' law to simulate high cycle fatigue by means of an irreversible cohesive zone model. The equation proposed was:

$$\frac{\partial \mathsf{d}}{\partial N} = \frac{C}{1+\beta} e^{\Lambda \mathsf{d}} \lambda^{1-\beta} \tag{5.25}$$

where λ is a norm of the displacement jump. The model is only valid for Region II crack growth rates, and it is not sensitive to stress ratio variations. Robinson and co-workers recently [141] improved Peerling's law to account for variations in the load ratio by multiplying the parameter C by the factor $(1 - R^2)$.

Note that in both Robinson's models, the damage evolution laws are established a priori, independently of the crack growth description, and they are expressed as a function of several parameters that have to be adjusted through a trial-and-error calibration of the whole numerical model. Moreover, both models are only valid in Region II crack growth rate.

Requirements for a the formulation of a fatigue model

In summary, none of the models proposed in the literature to simulate delamination under fatigue loading account for the load ratio. The adjustment of the parameters of the damage evolution law have to be changed when the mode changes. Moreover, most of the models proposed in the literature can reproduce only the Region II of the typical crack growth rate pattern.

A successful fatigue model for the simulation of delamination should be a function of the following: (a) the load ratio R; (b) the mode-ratio; (c) the model has to reproduce the three regions of the typical crack growth rate pattern.

Moreover, to facilitate the widespread use of the model, the calibration of the

numerical model should be as simple as possible, and have to be implemented in numerical methods normally used in the design of structures (such the Finite Element Method), and accessible to the majority of the designers.

Chapter 6

Simulation of delamination in composites under high-cycle fatigue loading

6.1 Introduction and motivation

A new fatigue damage model for cohesive elements is proposed here. The approach is based on the assumption that the evolution of damage derives from a Fracture Mechanics description of the fatigue crack growth rate and it is formulated using the cohesive zone model concept. The constitutive damage model previously developed described earlier in this report is enhanced to incorporate a damage evolution law for high-cycle fatigue damage.

In the present model for fatigue damage, the evolution of the damage variable associated with cyclic loading is derived by linking a Fracture Mechanics description of the fatigue crack growth rate to Damage Mechanics. The model relates damage accumulation to the number of load cycles while taking into account the loading conditions (load ratio, R, energy release rate, G, and fracture mode-ratio). When used in a structural analysis, the model can simulate the dependence of the crack

growth rate on these parameters. In addition to the Paris Law crack growth regime, the model also exhibits a threshold capability for no growth in addition to quasi-static tearing.

The new fatigue damage model is implemented as a user-written element in ABAQUS [75] by means of a new damage evolution law implemented in the cohesive finite element previously developed.

6.2 Cohesive Zone Model approach

As mentioned herein, cohesive damage zone models relate tractions, τ, to displacement jumps, $\bar{\Delta}$, at an interface where a crack may occur. Damage initiation is related to the interfacial strength, τ^o. When the area under the traction-displacement jump relation is equal to the fracture toughness, G_c, the traction is reduced to zero and new crack surfaces are formed. If a linear softening law is used, the new crack surfaces are completely formed when the displacement jump is equal to, or greater than, the final displacement jump, $\bar{\Delta}^f$ (see Figure 6.1):

$$\begin{cases} \tau = (1 - \bar{\mathsf{d}})\tau^o & \bar{\Delta} < \bar{\Delta}^f \\ \tau = 0 & \bar{\Delta} \geq \bar{\Delta}^f \end{cases} \tag{6.1}$$

In the cohesive damage model, the damage variable $\bar{\mathsf{d}}$ describes the density of microcracks of a representative element surface. Then, the damage variable can be interpreted as the ratio of the damaged area, A_{d}, with respect to the area A^e associated with the local discretization [166]. In the context of finite elements, the area A^e represents the area of the element (or that of an integration point). Using the linear softening law represented in Figure 6.1, this ratio is a function of the energy dissipated during the damage process, Ξ, and of the critical energy release rate, G_c. Using Equation (6.1), the damage variable can be expressed as:

$$\bar{\mathsf{d}} = \frac{A_{\mathsf{d}}}{A^e} = \frac{\Xi}{G_c} \tag{6.2}$$

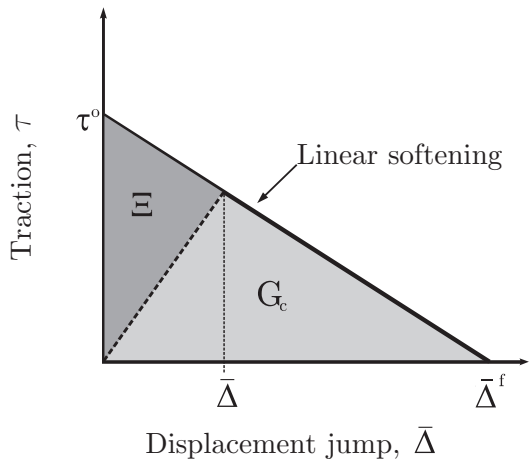

Figure 6.1: *Linear softening law for a cohesive zone model approach.*

6.2.1 Numerical implementation of to the CZM

The bilinear cohesive law is similar to the softening law of the CZM but with an initial linear elastic response before damage initiation, as shown in Figure 6.2. This linear elastic part is defined using a penalty stiffness parameter, K, that ensures a stiff connection between the surfaces of the material discontinuity. The interfacial strength and the penalty stiffness define an onset displacement jump, Δ^o, related to the initiation of damage. The equivalence between the constitutive equations of the physical cohesive zone model and the numerical constitutive equations is shown in Figure 6.2.

The relation between the physical and numerical model is straightforward: Under loading conditions ($\lambda = \Delta$), using equations (3.24) to (3.31) the damage variable can be written as:

$$\mathsf{d} = \frac{\Delta^f(\Delta - \Delta^o)}{\Delta(\Delta^f - \Delta^o)} \tag{6.3}$$

In the numerical model of the CZM, the damage variable d represents a loss of stiffness and, therefore, it is not equivalent to $\bar{\mathsf{d}}$, the ratio between the damaged area, A_{d}, with respect to the area of the element, A^e, in Equation (6.2). Since $\bar{\mathsf{d}}$ is

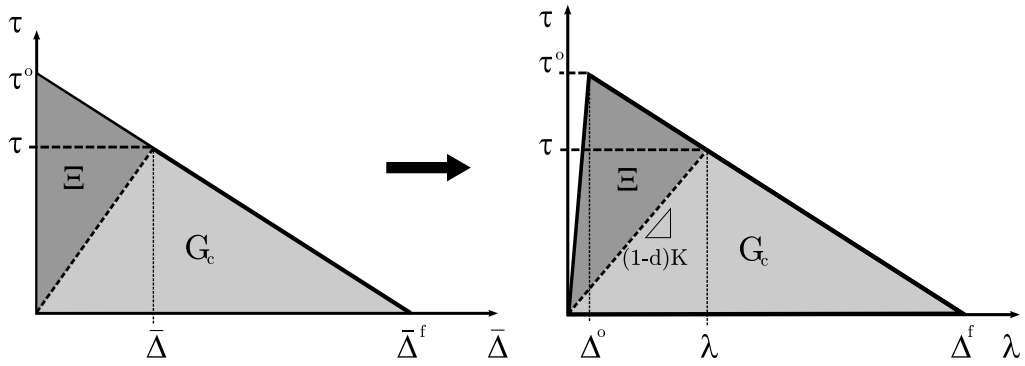

Figure 6.2: *Equivalence between the physical (left) and numerical (right) constitutive equation of the CZM.*

equal to the ratio of the energy dissipated over the fracture toughness the damaged area ratio is related to the damage variable, d, as:

$$\bar{\mathsf{d}} = \frac{A_{\mathsf{d}}}{A^e} = \frac{\Xi}{G_c} = 1 - \frac{\lambda}{\Delta^o}(1 - \mathsf{d}) \tag{6.4}$$

By solving Equation (6.3) for λ and substituting into Equation (6.4), the damaged area ratio becomes:

$$\frac{A_{\mathsf{d}}}{A^e} = \frac{\mathsf{d}\Delta^o}{\Delta^f(1 - \mathsf{d}) + \mathsf{d}\Delta^o} \tag{6.5}$$

6.3 Constitutive model for high-cycle fatigue

The damage evolution that results from a general loading history can be considered as the sum of the damage created by the quasi-static overloads and the damage created by the cyclic loads:

$$\dot{\mathsf{d}} = \dot{\mathsf{d}}_{static} + \dot{\mathsf{d}}_{cyclic} \tag{6.6}$$

The first term in the right hand side of Equation (6.6) is obtained from the equations presented in Chapter 3, while the second term has to be defined to account for cyclic loading. Using a Damage Mechanics framework, several authors have formulated the damage evolution that results from cyclic loads in terms of the number of cycles and of the strains (or displacement jumps) [139, 140, 141]. These damage laws are model-specific and they are a function of several parameters that have to be adjusted to calibrate the numerical model with experimental results, usually by trial and error. In contrast, the fatigue damage model formulated here is based on a Fracture Mechanics crack growth rate characterization which is achieved by linking Fracture Mechanics and Damage Mechanics: the evolution of the damage variable, d, is related with the crack growth rate, $\frac{dA}{dN}$ as follows:

$$\frac{\partial \mathsf{d}}{\partial N} = \frac{\partial \mathsf{d}}{\partial A_{\mathsf{d}}} \frac{\partial A_{\mathsf{d}}}{\partial N} \tag{6.7}$$

where A_{d} is the damaged area, and $\frac{\partial A_{\mathsf{d}}}{\partial N}$ is the growth rate of the damaged area. The term $\frac{\partial A_{\mathsf{d}}}{\partial N}$ is a material property that must be characterized experimentally for different loading conditions. The term $\frac{\partial \mathsf{d}}{\partial A_{\mathsf{d}}}$ can be obtained from Equation (6.5):

$$\frac{\partial \mathsf{d}}{\partial A_{\mathsf{d}}} = \frac{1}{A^e} \frac{[\Delta^f(1-\mathsf{d}) + \mathsf{d}\Delta^o]^2}{\Delta^f \Delta^o} \tag{6.8}$$

6.3.1 Determination of the growth rate of the damaged area as a function of the number of cycles

In a degradation process involving cyclic loading, the damaged area grows as the number of cycles increase: after ΔN cycles, the damaged area ahead of the crack tip increases by ΔA_{d} as schematically represented in Figure 6.3. It can be assumed that the increase in the crack area ΔA is equivalent to the increase in the amount of damaged area.

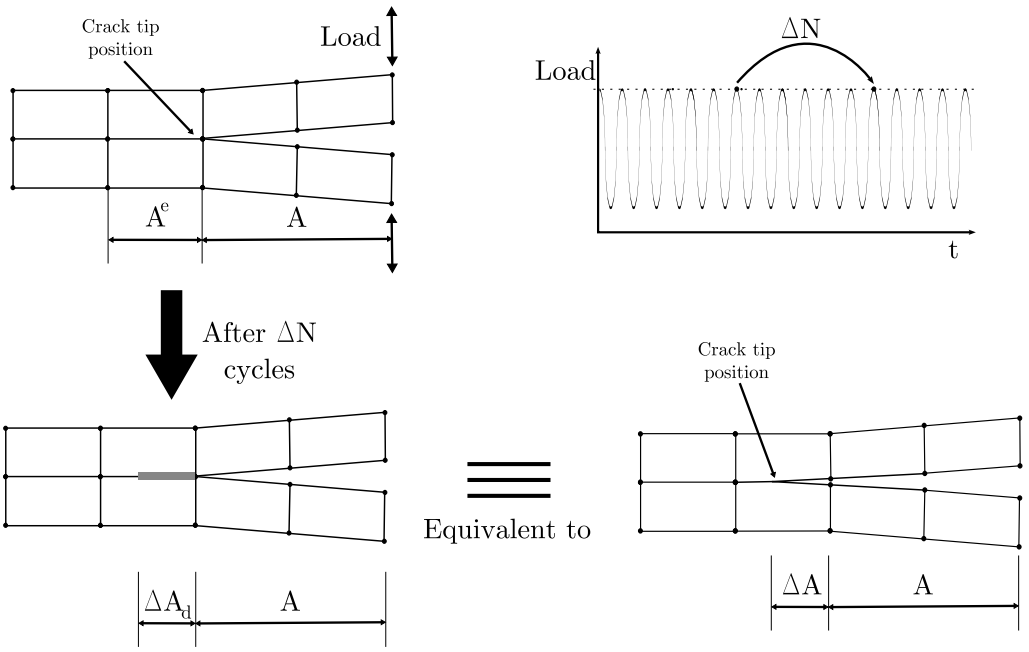

Figure 6.3: *Schematic representation of the equivalence between the increase in the damaged area and the crack growth.*

The increase in the damaged area along a crack front is equal to the increase in the damaged area of all of the elements ahead of the crack tip. Therefore, the crack growth rate can be assumed to be equal to the sum of the damaged area growth rates of all damaged elements ahead of the crack tip, that is, all elements in the cohesive zone:

$$\frac{\partial A}{\partial N} = \sum_{e \in A_{\mathrm{CZ}}} \frac{\partial A_{\mathsf{d}}^{e}}{\partial N} \tag{6.9}$$

where A_{d}^{e} is the damaged area of one element and the term A_{CZ} is the area of the cohesive zone. Assuming that $\frac{\partial A_{\mathsf{d}}}{\partial N}$ is the mean value of the damaged area growth rate $\frac{\partial A_{\mathsf{d}}^{e}}{\partial N}$ of the elements over the cohesive zone and assuming that the mean area of the elements in the cohesive zone is A^{e}, the previous equation can be written as:

$$\frac{\partial A}{\partial N} = \sum_{e \in A_{\mathrm{CZ}}} \frac{\partial A_{\mathsf{d}}^{e}}{\partial N} = \frac{A_{\mathrm{CZ}}}{A^{e}} \frac{\partial A_{\mathsf{d}}}{\partial N} \tag{6.10}$$

where the ratio $\frac{A_{\mathrm{CZ}}}{A^e}$ represents the number of elements in which the cohesive zone has been divided. In the context of finite elements, this ratio represents the number of elements that span the cohesive zone. Rearranging terms in Equation (6.10), the surface damage growth rate can be written as:

$$\frac{\partial A_{\mathsf{d}}}{\partial N} = \frac{A^{e}}{A_{\mathrm{CZ}}} \frac{\partial A}{\partial N} \tag{6.11}$$

6.3.2 Evolution of the damage variable under cyclic loading

By introducing Equations (6.8) and (6.11) into Equation (6.7) the evolution of the damage variable as a function of the number of cycles can be written as:

$$\frac{\partial \mathsf{d}}{\partial N} = \frac{1}{A_{\mathrm{CZ}}} \frac{(\Delta^{f}(1-\mathsf{d}) + \mathsf{d}\Delta^{o})^{2}}{\Delta^{f}\Delta^{o}} \frac{\partial A}{\partial N} \tag{6.12}$$

The area of the cohesive zone for pure Mode I can be estimated using Rice's closed-form equation [105, 165]:

$$A_{\mathrm{CZ}} = b \frac{9\pi}{32} \frac{E_3 G^{\max}}{(\tau^{o})^{2}} \tag{6.13}$$

where b is the width of the delamination front, and $G^{\max}$ is taken as the maximum energy release rate in the loading cycle. E_3 is the Young's modulus of the bulk material in the direction perpendicular to the crack plane, and τ^o is the interfacial strength.

6.3.3 Crack growth rate

The crack growth rate under fatigue loading, $\frac{\partial A}{\partial N}$, is a load and material-dependent characteristic that has been widely studied. The growth rate defined by the Paris

Law given in Equation (5.4) represents crack propagation in region II of the typical pattern of the crack growth rate (see Figure 5.1).

In region I, crack growth is not observed if the maximum energy release rate is smaller than the fatigue threshold of the energy release rate, G_{th}.

In region III, the crack growth rate increases because the maximum energy release rate approaches the fracture toughness. Tearing fracture controls the crack growth rate in region III instead of fatigue propagation.

The crack growth rate $\frac{\partial A}{\partial N}$ used in the present fatigue damage model, Equation (6.12), is defined as a piecewise function defined as:

$$\frac{dA}{dN} = \begin{cases} C\left(\frac{\Delta G}{G_c}\right)^m & , \quad G_{th} < G^{\max} < G_c \\ 0 & , \quad otherwise \end{cases} \tag{6.14}$$

where C, m and G_c are material constants that depend on the mode-ratio. The maximum energy release rate $G^{\max}$ and cyclic variation in the energy release rate ΔG used in the Paris Law rate equation can be computed using the constitutive law of the cohesive zone model (see Figure 6.4):

$$G = \int_0^{\Delta} \tau(\Delta) d\Delta \tag{6.15}$$

$$\Delta G = G^{\max} - G^{\min} \tag{6.16}$$

The maximum energy release rate is:

$$G^{\max} = \frac{\tau^o}{2}\left[\Delta^o + \frac{(\Delta^f - \lambda^{\max})^2}{\Delta^f - \Delta^o}\right] \tag{6.17}$$

By defining the load ratio, R as:

$$R^2 = \frac{G^{\min}}{G^{\max}} \tag{6.18}$$

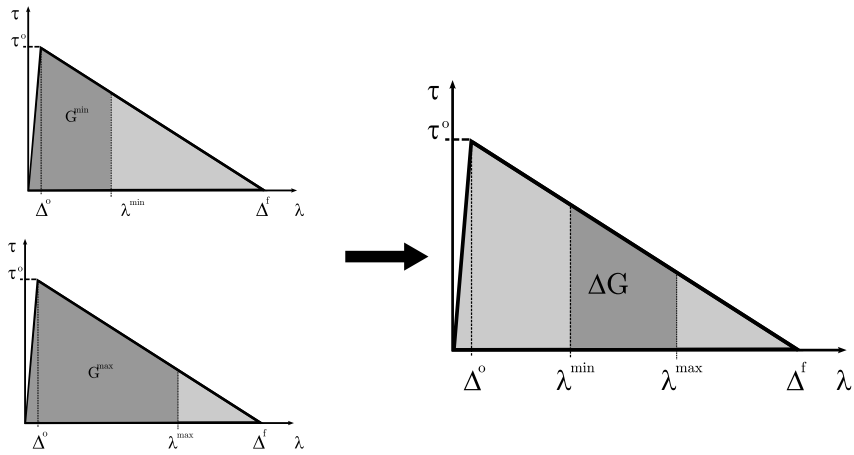

Figure 6.4: *Variation of the energy release rate.*

the variation of the energy release rate in Equation (6.16) can be re-written as:

$$\Delta G = \frac{\tau^o}{2}\left[\Delta^o + \frac{(\Delta^f - \lambda^{\max})^2}{\Delta^f - \Delta^o}\right](1 - R^2) \tag{6.19}$$

It is clear from Equation (6.19) that the model accounts for variations in the load ratio. The higher the load ratio, the smaller the variation in the energy release, as shown in Figure 6.5.

Mixed-mode loading

The material parameters, C, m, G_{th} used in the crack growth rate expression (6.14) depend on the mode ratio. In Mode I, the crack growth rate parameters are C_{I}, m_{I}, and $G_{\mathrm{I}th}$, and in Mode II, the crack growth rate parameters are C_{II}, m_{II}, and $G_{\mathrm{II}th}$. Under mixed-mode, the crack growth rate parameters C, m, and G_{th} must be determined. In this work, the dependence of the parameters C and m on the mode ratio is assumed to be of the form[163]:

$$\log C = \log C_{\mathrm{I}} + \left(\frac{G_{\mathrm{II}}}{G_T}\right)\log C_{\mathrm{m}} + \left(\frac{G_{\mathrm{II}}}{G_T}\right)^2 \log\frac{C_{\mathrm{II}}}{C_m C_{\mathrm{I}}} \tag{6.20}$$

and

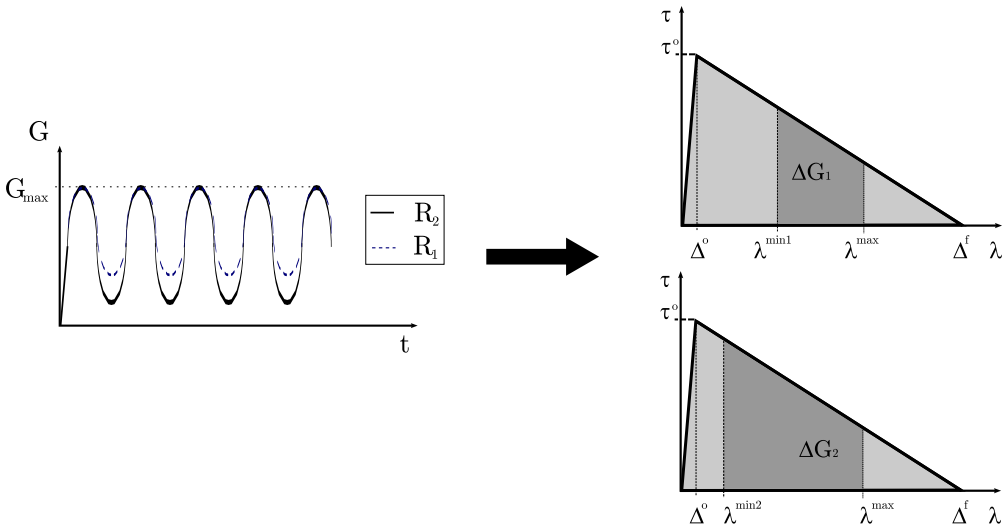

Figure 6.5: *The load ratio effect is captured by the constitutive equations. The higher load ratios ($R_1 > R_2$) the smaller ΔG ($\Delta G_2 > \Delta G_1$).*

$$m = m_{\mathrm{I}} + m_{\mathrm{m}} \left(\frac{G_{\mathrm{II}}}{G_T} \right) + (m_{\mathrm{II}} - m_{\mathrm{I}} - m_{\mathrm{m}}) \left(\frac{G_{\mathrm{II}}}{G_T} \right)^2 \tag{6.21}$$

where C_{m} and m_{m} are mode-ratio material parameters that must be determined by curve-fitting experimental data.

The dependence of the energy release rate threshold is assumed to follow an expression similar to that introduced by Benzeggagh and Kenane [29] for the dependence of the Fracture Toughness with the mode-ratio:

$$G_{th} = G_{\mathrm{I}th} + (G_{\mathrm{II}th} - G_{\mathrm{I}th}) \left(\frac{G_{shear}}{G_T} \right)^{\eta_2} \tag{6.22}$$

where η_2 is a material parameter obtained from a curve-fit of experimental results.

6.3.4 Cycle jump strategy

In a degradation process involving high-cycle fatigue, a cycle-by-cycle analysis becomes computationally intractable. Therefore, a cycle jump strategy is implemented

in the finite element model. A cycle jump means that the computation is done for a certain set of loading cycles at chosen intervals, and that the effect on the stiffness degradation of these loading cycles is extrapolated over the corresponding intervals in an appropriate manner. The cycle jump strategy adopted here is based on the one presented in [137]. After a certain number of cycles N_i, the damage variable d_i^J at an integration point J is computed using the quasi-static constitutive equations. The predicted evolution of the damage variable with the number of cycles, $\frac{\partial \mathsf{d}}{\partial N}$, is computed using Equation (6.12). The damage variable at an integration point J after ΔN_i cycles is:

$$\mathsf{d}_{i+\Delta N_i}^J = \mathsf{d}_i^J + \frac{\partial \mathsf{d}_i^J}{\partial N} \Delta N_i \tag{6.23}$$

To determine the number of cycles ΔN_i that can be skipped with a controlled level of accuracy, the following equation is used:

$$\Delta N_i = \frac{\Delta \mathsf{d}_{\max}}{\max\limits_J \left\{ \frac{\partial \mathsf{d}_i^J}{\partial N} \right\}} \tag{6.24}$$

where $\Delta \mathsf{d}_{\max}$ is a pre-established value. The smaller the choice of $\Delta \mathsf{d}_{\max}$ the higher the accuracy of the analysis.

6.4 Results and discussion

Several single-element numerical simulations were performed to verify the response of the fatigue damage model. Simulations of mode I, mode II and mixed–mode delamination tests were conducted to demonstrate that when the constitutive damage model is used in a structural analysis, the analysis can reproduce the response of the test specimens without the use of any model-specific adjustment parameters.

6.4.1 One element tests

The finite element model shown in Figure 6.6 is composed of two 4-node plane strain elements connected by a 4-node cohesive element representing the interface.

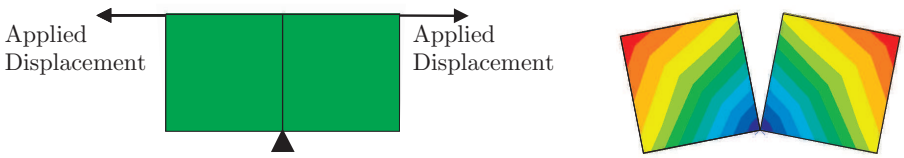

Figure 6.6: *Undeformed mesh with the boundary conditions and deformed mesh of one cohesive element tests.*

The material properties shown in Table 6.1 correspond to a T300/977-2 carbon-fiber reinforced epoxy laminate. The Paris Law coefficients used in the simulation were $C_{\mathrm{I}} = 0.0616$ mm^2/cycle and $m_{\mathrm{I}} = 5.4$. The threshold for fatigue crack propagation was assumed to be zero.

Table 6.1: *Properties used in the models with only one cohesive element.*

E_{11}	$E_{22} = E_{33}$	$G_{12} = G_{13}$	G_{23}	$\nu_{12} = \nu_{13}$	ν_{23}
150.0 GPa	11.0 GPa	6.0 GPa	3.7 GPa	0.25	0.45
G_{Ic}	G_{IIc}	τ_3^o	$\tau_2^o = \tau_1^o$	K	
0.268kJ/m^2	0.632 kJ/m^2	45 MPa	45 MPa	10^6N/mm^3	

The load was applied in two steps. The first step was a quasi-static step where the displacement jump is incremented to 20 times the onset displacement. The second step accounts for fatigue damage resulting from a maximum applied displacement of 20 times the onset displacement and a load ratio $R = 0$.

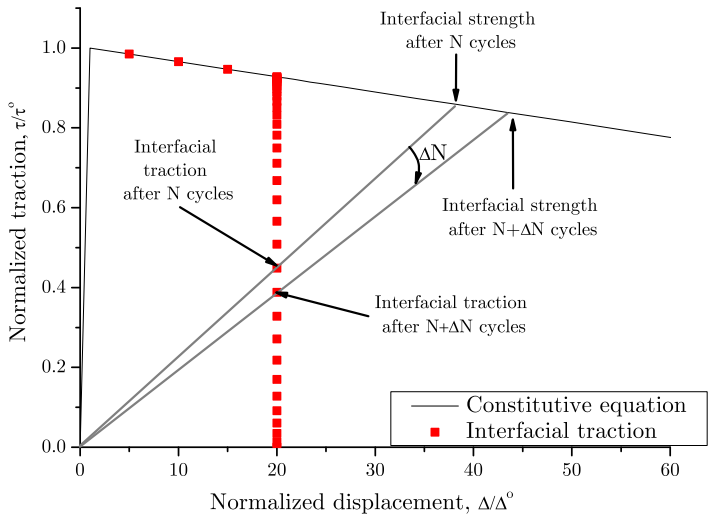

Figure 6.7: *Evolution of the interface traction in the constitutive equation for a displacement jump controlled high-cycle fatigue test.*

The evolution of the interface traction in the constitutive equation for a high-cycle fatigue test under displacement control is shown in Figure 6.7. It can be observed that fatigue damage causes a reduction of the stiffness, the interfacial traction, and the interfacial strength. The evolution of the interface traction and strength with the number of cycles is shown in Figure 6.8. The shape of the obtained curves is similar to the widely-used S-N curves used in the design for fatigue strength.

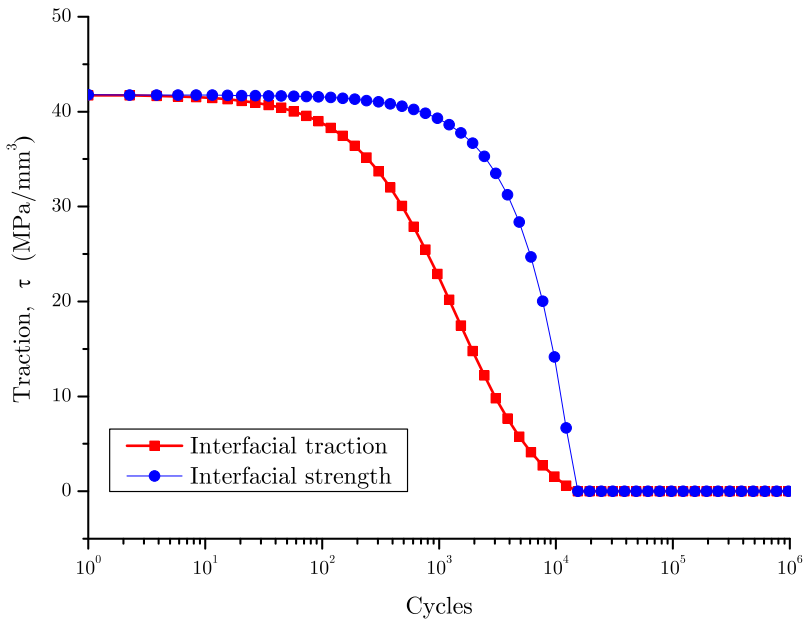

Figure 6.8: *Evolution of the interface traction and the maximum interface strength as a function of the number of cycles for a displacement jump controlled high-cycle fatigue test.*

6.4.2 Simulation of a DCB specimen under fatigue loading

Simulations of a double-cantilever beam (DCB) specimen were conducted to simulate the crack growth rate under Mode I loading for different ranges of the energy release rates. Experimental data on fatigue-driven delamination growth reported by Asp et al. [167] was selected for the validation of the numerical model. The specimen was fabricated with HTA/6376C carbon/epoxy prepreg produced by Hexcel. The layup consisted of $[0_{12}//(\pm 5/0_4)_S]$, where the sign // refers to the plane of the artificial delamination. The specimen was 150-mm-long, 20.0 mm-wide, with two 1.55-mm-thick arms, and an initial crack length of 35mm. A description of the experimental procedure is reported by Asp et al. [167]. The material properties are shown in Table 6.2 [140, 167, 168].

Table 6.2: *Material properties for HTA/6376C carbon/epoxy [140, 167, 168].*

E_{11}(GPa)	$E_{22} = E_{33}$(GPa)	$G_{12} = G_{13}$(GPa)	G_{23}(GPa)	$\nu_{12} = \nu_{13}$	ν_{23}
120	10.5	5.25	3.48	0.30	0.51
G_{Ic}(kJ/m^2)	G_{IIc}(kJ/m^2)	$\tau_2^0 = \tau_1^0$(MPa)	τ_3^0(MPa)		
0.260	1.002	30	30		

In the finite element model, the specimen's arms are loaded with opposing moments (Figure 6.9) to obtain a Mode I energy release rate that is independent independent of crack length and, consequently, to achieve a constant fatigue crack growth rate. The energy release rate is related to the applied moment as [140]:

$$G_{\mathrm{I}} = \frac{M^2}{bEI} \tag{6.25}$$

where b is the specimen width, E is the longitudinal flexural Young's modulus and I is the second moment of area of the specimen's arm.

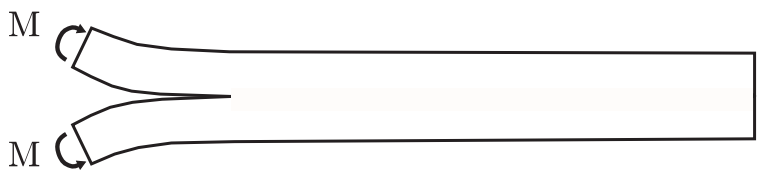

Figure 6.9: *Loading pattern for Mode I specimen.*

The finite element model is composed of 4-node plane strain elements for the arms, which are connected by 4-node cohesive elements representing the interface. Two elements are used through the thickness, h, of each arm. The length of the element is 0.05mm (see Figure 6.10). The Paris Law parameters of Equation

(5.4) were obtained from a linear regression of the experimental data [167]: $C_{\mathrm{I}} = 0.0616$ mm^2/cycle and $m_{\mathrm{I}} = 5.4$. The energy release rate threshold is 0.060 kJ/m^2 [167]. The material properties are shown in Table 6.3.

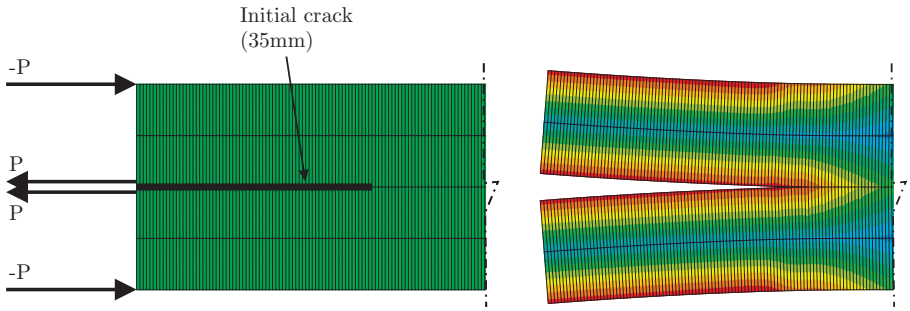

Figure 6.10: *Detail of the FEM model of the DCB specimen. Two applied load P with opposite direction were applied to each arm. The applied moment is equal to the product between the applied load P and the thickness of the arm.*

The load is applied in two steps: the first analysis loading step is quasi-static and it ends at the maximum applied load. It is assumed that no fatigue damage accumulation occurs during this step. Next, a second loading step is applied in which the maximum load is held constant. During this cycle, the analysis pseudo-time increment is assumed to be proportional to the number of loading cycles so that the fatigue damage model accounts for the accumulation of cyclic damage. The maximum variation in the damage variable $\Delta \mathsf{d}_{\max}$ allowed in a cycle jump is set to 0.001.

The results obtained from the simulations and the experimental data are shown in Figure 6.11. It can be observed that the constitutive model accounts for all three regions of fatigue crack growth. In region II, where crack growth rates follow the Paris Law, it is observed that a good agreement between the predictions and the experimental data is obtained. In region I there is negligible crack growth rate for small values of the normalized energy release rate and the numerical data follows the trend of the experimental data. A significant difference between the numerical and

Table 6.3: *Fatigue material properties for HTA/6376C carbon/epoxy obtained from references [140, 168] and using Equations (6.20) to (6.22).*

C_{I} (mm/cycle)	C_{II} (mm/cycle)	$C_{50\%}$ (mm/cycle)	m_{m} (mm/cycle)
0.0616	2.99	4.23	458087
m_{I}	m_{II}	$m_{50\%}$	C_{m}
5.4	4.5	6.41	4.94
G_{Ith} (kJ/m^2)	G_{IIth} (kJ/m^2)	$G_{50\%\mathrm{th}}$ (kJ/m^2)	η
0.060	0.100	0.066	2.73

the experimental data is observed in region III. One of the reasons for this difference is that the crack growth rates present in region III are very high and, therefore, a low-cycle instead of a high-cycle fatigue model is more appropriate for this region. However, in spite of this difference, the model can also predict Region III low cycle crack growth rate, where the Paris Law equation is not valid.

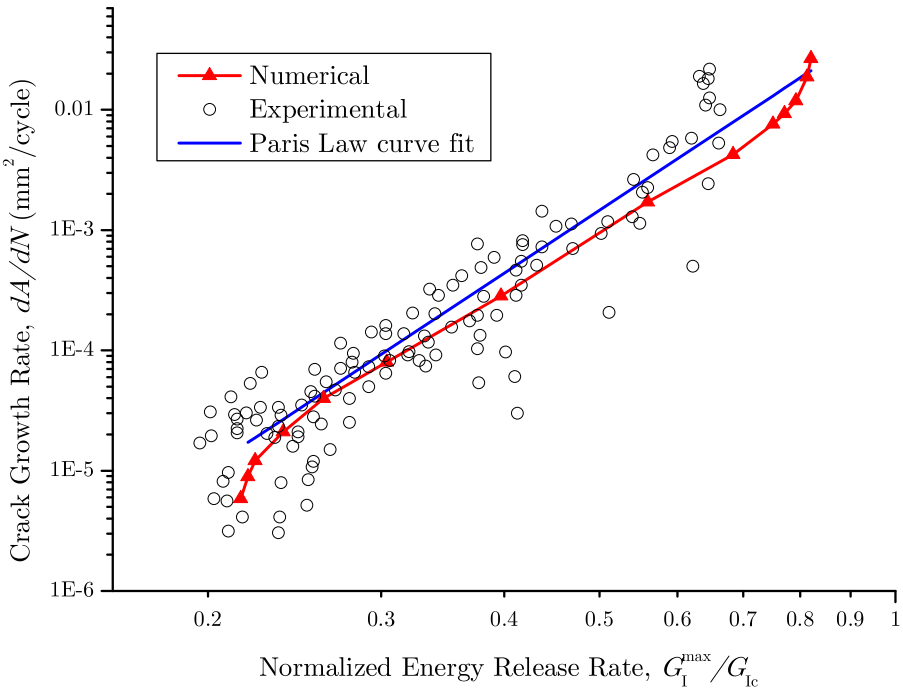

Figure 6.11: *Comparison of the experimental data with the crack growth rate obtained from the numerical simulation for a Mode I DCB test.*

Sensitivity of the rack propagation rates to the load ratio

Several DCB tests were conducted to verify the sensitivity of the model to the load ratio. The results obtained from the simulations are shown in Figure 6.12 where it can be observed that higher load ratios decrease the crack growth rate.

The sensitivity of the constitutive model to the load ratio is an asset of the model. The sensitivity of the propagation rate to the load ratio derives directly from the quasi-static model rather than from a fatigue model defined as a function of the load ratio, as has been done in previous investigations [141].

It can be observed from Figure 6.12 that the same energy release rate threshold G_{th} is predicted for all load ratios. This result is a consequence of the current formulation of the model: the influence of the load ratio on the energy release rate threshold is not taken into account. If G_{th} is constant, then the energy release rate

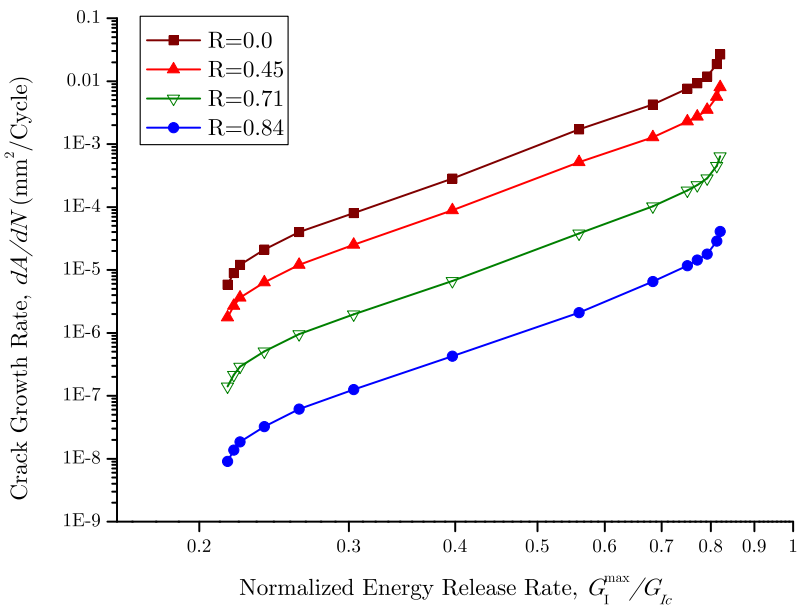

Figure 6.12: *Sensitivity of the model to the load ratio for a Mode I DCB test.*

range threshold ΔG_{th} must vary with the load ratio, which is a trend not reflected in experimental results. To verify this dependence, the predicted crack growth rates are represented in Figure 6.13 as a function of the energy release rate range ΔG instead of the $G^{\max}$. It can be observed that the predicted crack growth rates for the Region II of the crack growth rate are almost independent of the load ratio, which is in agreement with experimental results [145]. However, it can also be observed that different energy release rate range thresholds are predicted for different load ratios. This effect is a limitation of the present model that will be addressed in future work by the use of the range of the energy release rate range threshold in Equation (6.14).

6.4.3 Simulation of a 4ENF test

Several simulations were conducted to calculate the crack growth rate under Mode II loading for different ranges of the energy release rate. Experimental data on fatigue driven delamination growth reported in [167] was selected for comparison.

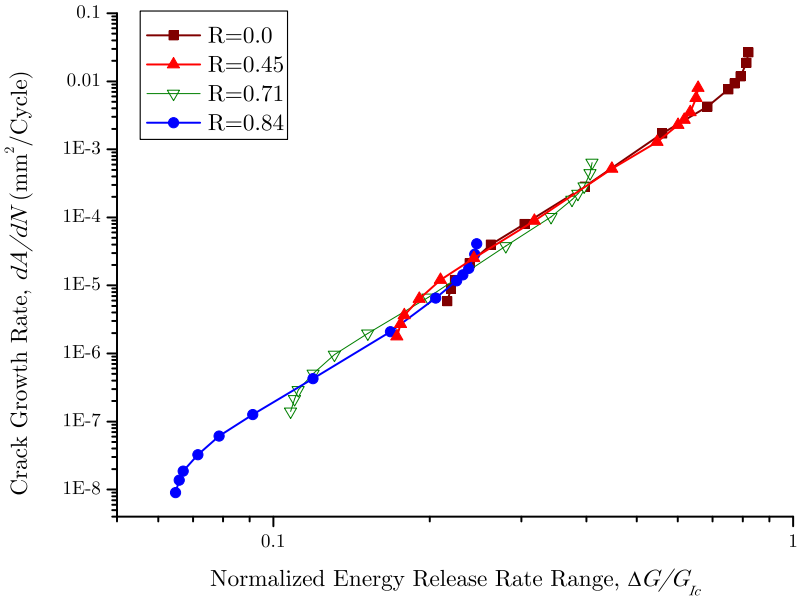

Figure 6.13: *Sensitivity of the model to the load ratio for a Mode I DCB test.*

The dimensions and the material of the specimen are the same used for the DCB specimen described in the previous section.

For pure Mode II, the specimen was loaded using the four point End Notched Flexure (4ENF) test shown in Figure 6.14. The energy release rate is related to the applied moment, $\frac{cP}{2}$, as [140]:

$$G_{\mathrm{II}} = \frac{3}{4}\frac{(\frac{cP}{2})^2}{bEI} \tag{6.26}$$

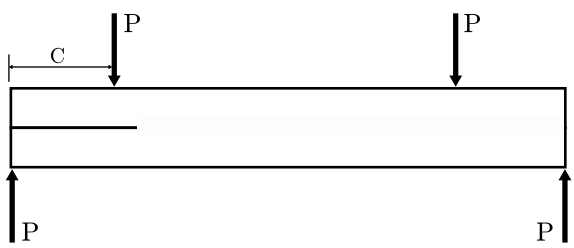

Figure 6.14: *Loading pattern for Mode II 4ENF specimen.*

The finite element model used was similar to that used in the simulation of the Mode I test (see Figure 6.15). The Paris Law coefficients of Equation (5.4) were obtained from a linear regression of the experimental data presented in Ref. [167]: $C_{\mathrm{II}} = 2.99$ mm^2/cycle and $m_{\mathrm{II}} = 4.5$. The energy release rate threshold is 0.100 kJ/m^2 [167]. The fatigue properties are summarized in Table 6.3.

The load is applied in two steps, as described in the previous section.

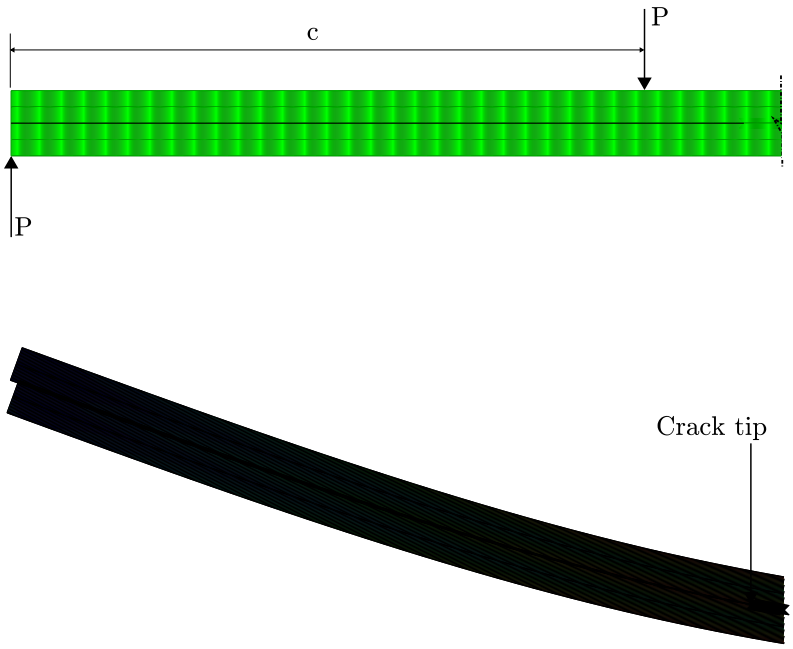

Figure 6.15: *Detail of the FEM model of the 4ENF specimen.*

The results obtained from the simulations and the experimental data [167] are shown in Figure 6.16. The predicted crack growth rates for small values of $\frac{G_{\mathrm{II}}^{\max}}{G_{\mathrm{IIc}}}$ are slightly higher compared to the experimental data. This difference can be attributed to friction effects that are not considered in the current implementation. Moreover, it should be mentioned that the model estimates the size of the cohesive zone using Equation (6.13), which may be accurate for Mode I [165] but not necessarily for Mode II. Further investigations on the estimation of the cohesive zone length under

Mode II should be conducted.

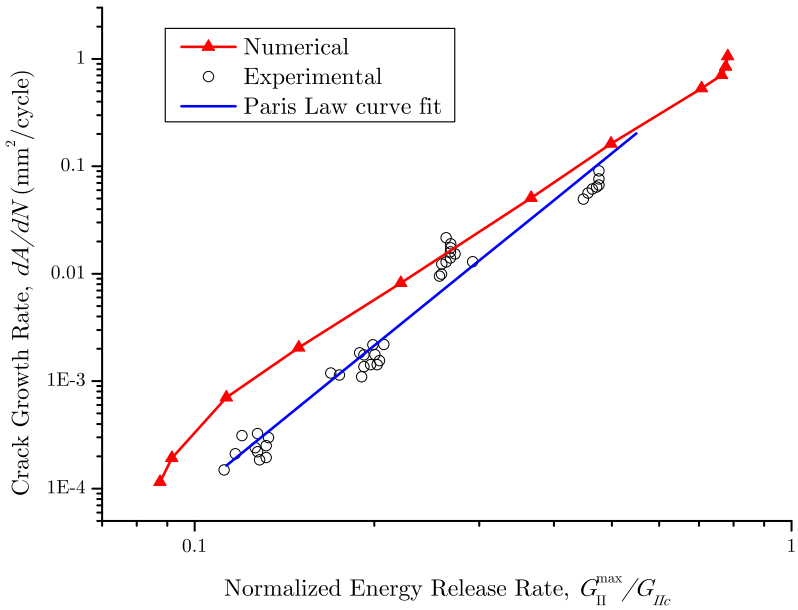

Figure 6.16: *Comparison of the experimental data with the crack growth rate obtained from the numerical simulation for a Mode II 4ENF test.*

6.4.4 Simulation of mixed-mode loading

Several simulations were conducted to calculate the crack growth rate under mixed-mode loading with $G_{\mathrm{I}} = G_{\mathrm{II}}$ for different energy release rates. Experimental data on fatigue driven delamination growth reported in [167] was selected for comparison. The dimensions and the material of the specimen are the same used for the DCB specimen described above.

For mixed-mode loading, the specimen was loaded with two moments as it is shown in Figure 6.17. The ratio between the two applied moments, ρ, for a mode-ratio of 50% is:

$$\rho = \frac{1 - \frac{\sqrt{3}}{2}}{1 + \frac{\sqrt{3}}{2}} \tag{6.27}$$

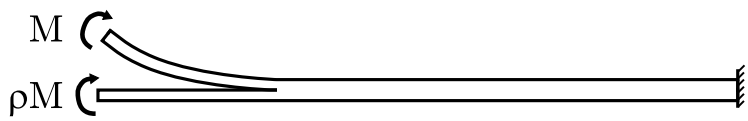

Figure 6.17: *Loading pattern for mixed-mode specimen.*

The energy release rate is related to the applied moment, M, as [140]:

$$G_{\mathrm{I}} = G_{\mathrm{II}} = \frac{3}{4\left(1 + \frac{\sqrt{3}}{2}\right)^2} \frac{M^2}{bEI} \tag{6.28}$$

The finite element model used was similar to that used in the simulation of the Mode I test (see Figure 6.18).

The mixed-mode parameters C_{m}, m_{m}, and G_{th} are computed at each integration point using Equations (6.20), (6.21) and (6.22) to account for any changes in the mode-ratio. The fatigue material properties used in the simulation are summarized in Table 6.3. The load is applied in two loading steps, as described in previous sections.

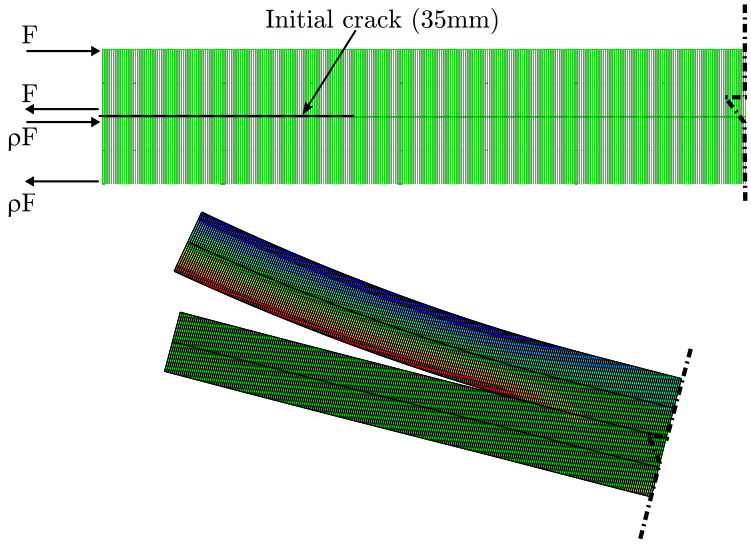

Figure 6.18: *Detail of the FEM model of the specimen mixed-mode loaded.*

The results obtained from the simulations and the experimental data [167] are shown in Figure 6.19. As in the case of pure Mode II, the predicted data for small values of $\frac{G^{\max}}{G_c}$ are slightly higher than the experimental data.

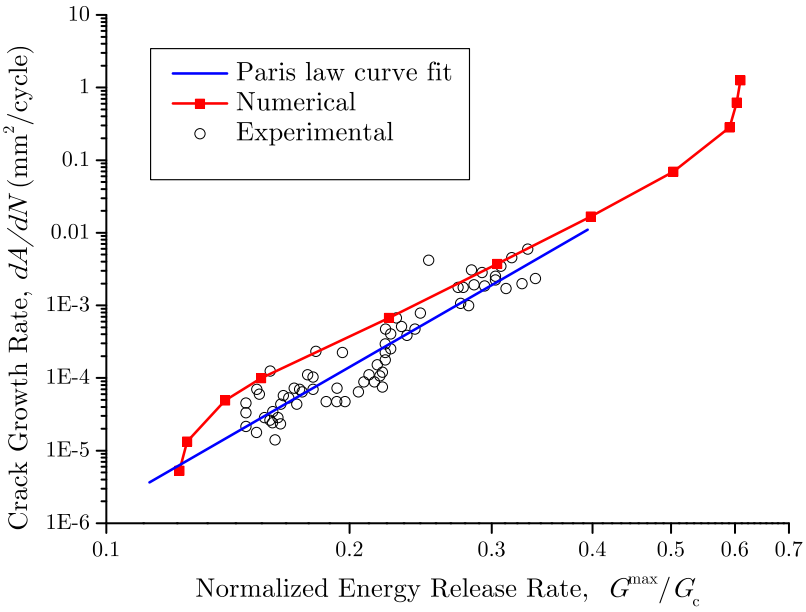

Figure 6.19: *Comparison of the experimental data with the crack growth rate obtained from the numerical simulation for a mixed-mode test with* $G_I = G_{II}$.

6.5 Conclusions

A damage model suitable for both quasi-static and high-cycle fatigue delamination propagation was developed. The evolution of the damage variable was derived by linking Damage Mechanics and Fracture Mechanics, thus establishing a relation between damage evolution and crack growth rates. The damage evolution laws for cyclic fatigue were combined with the law of damage evolution for quasi-static loads within a cohesive element previously developed by the authors.

The model was validated using single-element numerical tests, as well as by simulating the propagation rates of Mode I, Mode II and mixed-mode tests. The model was able to reproduce the Paris Law growth rate without the need of any additional adjustment parameters. Moreover, the model accounts for the energy release rate thresholds preventing crack growth for smaller values of the energy release rate. Unlike other approaches proposed in the literature, where the dependence on the load ratio, R, is introduced through the definition of R-dependent Paris Law parameters, the effects of the load ratio on the analysis results are inherent to the formulation.

The analysis of the results indicate that the model is more accurate when Mode I loading predominates. This effect can be justified by two factors: i) friction between the crack faces is not taken into account in the model, and ii) the model relies on an equation to estimate the length of the cohesive zone that was developed for for Mode I loading. Further investigations on the estimation of the cohesive zone length under Mode II and mixed-mode should be conducted.

In summary, the model is able to predict the crack growth rates in all regimes of propagation and the results compare favorably with the experimental data, including the negligible crack growth rates for small values of the normalized energy release rate and the sensitivity to the mode and load ratio.

Part III

Closure

Chapter 7

Conclusions and suggestions for Future Work

7.1 Conclusions

A design tool for the analysis of delamination in laminated composites was developed. The design tool is developed using the damage-tolerance concept to predict both delamination initiation and growth. Therefore, the model developed can be used to perform either strength and damage-tolerance verification of new components, and can be used to assess the necessity to repair or replace in-service components. The model developed can be used either to simulate quasi-static and fatigue loading.

7.1.1 Cohesive zone model for the simulation of delamination under quasi-static loads

A thermodynamically consistent damage model for the simulation of progressive delamination based on Damage Mechanics was presented. A constitutive equation for the interface was derived from the free energy of the interface. The resulting damage model simulates delamination onset and delamination propagation. The

constitutive equation proposed uses a single scalar variable to track the damage at the interface under general loading conditions. A new initiation criterion that evolves from the Benzeggagh-Kenane propagation criterion has been developed to assure that the model accounts for changes in the loading mode in a thermodynamically consistent way and avoids restoration of the cohesive state.

The damage model was implemented in a finite element formulation. The material properties required to define the element constitutive equations are the interlaminar fracture toughnesses, the penalty stiffness, and the strengths of the interface. In addition, a material parameter η, which is determined from standard delamination tests, is required for the Benzeggagh-Kenane mode interaction law.

The simulations of the DCB, ENF, and MMB tests, and the simulation of a composite skin-stiffener co-cured sub-component show the accuracy of the model. The proposed formulation can predict the strength of composite structures that exhibit progressive delamination.

Moreover, an engineering solution for the simulation of delamination using coarse meshes was developed. Two new guidelines for the selection of the parameters for the constitutive equation used for the simulation of delamination were presented.

Firstly, a new equation for the selection of the interface stiffness parameter K was derived. The new equation is preferable to previous guidelines because it results from mechanical considerations rather than from experience. The approach provides an adequate stiffness to ensure a sufficiently stiff connection between two neighboring layers, while avoiding the possibility of spurious oscillations in the solution caused by overly stiff connections.

Secondly, an expression to adjust the maximum interfacial strength used in the computations with coarse meshes was presented. It was shown that a minimum number of elements within the cohesive zone is necessary for accurate simulations. By reducing the maximum interfacial strength, the cohesive zone length is enlarged and the cohesive zone spans more elements.

The methodology was used to simulate delamination in specimens with and

without initial crack. The results obtained by reducing the maximum interfacial strength show that accurate results can be obtained with a mesh ten times coarser than by using the nominal interface strength. Moreover, the results obtained show that the model can be used to predict both delamination initiation and delamination propagation.

7.1.2 Cohesive zone model for the simulation of delamination under high-cycle fatigue

The damage model developed to simulate static or quasi-static loads has been enhanced to simulate high cycle fatigue. The evolution of the damage variable was derived by linking Fracture Mechanics and Damage Mechanics, establishing a relation between damage evolution and crack growth rates. The damage evolution laws for cyclic fatigue were combined with the law of damage evolution for quasi-static loads.

The material properties required to define the element constitutive equations are those used to define the quasi-static model, the Paris Law parameters under mode I and mode II, the dependence of the Paris Law parameters with the mode-ratio, the energy release rate thresholds under mode I and mode II, and a material parameter η_2, which is used to describe the dependence to the energy release rate thresholds and to the mode-ratio.

The model is able to reproduce the typical crack growth pattern without the need of any additional adjustment parameters than those of the Paris Law parameters and the energy release rate threshold. The number of parameters to be adjusted is smaller than for other phenomenological models to simulate high cycle fatigue. The model is also sensitive to the load ratio and to the mode ratio.

7.2 Suggestions for Future Work

7.2.1 Quasi-static Model

The computational cost of cohesive models is not addressed in this thesis but is an important issue in the use of these models. To reduce the computational cost of the simulations using cohesive zone models it is necessary to investigate how to solve the convergence problems that appear in the simulations. A good approach can be using a convergence criteria based on energy measures instead of displacement or force measures.

The current implementation is done using cohesive elements, that is, zero-thickness elements that are placed at the interface between two solid continuum elements. The pre-processing of these types of elements cannot be done directly using the current pre-processors present in the market. It is important to aid the pre-processing of cohesive models and also to implement the model in other element technologies like elements with embedded interfaces. However, further research has to be done in the field of elements with embedded interfaces to be used with commercial finite element codes. To simulate large structures like aircraft engine blades, solid elements are not typically used because it is necessary to define very small elements to obtain correct aspect ratios. Thus, it can be useful to implement the model in cohesive elements connecting continuum shell elements instead of solid elements. Some attempts to do so are underway although some problems remain to be solved, such as the traction discontinuity of the shear stress profile through the thickness before delamination initiation.

7.2.2 Fatigue Model

There are several aspects to be investigated before the high-cycle fatigue model is used routinely in the design of structures.

There are some references in the literature that suggest the shape of the quasi-

static constitutive equation does not affect much the results under static or quasi-static loading. This is not necessary true under fatigue loading. In fact, the computation of the energy release rate range used in formulation strongly depends on the shape of the quasi-static loading. Therefore, an investigation of the effect of the shape of the constitutive model on the results is required.

The influence of the mesh size is not addressed for the high-cycle fatigue model. The meshes used in the simulation with the high-cycle fatigue model are very fine to accurately compute the energy release rate at each integration point. The use of coarser mesh can affect the results, as seen for the quasi-static model, especially for values near the threshold.

The results obtained with the model are more accurate for mode I than for mode II. As the mode II component increases, the accuracy of the results decreases. A possible explanation for this effect is the presence of friction effects. Further investigation to clarify the effect observed should be addressed.

The cycle-jump strategy used in the formulation is quite simple. There are in the literature more advanced cycle jump strategies that may be used to improve the accuracy of the model.

It has been shown that the proposed model is able to reproduce the crack growth rate in the Region III of the typical pattern of the crack growth rate. In Region III high crack growth rates are obtained, thus the size the size of the cycle jump is very small. Further investigation about the validity of the model in this Region should be addressed to decide if it is necessary to develop a low-cycle fatigue model that complements the current model.

7.2.3 Environmental Effects

Environmental effects like the presence of humidity or thermal effects, especially thermal fatigue, are not addressed in the current model. These aspects can be considered by defining the interface properties used in the model to be dependent

on environmental effects.

7.2.4 Stochastic Distributions

As it was shown throughout this dissertation, the interfacial material properties may significantly affect the structural response. In most cases, one cannot obtain the interfacial material properties since these data are limited and incomplete in the literature. Hence, the material properties are often assumed based on the strength limits of the bulk material. For this reason, it is suggested a stochastic analysis of the fracture process with the statistical variation of the interfacial strength, critical energy release rate.

Regarding the fatigue model, the cyclic load history has a stochastic behaviour. The sensitivity of the current model to load-sequence is inherent to the formulation presented. However, deeper analysis verifying the effect of stochastic cyclic load histories is suggested.

Part IV

Appendices

Appendix A

Cohesive element for progressive delamination using ABAQUS. User Manual.

A.1 Preface

This appendix is a reference manual for the utilization of a cohesive element implemented as an ABAQUS© user subroutine (UEL). The report contains a brief description of the formulation of the element, the input into ABAQUS/Standard and some examples to test the code.

A.2 Introduction

This report is a reference manual for the use of the cohesive element implemented using a user written subroutine in ABAQUS. The subroutine implemented contains a cohesive element for the simulation of delamination onset and growth under generalized loading conditions.

The cohesive element can be formed by 2^n nodes. The cohesive element formed by 4 nodes ($n = 2$) can be used to connect continuum plane strain elements with two degrees of freedom per node. The cohesive element formed by 8 nodes ($n = 3$) can be used to connect three-dimensional continuum elements with three degrees of freedom per node.

The subroutine has been written by Albert Turon (University of Girona, Spain) directed and supervised by Dr. Pedro P. Camanho (University of Porto, Portugal), Dr. Josep Costa (University of Girona, Spain) and Dr. Carlos G. Dávila (NASA-Langley Research Center, US). The subroutine has been written based on previous versions by Dr. P.P. Camanho, C.G. Dávila, S.T. Pinho and M. Moura.

A.3 Formulation of the Element

A.3.1 Basic element theory

The constitutive equation of the cohesive element relate the tractions τ_i at the midsurface of the element to the displacement jumps Δ_m. The boundary value

problem, the kinematic equations, and the constitutive model for delamination onset and delamination propagation are presented in previous Chapters.

The basic requirement of the subroutine is to define the contribution of the cohesive element to the global model. The subroutine must define the contribution of the element to the tangent stiffness matrix and to the residual vector, i.e., the internal force vector of the cohesive element.

The internal force vector of the cohesive element is given by:

$$f_{Ki} = \int_{\Gamma_{d_i}} \tau_i B_{imK} d\Gamma_d \tag{A.1}$$

where B_{imK} is defined as:

$$B_{imK} = \Theta_{im} \bar{N}_K \tag{A.2}$$

The rotation tensor Θ_{im} relates the global and the local co-ordinates.

The softening nature of the cohesive element constitutive equation causes difficulties in obtaining a converged solution for the non-linear problem when using the Newton-Raphson iterative method. In particular, quadratic convergence is not assured because the residual vector is not continuously differentiable with respect to the nodal displacements.

The tangent stiffness matrix stems from the linearization of the internal force vector and it is obtained using Taylor's series expansion about the approximation q_{Ki}. Taking into account that the calculation of the geometric terms of the tangent stiffness matrix is computationally very intensive, these terms are neglected. The tangent stiffness matrix, K_{rZiK}, for the cohesive element is therefore approximated as:

$$K_{jKrZ} \approx \int_{\Gamma_d} B_{ijK} D_{in}^{\tan} B_{nrZ} d\Gamma_d \tag{A.3}$$

where $D_{in}^{\tan}$ is the material tangent stiffness matrix, or constitutive tangent tensor used to define the tangent stiffness matrix and depends on the interfacial constitutive model adopted.

A.3.2 Element definition

Geometry and node numbering

The cohesive element is an initially zero-thickness element that connects two continuum elements. The numbering sequence of the cohesive element is shown in figure A.1.

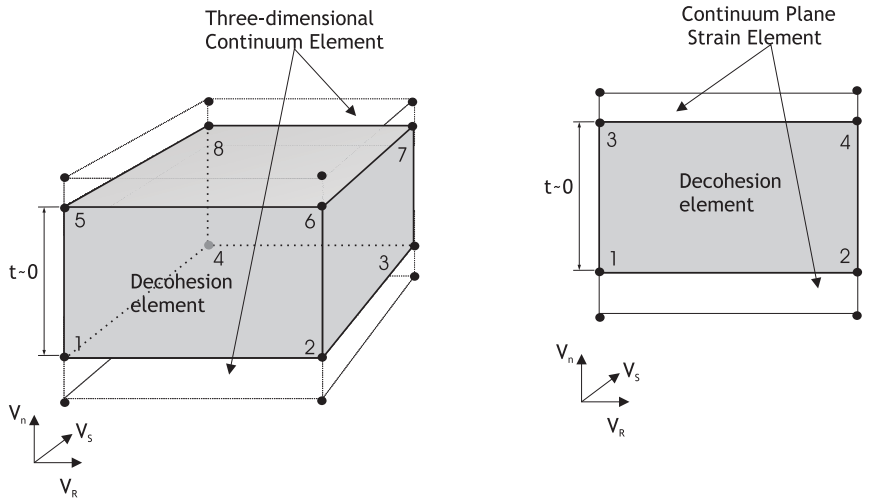

Figure A.1: Element node-numbering conventions

Nodal freedoms (displacement jumps)

At each node, all elements have n translational degrees of freedom. The order of the displacement components at the element node K, in the global coordinate system (123) is:

$$q_K = \{q_{Ki}\} \quad i = 1, n \tag{A.4}$$

The order of the displacement components for the 2^n-node cohesive elements is:

$$q = \{q_{11}, q_{12}, .., q_{2^n n-1}, q_{2^n n}\} \tag{A.5}$$

Intrinsic parameters

A summary of intrinsic parameters for each element is presented in Table 1.

Table 1. *Element Parameters*

Parameter	Description	Value
NNODE	No. of Element Nodes	2^n
NDIME	No. of Freedoms/Node	n
NEVAB	No. of Freedoms/Element	$n2^n$
NGAUS	No. of Gauss points for each direction	2
IPOINTS	No. of Integration points /Element	2^{n-1}

A.3.3 Implementation status

Nomenclature of the subroutine

The nomenclature of the subroutine is:

$$ut - vX - rZ.for$$

where X is the version number and Z is the release number. The code of the current implementation is presented in Appendix B

Material non-linearity

The constitutive behaviour of the cohesive element is modelled using a non-linear material model formulated in the context of Damage Mechanics. In the current formulation, a scalar constitutive damage model has been implemented. The constitutive equation is written as:

$$\tau = \left\{ \begin{array}{c} \tau_1 \\ \tau_2 \\ \tau_3 \end{array} \right\} = (1 - \mathsf{d})\, K \left\{ \begin{array}{c} \Delta_1 \\ \Delta_2 \\ \Delta_3 \end{array} \right\} - \mathsf{d} K \left\{ \begin{array}{c} 0 \\ 0 \\ \langle -\Delta_3 \rangle \end{array} \right\} \tag{A.6}$$

where K is a penalty parameter necessary to assure a stiff connection between two neighboring layers, $\langle \cdot \rangle$ is the McAuley bracket, and d is the damage variable of the model. The evolution of the damage variable depends on the constitutive equation adopted. In the current implementation a bilinear equation has been used.

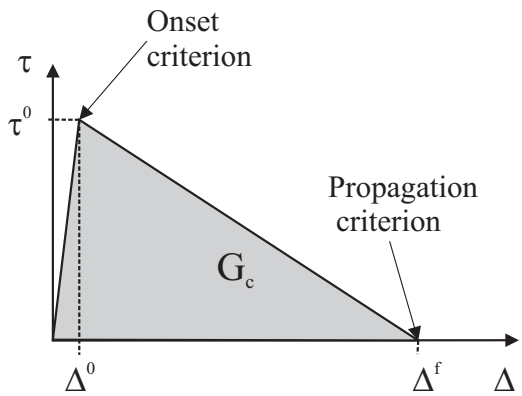

Figure A.2: *A bilinear constitutive equation for the cohesive element for a mixed-mode loading situation*

Geometrical nonlinearity

The effect of the geometrical nonlinearities is taken into account using a total Lagrangian formulation, where the position of the element midsurface is tracked throughout the analysis.

Implementation of the stiffness tensor

The implementation of the damage model as a finite element stiffness was performed using the tangent as well the secant constitutive tensors. The tangent stiffness poses convergence difficulties in the vicinity of a global instability, while the secant stiffness produces slow convergence of the solution procedure. The code initially uses the tangent stiffness tensor in the calculations. If after a certain number of iterations the convergence has not achieved, the code automatically reduces the time step. If convergence is not achieved after a certain number of iterations, then the code switches between the tangent stiffness tensor and the secant stiffness tensor.

The threshold number of iterations can be changed by an expert user changing the default value of the variable $ITMAX$ in the code. In the same way, the reduction factor in the time step can also be changed modifying the value of the *pnewdt*

variable.

A.4 Input into ABAQUS/Standard

The format of the parameters required by the subroutine to use the cohesive element with ABAQUS/Standard is discussed in this Section. The user must define the type of the element, the element properties, the number of nodes, the maximum number of coordinates needed at any nodal point, the element properties, and the number of solution-dependent variables that must be stored within the element. A summary of the command lines and parameters needed to be defined is presented in Table 2.

A.4.1 Element type

The user must first specify whether to invoke an initially open (broken) element or initially closed. This specification is accomplished in the *USER ELEMENT command line with the TYPE option set to either U1 for an initially open cohesive element or U2 for a broken cohesive element.

A.4.2 Number of nodes and coordinates per node

The number of nodes and the coordinates per node of the cohesive element are specified by the NODES and COORDINATES parameters on the *USER ELEMENT option. The number of nodes of the elements is 2^n, and the coordinates per node is n.

A.4.3 Element properties

Eight parameters define the properties of an element. These eight numerical values consist of seven real values and one integer value. The number of properties is defined on the *USER ELEMENT command line, using the PROPERTIES parameter to

define the number of real values (7) and the I PROPERTIES parameter to define the number of integer values (1).

The numerical values of the element properties are defined on the *UEL PROPERTY command line, entering the real values first, followed immediately by the integer values. The data required on the data line of the *UEL PROPERTY are:

1. G_{IC}, mode I fracture toughness of the material.

2. G_{IIC}, mode II fracture toughness of the material.

3. τ_3^o, normal interfacial strength.

4. τ_{shear}^o, shear interfacial strength.

5. K, the value of the penalty stiffness to assure a stiff connection between two neighboring layers.

6. η, the mixed-mode interaction parameter. The signum of η determines the mixed-mode criteria used:

   (a) $\eta > 0$ The expression proposed by [29] for the calculation of the critical energy release rate is used.

   (b) $\eta < 0$ The Power Law form for the failure criterion is used in the calculation.

7. $Thickness$, the thickness of the element for the 4-node cohesive element. For the 8-node cohesive element, this space can be left blank.

8. $NLGEOM$, This is a flag to activate geometrically nonlinear behavior of the element.

   (a) $NLGEOM = 0$, geometrically linear behavior.

   (b) $NLGEOM = 1$, geometrically nonlinear behavior.

A.4.4 Number of solution-dependent variables

The solution-dependent variables that must be stored at each integration point is the damage variable d of the constitutive damage model. Thus, the number of solution-dependent variables that must be stored within the element is equal to the number of integration points of the element, i.e., 2^{n-1}.

The number of solution dependent variables per element are specified by the VARIABLES parameter on the *USER ELEMENT option.

Table 2. *Command lines for the input into ABAQUS/Standard*

Command Line	Parameter
*USER ELEMENT	,TYPE=U1,NODES=2^n,UNSYMM,
	COORDINATES=n,I PROPERTIES=1,
	PROPERTIES=7,VARIABLES=2^{n-1}
	1..n
*ELEMENT	,TYPE=U1
*UEL PROPERTY	,ELSET=INTER
	G_{IC}, G_{IIC}, τ_3^o, τ_{shear}^o, K, η, $Thickness$, $NLGEOM$

A.5 Examples

Two different types of examples are provided to illustrate the behavior of the subroutine and check possible future improvements in the code. The first set of examples are models with only one cohesive element, joining two continuum elements. The second set of examples are simulations of Double Cantilever Beam test (DCB), End Notched Flexure test (ENF), and Mixed Mode Bending test (MMB). The input files of all of these models are given in the appendix.

A.5.1 One element simulations

The set of examples with only one cohesive elements is formed by three different models. The first model consists of an 8-node cohesive element that connects two three-dimensional continuum elements. The continuum solid elements are 1-mm-long, 1-mm-wide and 1-mm-thick. The second and the third models consist of a 4-node cohesive element that connects two continuum plane strain elements. The difference between these two models is the orientation in the space. The undeformed and deformed meshes for these three models are presented in Figure A.3. The material properties used in the simulations are summarized in Table 3.

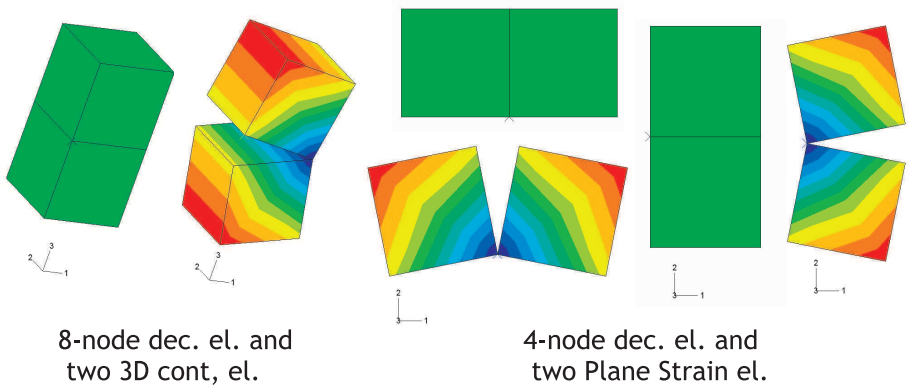

Figure A.3: Undeformed and deformed mesh of models with an 8-node cohesive element (left), and a 4-node cohesive element (center and right), connecting two continuum elements.

Table 3. *Properties used in the models with only one cohesive element*

E_{11}	$E_{22} = E_{33}$	$G_{12} = G_{13}$	G_{23}	$\nu_{12} = \nu_{13}$	ν_{23}
150.0 GPa	11.0 GPa	6.0 GPa	3.7 GPa	0.25	0.45
G_{IC}	G_{IIC}	τ_3^o	$\tau_2^o = \tau_1^o$	K	
0.268 kJ/m^2	0.632 kJ/m^2	45 MPa	45 MPa	$10^6 N/mm^3$	

These models with only one cohesive element are very useful to check the implementation, especially the constitutive model implemented: the force-displacement

relation obtained in the simulation can be directly related to the traction-displacement jump constitutive equation implemented in the formulation. For example, the maximum load expected in a mode I test should be around $\tau_3^o dA$, where dA is the area associated with each integration point, thus the maximum load for delamination onset expected in the simulations is around $45MPa$ x $0.50mm^2 = 22.5N$.

A load-unload test has been simulated, increasing the displacement until a certain value far away from the delamination onset point and then releasing the load until the start point of the simulation. The load-displacement curve obtained in the simulations is shown in Figure A.4. As expected, the maximum load is around $22.5N$, and when the load has been released, no permanent displacement jump is observed.

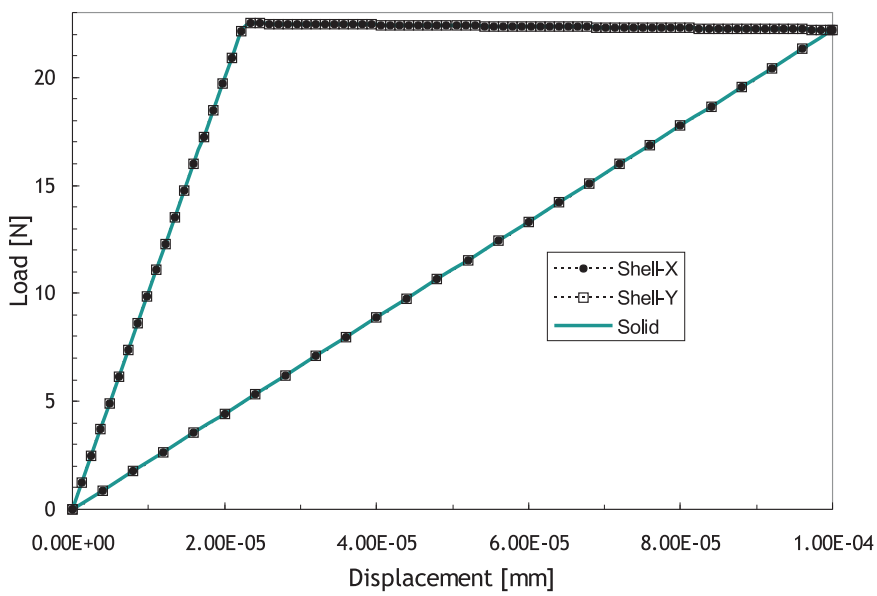

Figure A.4: Load-displacement curve for models with one cohesive element

A.5.2 Mode I, mode II and mixed-mode delamination growth for PEEK composites

Eight-node cohesive elements were used to simulate DCB, ENF and MMB tests in a unidirectional AS4/PEEK carbon-fiber reinforced composite. The specimens simulated were 102-mm-long, 25.4-mm-wide, with two 1.56-mm-thick arms. The material properties are shown in Table 4, and a penalty stiffness $K = 10^6 N/mm^3$ is used. The undeformed and deformed mesh for the MMB simulation are shown in Figure A.5. The load-displacement curves obtained in the simulations are shown in Figure A.6.

Table 4. *Properties for PEEK/AS4*

E_{11}	$E_{22} = E_{33}$	$G_{12} = G_{13}$	G_{23}	$\nu_{12} = \nu_{13}$
122.7 GPa	10.1 GPa	5.5 GPa	3.7 GPa	0.25
ν_{23}	G_{IC}	G_{IIC}	τ_3^o	$\tau_2^o = \tau_1^o$
0.45	0.969 kJ/m^2	1.719 kJ/m^2	80 N/mm^3	$100 N/mm^3$

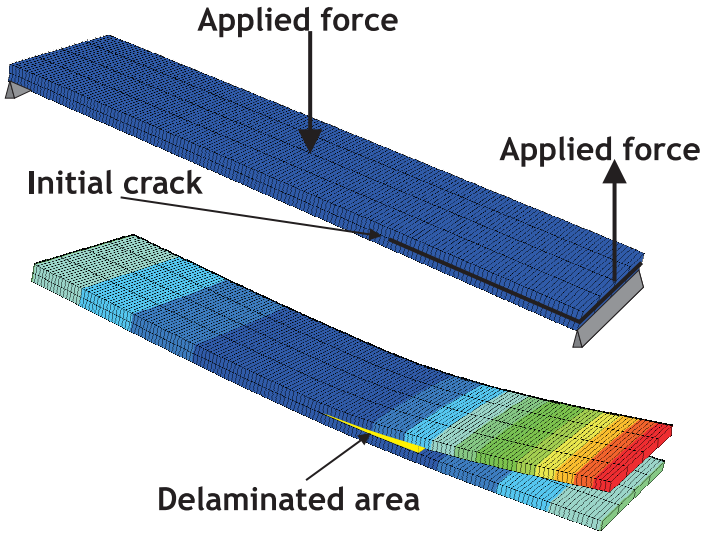

Figure A.5: Undeformed and deformed mesh for the MMB simulation

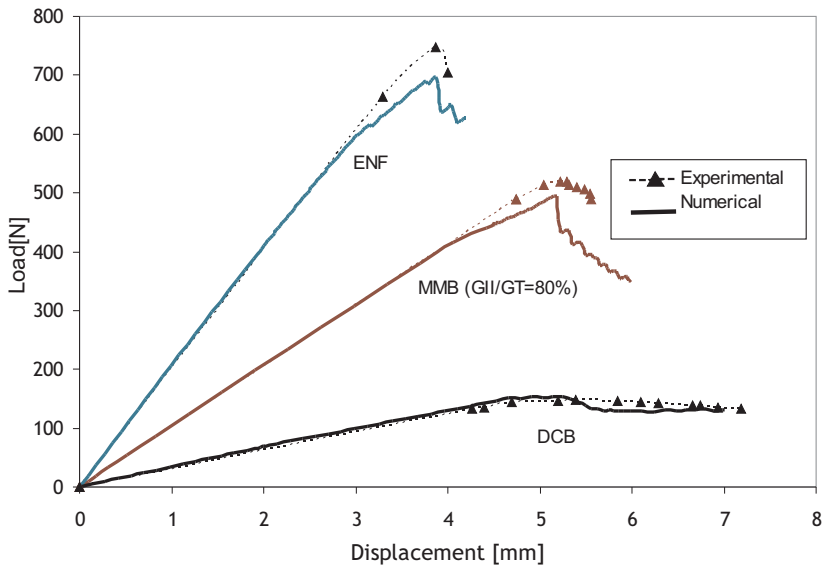

Figure A.6: Load-displacement curves for DCB, ENF and MMB 80% tests

Appendix B

Code

```
******************  ut-v1-r3.f  ********
*  DECO-UEL.V1                          *
*  Version 1.0                          *
*  Release 3                            *
*  2004 / 12 / 15                        *
****************************************
C
C           ----------------
C           | SUBROUTINE UEL |
C           ----------------
C
C   4 OR 8-NODE DECOHESION ELEMENT FOR THE SIMULATION OF
C   DELAMINATION ONSET AND GROWTH UNDER GENERALIZED LOADING
C   CONDITIONS.
C
C==============================================================
C
C    VARIABLES:
C
C    T1, T2: INTERFACIAL STRENGTH (MODE I, MODE II)
C    GIC, GIIC :  INTERFACIAL FRACTURE TOUGHNESS (MODE I, MODE II)
C    PEN: PENALTY STIFFNESS PARAMETER
C    ETA: Mode interaction parameter
C    THICK: Thickness of the element (2D)
C    IELEM: element label
C    KGASP: integration pt. n.
C    TAU: tractions TAU(KGASP,i), i=1-tau s, i=2-tau t
C      i=3-tau n
C    ASDIS: Displacement jump. ASDIS(KGASP,i)
C    BMATX: matrix of SHAPE functions [B]
C    SHAPE(i): ith SHAPE function
C    DERIV(j,i): derivative of the ith SHAPE function with respect
C          to the jth co-ordinate
C    XJACM: jacobean matrix
```

```
C    DMATX: matrix [D]
C    DTANG: tangent stiffness matrix [DTAN]
C    DNORMA3: absolute value of v3, ||v3||
C    SCALAR:  Scalar(KGASP) value used in the computation of DTANG
C    V(i,j): vectors on element surface
C    NGAUS: Number of Gauss points for each direction
C    NLGEOM: Geometrically non-linear
C    KF: Loading function
C
C--------------------------------------
C
C    ABAQUS VARIABLES
C
C    U: displacements (passed in)
C    RHS: residual vector
C    COORDS(k1,k2): k1 co-ordinate of the k2 node of an element
C    ESTIF : tangent stiffness matrix [KT]
C    NEVAB: n. of degrees of freedom
C    SVARS: solution-dependent variables
C    PNEWDT: control of time incrementation
C    DTIME: time increment
C    KINC: n. of current increment
C    PROPS: material properties
C    NDIME: dimension
C    NNODE: Number of nodes
C--------------------------------------
C
    SUBROUTINE UEL(RHS,ESTIF,SVARS,ENERGY,NEVAB,NRHS,NSVARS,
   .  PROPS,NPROPS,COORDS,NDIME,NNODE,U,DU,VEL,A,JTYPE,TIME,DTIME,
   .  KSTEP,KINC,IELEM,PARAMS,NDLOAD,JDLTYPE,ADLMAG,PREDEF,NPREDF,
   .  LFLAGS,MLVARX,DDLMAG,MDLOAD,PNEWDT,JPROPS,NJPROP,PERIOD)
C
     INCLUDE 'ABA_PARAM.INC'
C
* ---------------------------------------
C
     PARAMETER  (NGAUS = 2)  !Number of Gauss points for each direction
C
     DIMENSION RHS(MLVARX,*),ESTIF(NEVAB,NEVAB),SVARS(NSVARS),
   .   ENERGY(8),PROPS(*),COORDS(NDIME,NNODE),U(NEVAB),DU(MLVARX,*),
   .   VEL(NEVAB),A(NEVAB),TIME(2),PARAMS(*),JDLTYPE(MDLOAD,*),
   .   ADLMAG(MDLOAD,*),DDLMAG(MDLOAD,*),PREDEF(2,NPREDF,NNODE),
   .   LFLAGS(*),JPROPS(*)
C
     DIMENSION TAU(NNODE/2,NDIME),POSGP(NGAUS)
     DIMENSION ASDIS(NNODE/2,NDIME)
     DIMENSION DERIV(NDIME-1,NNODE),SHAPE(NNODE),V(NDIME,NDIME),
   .   BMATX(NDIME,NEVAB),WEIGP(NGAUS),DBMAT(NDIME,NEVAB),
   .   DMATX(NNODE/2,NDIME,NDIME),XJACM(NDIME-1,NDIME),
   .   KF(NNODE/2),SCALAR(NNODE/2),BMAT(NDIME,NEVAB)
C
     IF(NNODE.NE.8.AND.NNODE.NE.4) THEN
```

```
      WRITE(7,*)
   &   '* ERROR: Number of nodes of decohesion element: 4 or 8 *'
      WRITE(6,*)
   &   '* ERROR: Number of nodes of decohesion element: 4 or 8 *'
      STOP 911
     ENDIF
* ---------------------------------------
C    Initialization of preopened elements
* ---------------------------------------
     If(JTYPE.EQ.2) Then ! Ui is initially broken
      SVARS(1)=1.D0
      SVARS(2)=1.D0
      SVARS(3)=1.D0
      SVARS(4)=1.D0
     EndIf
* ---------------------------------------
C    Definition of properties
* ---------------------------------------
     CALL NUMPROP(GIC,GIIC,T1,T2,PEN,ETA,THICK,NLGEOM,PROPS,
   .  JPROPS,COORDS,NDIME,NNODE)
* ---------------------------------------
C    Initialization of variables
* ---------------------------------------
     DO IEVAB=1,NEVAB
      DO JEVAB=1,NEVAB
       ESTIF(IEVAB,JEVAB)=0.0D0  !STIFFNESS MATRIX
      ENDDO
       RHS(IEVAB,1)=0.0D0     !RESIDUAL FORCE VECTOR
     ENDDO
C
     IF(LFLAGS(4).NE.0)STOP 771
     IF(LFLAGS(3).EQ.1)THEN
* ---------------------------------------
C   definition of integration pt. co-ordinates & weigths
* ---------------------------------------
       CALL GAUSSQ(NGAUS,POSGP,WEIGP)
* ---------------------------------------
*    Calculation of tractions and residual vector          *
* ---------------------------------------
C
C    For each integration point:
C
      KGASP=0
      DO IGAUS=1,NNODE/2/NGAUS   !IGAUS
       DO JGAUS=1,NGAUS      !JGAUS
        KGASP=KGASP+1
* ---------------------------------------
C   position of integration points (4-node element):
C         x------------x____\  R
C         1       2
C   position of integration points (8-node element):
C             /|\ S
```

```
C              |
C         3    |    4
C         x------------x
C         |     |        |
C         |     |____ |____\  R
C         |              |   /
C         |             |
C         x------------x
C         1       2
* ----------------------------------------
         R=POSGP(JGAUS)
         S=POSGP(IGAUS)
* ----------------------------------------
C   definition of SHAPE functions and its derivatives
* ----------------------------------------
        CALL SFR3(DERIV,R,S,NDIME,SHAPE,NNODE)
* ----------------------------------------
C   calculation of Cartesian co-ordinates of integration pts.
C   v1, v2, v3 & ||v3||
* ----------------------------------------
        CALL JACOBT(DERIV,DNORMA3,COORDS,KGASP,NDIME,NNODE,
   .      SHAPE,V,XJACM,IELEM,NEVAB,U,THICK,NLGEOM)
        DAREA=0.0D0
        DAREA=DNORMA3*WEIGP(IGAUS)*WEIGP(JGAUS)
* ----------------------------------------
C   definition of matrix of SHAPE functions [B]
* ----------------------------------------
        CALL BMATT (SHAPE,NEVAB,NDIME,BMATX,V,NNODE,BMAT)
* ----------------------------------------
C   determination of relative displacements: delta = [B]*U(e)
* ----------------------------------------
        DO ISTRE=1,NDIME   !ISTRE
         ASDIS(KGASP,ISTRE)=0.0D0
         DO IEVAB=1,NEVAB  !IEVAB
          ASDIS(KGASP,ISTRE)=ASDIS(KGASP,ISTRE)+
   .        BMATX(ISTRE,IEVAB)*(U(IEVAB))
         ENDDO        !IEVAB
        ENDDO    !ISTRE
* ----------------------------------------
C   definition of matrix ([I]-[E])[D] (Dsr tensor)
* ----------------------------------------
        CALL MODT (NDIME,DMATX,KGASP,IELEM,
   &      PEN,ASDIS,T1,T2,GIC,GIIC,ETA,SVARS,KF,SCALAR,
   &      NNODE)
* ----------------------------------------
C   determination of tractions (local co-ordinates) TAUs=Dsr x DELTAr
* ----------------------------------------
        DO ISTRE=1,NDIME
         TAU(KGASP,ISTRE)=DMATX(KGASP,ISTRE,ISTRE)*
   .       ASDIS(KGASP,ISTRE)
        ENDDO
* ----------------------------------------
```

```
C   determination of residual vector
* ----------------------------------------
        DO IEVAB=1,NEVAB/2
         DO ISTRE=1,NDIME
          RHS(IEVAB,1)=RHS(IEVAB,1)-BMATX(ISTRE,IEVAB)*
   .        TAU(KGASP,ISTRE)*DAREA
         ENDDO
         RHS(IEVAB+NEVAB/2,1)=-RHS(IEVAB,1)
        ENDDO
C
* ----------------------------------------
C   calculation of the consistent tangent stiffness matrix
* ----------------------------------------
        CALL STIFF (NDIME,NEVAB,NNODE,DMATX,BMATX,KGASP,ASDIS,
   &     KF,SCALAR,DAREA,ESTIF,IELEM,KINC,KSTEP,PNEWDT,TIME,DTIME)
C
       ENDDO  !JGAUS
      ENDDO   !IGAUS
C
     ELSE
      Write(7,*)'*****WARNING LFLAGS(3)=',LFLAGS(3)
     END IF          ! LFLAGS(3)=1
     RETURN
    END
C
*****************SUBROUTINE NUMPROP*************
*
*     READ/DEFINE THE MATERIAL PROPERTIES
*
****************************************
C
    SUBROUTINE NUMPROP(GIC,GIIC,T1,T2,PEN,ETA,THICK,NLGEOM,PROPS,
   .  JPROPS,COORDS,NDIME,NNODE)
C
     INCLUDE 'ABA_PARAM.INC'
C
     DIMENSION COORDS(NDIME,NNODE),PROPS(*),JPROPS(*)
C
     GIC   = PROPS(1)
     GIIC  = PROPS(2)
     T1   = PROPS(3)
     T2   = PROPS(4)
     PEN   = PROPS(5)
     ETA   = PROPS(6)
     THICK  = PROPS(7)
     NLGEOM = JPROPS(1)
     RETURN
    END
C
*****************SUBROUTINE GAUSSQ**************
*
*     DEFINES POSITION & WEIGTH OF INTEGRATION POINTS
```

```
*
****************************************
C
    SUBROUTINE GAUSSQ (NGAUS,POSGP,WEIGP)
C
     INCLUDE 'ABA_PARAM.INC'
C
     DIMENSION POSGP(NGAUS),WEIGP(NGAUS)
C
     POSGP(1) = -1.0D0
     WEIGP(1) =  1.0D0
C
     KGAUS=NGAUS/2
     DO IGASH = 1,KGAUS
      JGASH = NGAUS+1-IGASH
      POSGP(JGASH) = - POSGP(IGASH)
      WEIGP(JGASH) =  WEIGP(IGASH)
     ENDDO
C
     RETURN
    END
C
*****************SUBROUTINE MODT**************
*
*            CALCULATES [D]
*
* ************************************************
C
    SUBROUTINE MODT (NDIME,DMATX,KGASP,IELEM,
   &  PEN,ASDIS,T1,T2,GIC,GIIC,ETA,SVARS,KF,
   &  SCALAR,NNODE)
C
     INCLUDE 'ABA_PARAM.INC'
C
     DIMENSION DMATX(NNODE/2,NDIME,NDIME),
   &   ASDIS(NNODE/2,NDIME),SVARS(*),
   &   KF(NNODE/2),SCALAR(NNODE/2)
C
     KF(KGASP) = 0
C
* ---------------------------------------
C  Solution dependent state variable DMAX: damage at the end of the
C  last converged increment
* ---------------------------------------
     DMAX = SVARS(KGASP)
     ODI = T1/PEN
     ODII = T2/PEN
C
     IF (NNODE/2.GT.2) THEN
      Dx  = ASDIS(KGASP,1)
      Dy  = ASDIS(KGASP,2)
      DI  = ASDIS(KGASP,3)
```

```
      DII  = DSQRT(Dx*Dx+Dy*Dy)
     ELSE
      Dx  = ASDIS(KGASP,1)
      DI  = ASDIS(KGASP,2)
      DII  = DSQRT(Dx*Dx)
     ENDIF
* ---------------------------------------
c  determine mixed-mode ratios
* ---------------------------------------
     IF (DI.LT.1.0D-19) THEN  !mode II
      BETA = 1.D0
      D=DII
     ELSE
      BETA = DII/(DI+DII)
      D = DSQRT(DI*DI+DII*DII)
     ENDIF
* ---------------------------------------
c   determine mixed-mode onset and final displacement
* ---------------------------------------
     If (ETA.LT.0.D0) Then      !  Power law criterion
      ALPHA = -ETA
      A = (1-BETA)**2+BETA**2
      OD = ODI*ODII*DSQRT(A)
   &    /(((1.D0-BETA)*ODII)**(2.D0*ALPHA)+(BETA*ODI)**
   &    (2.D0*ALPHA)**(1/(2.D0*ALPHA)))
      FD = 2.D0*A/
   &    (PEN*OD*(((1.D0-BETA)**2/GIc)**ALPHA+
   &    (BETA**2.D0/GIIc)**ALPHA)**(1.D0/ALPHA))
     Else               !  B-K criterion
      A = (BETA**2/(1+2*BETA**2-2*BETA))**ETA
      OD=DSQRT(ODI**2+(ODII**2-ODI**2)*A)
      FD = 2*(GIc+(GIIc-GIc)*A)/(PEN*OD)
     Endif
* ---------------------------------------
c   calculate mixed-mode damage threeshold
* ---------------------------------------
     R = OD*FD/(FD-DMAX*(FD-OD))
* ---------------------------------------
c   update internal variables
* ---------------------------------------
     If (D.GT.R) THEN
      R = D         ! maximum damage
      KF(KGASP) = 1     ! loading function
     ELSE
      KF(KGASP) = 0     ! unloading
     endif
     DMAX = FD*(R-OD)/(R*(FD-OD))
     IF (DMAX.GT.1.0D0) THEN     !if fully open
      DMAX = 1.D0
      KF(KGASP) = 0
     ENDIF
CC
```

```
     DO I=1,NDIME
      DO J=1,NDIME
       DMATX(KGASP,I,J)=0.D0
      ENDDO
      DMATX(KGASP,I,I)=(1.0D0-DMAX)*PEN
     ENDDO
     IF (DI.LT.0.D0) DMATX(KGASP,NDIME,NDIME)= PEN     ! interpenetration
C
* ---------------------------------------
C   Calculate scalar parameter used in the definition of the
C   consistent tangent stiffness of softening points for loading
C   conditions
* ---------------------------------------
     IF(KF(KGASP).EQ.1) SCALAR(KGASP) = FD*OD*PEN/(R**3*(FD-OD))
* ---------------------------------------
C   Update state variables
* ---------------------------------------
     SVARS(KGASP)      = DMA   X ! damage variable
C
     RETURN
    END
***************** SUBROUTINE STIFF *************
*
*          CALCUTATES THE CONSISTENT
*         TANGENT STIFFNESS MATRIX, [KT]
*
***********************************************
C
    SUBROUTINE STIFF (NDIME,NEVAB,NNODE,DMATX,BMATX,KGASP,ASDIS,
   &  KF,SCALAR,DAREA,ESTIF,IELEM,KINC,KSTEP,PNEWDT,TIME,DTIME)
C
     INCLUDE 'ABA_PARAM.INC'
C
     PARAMETER (ITMAX = 15)  !Max. iterations with tangent stiffness
C
     DIMENSION ESTIF(NEVAB,NEVAB),DMATX(NNODE/2,NDIME,NDIME),
   .   SCALAR(NNODE/2),ASDIS(NNODE/2,NDIME),BMATX(NDIME,NEVAB),
   .   DTANG(NNODE/2,NDIME,NDIME),DBMAT(NDIME,NEVAB),KF(NNODE/2),
   .   TIME(2)
     COMMON /KZERO/ KSEC
     COMMON /KINCREMENTZ/ KINC1
     COMMON /KCOUNTINGZ/ KCOUNT
     COMMON /KAUX/ KELEMENT
     COMMON /KELLABEL/ KLABEL
     COMMON /KCHSTEP/ KSTEP1
     COMMON TI
C
     IF(KELEMENT.NE.1) THEN
      KLABEL  = IELEM
      KELEMENT = 1
     ENDIF
C
```

```
* ----------------------------------------
C    Counter of the number of iterations
* ----------------------------------------
     IF(KINC.NE.KINC1.AND.KSTEP1.NE.KSTEP) THEN
      IF(IELEM.EQ.KLABEL) THEN
       KCOUNT = KCOUNT+1
       KINC1  = KINC+1
       KSTEP1 = KSTEP+1
      ENDIF
     ELSE
      KCOUNT = 0
      KINC1  = KINC+1
      KSTEP1 = KSTEP +1
      KSEC  = 0
      TI = DTIME
     ENDIF
     IF(KCOUNT.GE.ITMAX*NNODE/2) THEN
      IF(DTIME.NE.TI) THEN
       KCOUNT = 0
       TI = DTIME
       KSEC = 1
      ENDIF
     ENDIF
* ----------------------------------------
C    Reduce time increment and use SECANT Dsr for it > itmax
* ----------------------------------------
     IF (IELEM.EQ.KLABEL.AND.KCOUNT.GE.ITMAX*NNODE/2.AND.KSEC.NE.1)
   .   pnewdt = 0.9d0
     DO I=1, NDIME
      DO J=1, NDIME
       DTANG(KGASP,I,J)=DMATX(KGASP,I,J)
      END DO
     END DO
* ----------------------------------------
C    TANGENT STIFFNESS MATRI  X DTAN
* ----------------------------------------
     IF (KCOUNT.LT.(ITMAX+1)*NNODE/2)  THEN
      IF(KF(KGASP).EQ.1) THEN   !LOADING
       DO I=1, NDIME
        DO J=1, NDIME
         DTANG(KGASP,I,J)=DMATX(KGASP,I,J)
   .       -SCALAR(KGASP)*ASDIS(KGASP,J)*ASDIS(KGASP,I)
        END DO
       END DO
       IF (ASDIS(KGASP,NDIME).LT.0.D0) THEN  !PENETRATION
        DO I=1,NDIME
         DTANG(KGASP,NDIME,I)=DMATX(KGASP,NDIME,I)
         DTANG(KGASP,I,NDIME)=DMATX(KGASP,I,NDIME)
        END DO
       ENDIF   !PENETRATION
      ENDIF  !LOADING
     ELSE
```

```
     ENDIF
* ---------------------------------------
C   calculate [DTAN]x[B]
* ---------------------------------------
     DO I=1,NDIME
      DO J=1,NEVAB
       DBMAT(I,J)=0.0D0
       DO K=1,NDIME
        DBMAT(I,J)=DBMAT(I,J)+DTANG(KGASP,I,K)*BMATX(K,J)
       ENDDO
      ENDDO
     ENDDO
* ---------------------------------------
C    calculate [BT]x[DTAN]x[B]dA
* ---------------------------------------
     DO IEVAB=1,NEVAB
      DO JEVAB=1,NEVAB
       DO ISTRE=1,NDIME
        ESTIF(IEVAB,JEVAB)=ESTIF(IEVAB,JEVAB)+BMATX(ISTRE,IEVAB)*
   .      DBMAT(ISTRE,JEVAB)*DAREA
       ENDDO  !ISTRE
      ENDDO   !JEVAB
     ENDDO    !IEVAB
C
     RETURN
    END
***************** SUBROUTINE BMATT *************
*
*         CALCULATES SHAPE FUNCTIONS MATRIX B
*
***********************************************
C
    SUBROUTINE BMATT (SHAPE,NEVAB,NDIME,BMATX,V,NNODE,BMAT)
C
     INCLUDE 'ABA_PARAM.INC'
C
     DIMENSION SHAPE(NNODE),BMATX(NDIME,NEVAB),BMAT(NDIME,NEVAB),
   .   V(NDIME,NDIME)
* ---------------------------------------
C     definiton of [B] in local co-ordinates
* ---------------------------------------
     DO I=1,NDIME
      DO J=1,NEVAB
       BMAT(I,J)=0.0D0
      ENDDO
     ENDDO
     DO I=1,NDIME
      K=0
      DO J=I,NEVAB,NDIME
       K=K+1
       BMAT(I,J)=SHAPE(K)
      ENDDO
```

```
      ENDDO
* ---------------------------------------
C     definiton of [B] in global co-ordinates
C     [B]=[theta]T x [N, -N]
* ---------------------------------------
      DO I=1,NDIME
       DO J=1,NEVAB
        BMATX(I,J)=0.0D0
        DO M=1,NDIME
         BMATX(I,J)=BMATX(I,J)+V(I,M)*BMAT(M,J)
        ENDDO
       ENDDO
      ENDDO
      RETURN
     END
C
****************SUBROUTINE JACOBT********
*
*    CALCULATES THE CARTESIAN COORDINATES OF INTEGRATION POINTS
*    CALCULATES THE VECTORS V1, V2 AND V3
*    CALCULATES THE NORM OF V3 (DNORMA3)
*
****************************************
C
     SUBROUTINE JACOBT (DERIV,DNORMA3,COORDS,KGASP,NDIME,NNODE,
    .  SHAPE,V,XJACM,IELEM,NEVAB,U,THICK,NLGEOM)
C
      INCLUDE 'ABA_PARAM.INC'
C
      DIMENSION DERIV(NDIME-1,NNODE),COORDS(NDIME,NNODE),
    .   SHAPE(NNODE),V(NDIME,NDIME),
    .   XJACM(NDIME-1,NDIME),U(NEVAB)
* ---------------------------------------
C   Definition of Jacobean matrix (3X2)
* ---------------------------------------
      DO IDIME=1,NDIME-1
       DO JDIME=1,NDIME
        XJACM(IDIME,JDIME)=0.0D0
        DO INODE=1,NNODE/2
         IF(NLGEOM.EQ.1) THEN
          XJACM(IDIME,JDIME)=XJACM(IDIME,JDIME)+DERIV(IDIME,INODE)
    .       *(COORDS(JDIME,INODE)+
    .       0.5D0*(U((INODE-1)*NDIME+JDIME)+
    .       U((INODE+NNODE/2-1)*NDIME+JDIME)))
         ELSE
          XJACM(IDIME,JDIME)=XJACM(IDIME,JDIME)+DERIV(IDIME,INODE)
    .       *(COORDS(JDIME,INODE))
         ENDIF
        ENDDO
       ENDDO
      ENDDO
* ---------------------------------------
```

```
C    Definition of vector v1
C    v1=vxi/||vxi||
* ---------------------------------------
     DNORMA1=0.0D0
     DO IDIME=1,NDIME
      DNORMA1=DNORMA1+XJACM(1,IDIME)**2
     ENDDO
     DNORMA1=DSQRT(DNORMA1)
     DO I=1,NDIME
      DO J=1,NDIME
       V(I,J)=0.0D0
      ENDDO
     ENDDO
     IF(NNODE.GE.8) THEN
      V(1,1)=XJACM(1,1)/DNORMA1
      V(1,2)=XJACM(1,2)/DNORMA1
      V(1,3)=XJACM(1,3)/DNORMA1
* ---------------------------------------
C   Definition of the vector v3 and its norm
C   v3=vxi x veta
* ---------------------------------------
      V(3,1)=XJACM(1,2)*XJACM(2,3)-XJACM(2,2)*XJACM(1,3)
      V(3,2)=XJACM(2,1)*XJACM(1,3)-XJACM(1,1)*XJACM(2,3)
      V(3,3)=XJACM(1,1)*XJACM(2,2)-XJACM(2,1)*XJACM(1,2)
      DNORMA3=0.D0
      DO IDIME=1,NDIME
       DNORMA3=DNORMA3+V(3,IDIME)**2
      ENDDO
      DNORMA3=DSQRT(DNORMA3)
      V(3,1)=V(3,1)/DNORMA3
      V(3,2)=V(3,2)/DNORMA3
      V(3,3)=V(3,3)/DNORMA3
* ---------------------------------------
C    Definition of vector v2
* ---------------------------------------
      V(2,1)=V(3,2)*V(1,3)-V(1,2)*V(3,3)
      V(2,2)=V(1,1)*V(3,3)-V(3,1)*V(1,3)
      V(2,3)=V(3,1)*V(1,2)-V(3,2)*V(1,1)
     ELSE
      V(1,1)=XJACM(1,1)/DNORMA1
      V(1,2)=-XJACM(1,2)/DNORMA1
      V(2,1)=XJACM(1,2)/DNORMA1
      V(2,2)=XJACM(1,1)/DNORMA1
      DNORMA3 = DNORMA1*THICK
     ENDIF
     RETURN
    END
*****************SUBROUTINE SFR3************ *
*     CALCULATES SHAPE FUNCTIONS & ITS DERIVATIVES
*
*****************************************
C
```

```
    SUBROUTINE SFR3 (DERIV,R,S,NDIME,SHAPE,NNODE)
C
     INCLUDE 'ABA_PARAM.INC'
     DIMENSION SHAPE(NNODE),DERIV(NDIME-1,NNODE)
C
     RP=1.0D0+R
     RN=1.0D0-R
     SP=1.0D0+S
     SN=1.0D0-S
     RR=1.0D0-R*R
     SS=1.0D0-S*S
     DO I=1,NNODE
      SHAPE(I)=0.0D0
      DO J=1,NDIME-1
       DERIV(J,I)=0.0D0
      ENDDO
     ENDDO
     IF (NNODE.EQ.8) THEN
      SHAPE(1)=RN*SN/4.0D0
      SHAPE(2)=RP*SN/4.0D0
      SHAPE(3)=RP*SP/4.0D0
      SHAPE(4)=RN*SP/4.0D0
      DERIV(1,1)=-SN/4.D0
      DERIV(2,1)=-RN/4.D0
      DERIV(1,2)= SN/4.D0
      DERIV(2,2)=-RP/4.D0
      DERIV(1,3)= SP/4.D0
      DERIV(2,3)= RP/4.D0
      DERIV(1,4)=-SP/4.D0
      DERIV(2,4)= RN/4.D0
     ELSEIF (NNODE.EQ.4) THEN
      SHAPE(1)=RN/2.0D0
      SHAPE(2)=RP/2.0D0
      DERIV(1,1)=-0.5D0
      DERIV(1,2)= 0.5D0
     ENDIF
     DO I=1,NNODE/2
      DO J=1,NDIME-1
       DERIV(J,I+NNODE/2)=DERIV(J,I)
      ENDDO
      SHAPE(I+NNODE/2)=SHAPE(I)
      SHAPE(I)=-SHAPE(I+NNODE/2)
     ENDDO
     RETURN
    END
*=====================================================*
*            END OF PROGRAM
*=====================================================*
```

Appendix C

Input files

C.1 One element simulations

C.1.1 Input file for an 8-node decohesion element that connects two three dimensional continuum elements.

```
*HEADING DCB with two SOLID elements connected by a decohesion
element ** ** CLAMPED AT THE END, DISPLACEMENTS AT THE CRACK FACES
** *Node
 1, 1., 1., 1.
 2, 1., 0., 1.
 3, 1., 1., 0.
 4, 1., 0., 0.
 5, 0., 1., 1.
 6, 0., 0., 1.
 7, 0., 1., 0.
 8, 0., 0., 0.
 11, 1., 1., -1.
 12, 1., 0., -1.
 13, 1., 1., 0.
 14, 1., 0., 0.
 15, 0., 1., -1.
 16, 0., 0., -1.
 17, 0., 1., 0.
 18, 0., 0., 0.
*NSET,NSET=FDALT
 7,8
*NSET,NSET=FBAIX
 17,18
*NSET,NSET=CLAMP
 3,4
```

```
 13,14
*Element, type=C3D8R
101, 5, 6, 8, 7, 1, 2, 4, 3 111, 11, 12, 14,
13,15, 16, 18, 17 **
*ELSET, ELSET=SOLIDO
 101,111
**
*USER ELEMENT,TYPE=U1,NODES=8,UNSYMM,COORDINATES=3,
 I PROPERTIES=1, PROPERTIES=7, VARIABLES=4
 1,2,3
*ELEMENT,TYPE=U1
 51,8,7,3,4,18,17,13,14
*ELSET,ELSET=INTER
 51
*UEL PROPERTY,ELSET=INTER
** GIc GIIc SI SII Kp Eta
 0.268, 0.632, 45.0, 45.0, 1.E+6, 2.1 , 0 , 5 , 4
*ORIENTATION,NAME=OR1
 1.,0.,0.,0.,1.,0.
*SOLID SECTION,MATERIAL=CFRP,ELSET=SOLIDO,ORIENTATION=OR1
*MATERIAL,NAME=CFRP
*ELASTIC,TYPE=ENGINEERING CONSTANTS
 150.E+03,11.E+03,11.E+03,0.25,0.25,0.45,6.E+03,6.E+03
 3.7E+03
*BOUNDARY
 CLAMP,ENCASTRE
** *PREPRINT,ECH=NO,HISTORY=NO,MODEL=NO
*RESTART,WRITE,FREQ=4,OVERLAY
*STEP,INC=1000
 16mm displacement
*STATIC
 0.005,0.40625,,0.005
*BOUNDARY,TYPE=DISP
 FDALT,3,3, .000100
 FBAIX,3,3,-.000100
*CONTROLS,PARAMETERS=FIELD,FIELD=DISPLACEMENT
 .05,1.0
*CONTROLS,PARAMETERS=TIME INCREMENTATION
 1500,1500,,1500,1500
*CONTROLS,PARAMETERS=LINE SEARCH
 4,4,0.25,0.25,0.15
*OUTPUT,HISTORY,FREQUENCY=1
*NODE OUTPUT,NSET=FDALT
 U3
*NODE OUTPUT,NSET=FBAIX
 RF3
*OUTPUT,FIELD,FREQUENCY=1
*NODE OUTPUT
 U
*ELEMENT OUTPUT
 S
*END STEP
```

```
*STEP,INC=1000
 Displacement back to zero (unloading)
*STATIC
 0.02,0.50,,0.02
*BOUNDARY,TYPE=DISP
 FDALT,3,3, 0.00
 FBAIX,3,3, 0.00
*CONTROLS,PARAMETERS=FIELD,FIELD=DISPLACEMENT
 .05,1.0
*CONTROLS,PARAMETERS=TIME INCREMENTATION
 1500,1500,,1500,1500
*CONTROLS,PARAMETERS=LINE SEARCH
 4,4,0.25,0.25,0.15
*OUTPUT,HISTORY,FREQUENCY=1
*NODE OUTPUT,NSET=FDALT
 U3
*NODE OUTPUT,NSET=FBAIX
 RF3
*OUTPUT,FIELD,FREQUENCY=1
*NODE OUTPUT
 U
*ELEMENT OUTPUT
 S
*END STEP
```

C.1.2 Input file for an 4-node decohesion element that connects two continuum plane strain element

```
*HEADING DCB with two shell elements connected by a decohesion
element ** ** CLAMPED AT THE END, DIPLACEMENTS AT THE CRACK FACES
** *Node
 1, 0,0.,
 2, 0.,1.,
 3, -1.,1.,
 4, -1.,0.,
 11, 0.,0.,
 12, 0.,1.,
 13, 1.,1.,
 14, 1.,0.,
*NSET,NSET=FDALT
 12
*NSET,NSET=FBAIX
 2
*NSET,NSET=CLAMP
 1,11
*Element, type=CPE4 101, 4,1,2,3, 111, 11, 14,13,12 **
*ELSET,
ELSET=SOLIDO
 101,111
**
*USER ELEMENT,TYPE=U1,NODES=4,UNSYMM,COORDINATES=2,
 I PROPERTIES=1, PROPERTIES=7, VARIABLES=4
 1,2
*ELEMENT,TYPE=U1
 51,1,2,11,12
*ELSET,ELSET=INTER
 51
*UEL PROPERTY,ELSET=INTER
** GIc GIIc SI SII Kp Eta Thick NLGEOM
 0.268, 0.632, 45.0, 45.0, 1.E+6, 2.1 , 1.,1
*ORIENTATION,NAME=OR1
 1.,0.,0.,0.,1.,0.
*SOLID SECTION,MATERIAL=CFRP,ELSET=SOLIDO,ORIENTATION=OR1
1
*MATERIAL,NAME=CFRP
*ELASTIC,TYPE=ENGINEERING CONSTANTS
 150.E+03,11.E+03,11.E+03,0.25,0.25,0.45,6.E+03,6.E+03
 3.7E+03
*BOUNDARY
 CLAMP,ENCASTRE
*RESTART,WRITE,FREQ=4,OVERLAY
*STEP,INC=1000
 16mm displacement
*STATIC
 0.005,0.40625,,0.005
*BOUNDARY,TYPE=DISP
```

```
 FDALT,1,1, .000100
 FBAIX,1,1,-.000100
*CONTROLS,PARAMETERS=FIELD,FIELD=DISPLACEMENT
 .05,1.0
*CONTROLS,PARAMETERS=TIME INCREMENTATION
 1500,1500,,1500,1500
*CONTROLS,PARAMETERS=LINE SEARCH
 4,4,0.25,0.25,0.15
*OUTPUT,HISTORY,FREQUENCY=1
*NODE OUTPUT,NSET=FDALT
 U1
*NODE OUTPUT,NSET=FBAIX
 RF1
*OUTPUT,FIELD,FREQUENCY=1
*NODE OUTPUT
 U
*ELEMENT OUTPUT
 S
*END STEP
*STEP,INC=1000
 Displacement back to zero (unloading)
*STATIC
 0.02,0.50,,0.02
*BOUNDARY,TYPE=DISP
 FDALT,1,1, 0.00
 FBAIX,1,1, 0.00
*CONTROLS,PARAMETERS=FIELD,FIELD=DISPLACEMENT
 .05,1.0
*CONTROLS,PARAMETERS=TIME INCREMENTATION
 1500,1500,,1500,1500
*CONTROLS,PARAMETERS=LINE SEARCH
 4,4,0.25,0.25,0.15
*OUTPUT,HISTORY,FREQUENCY=1
*NODE OUTPUT,NSET=FDALT
 U1
*NODE OUTPUT,NSET=FBAIX
 RF1
*OUTPUT,FIELD,FREQUENCY=1
*NODE OUTPUT
 U
*ELEMENT OUTPUT
 S
*END STEP
```

C.1.3 Input file for an 4-node decohesion element that connects two continuum plane strain element. Rotated 90º.

```
*HEADING DCB with two shell elements connected by a decohesion
element ** ** CLAMPED AT THE END, DIPLACEMENTS AT THE CRACK FACES
** *Node
 1, 0, 0.,
 2, 1., 0.,
 3, 1., -1.,
 4, 0., -1.,
 11, 0., 0.,
 12, 1., 0.,
 13, 1., 1.,
 14, 0., 1.,
*NSET,NSET=FDALT
 12
*NSET,NSET=FBAIX
 2
*NSET,NSET=CLAMP
 1,11
** GENERATION OF ELEMENTS ** ** ***************************** **
*Element, type=CPE4 101, 1,4,3,2 111, 11, 12, 13, 14 *ELSET,
ELSET=SOLIDO
 101,111
*USER ELEMENT,TYPE=U1,NODES=4,UNSYMM,COORDINATES=2,
 I PROPERTIES=1, PROPERTIES=7, VARIABLES=4
 1,2
*ELEMENT,TYPE=U1
 51,1,2,11,12
*ELSET,ELSET=INTER
 51
*UEL PROPERTY,ELSET=INTER
** GIc GIIc SI SII Kp Eta Thick NLGEOM
 0.268, 0.632, 45.0, 45.0, 1.E+6, 2.1 , 1.,1
*ORIENTATION,NAME=OR1
 1.,0.,0.,0.,1.,0.
*SOLID SECTION,MATERIAL=CFRP,ELSET=SOLIDO,ORIENTATION=OR1
1
*MATERIAL,NAME=CFRP
*ELASTIC,TYPE=ENGINEERING CONSTANTS
 150.E+03,11.E+03,11.E+03,0.25,0.25,0.45,6.E+03,6.E+03
 3.7E+03
*BOUNDARY
 CLAMP,ENCASTRE
** *PREPRINT,ECH=NO,HISTORY=NO,MODEL=NO
*RESTART,WRITE,FREQ=4,OVERLAY
*STEP,INC=1000
 16mm displacement
*STATIC
```

```
 0.005,0.40625,,0.005
*BOUNDARY,TYPE=DISP
 FDALT,2,2, .000100
 FBAIX,2,2,-.000100
*CONTROLS,PARAMETERS=FIELD,FIELD=DISPLACEMENT
 .05,1.0
*CONTROLS,PARAMETERS=FIELD,FIELD=DISPLACEMENT
*CONTROLS,PARAMETERS=TIME INCREMENTATION
 1500,1500,,1500,1500
*CONTROLS,PARAMETERS=LINE SEARCH
 4,4,0.25,0.25,0.15
*OUTPUT,HISTORY,FREQUENCY=1
*NODE OUTPUT,NSET=FDALT
 U2
*NODE OUTPUT,NSET=FBAIX
 RF2
*OUTPUT,FIELD,FREQUENCY=1
*NODE OUTPUT
 U
*ELEMENT OUTPUT
 S
*END STEP
*STEP,INC=1000
 Displacement back to zero (unloading)
*STATIC
 0.02,0.50,,0.02
*BOUNDARY,TYPE=DISP
 FDALT,2,2, 0.00
 FBAIX,2,2, 0.00
*CONTROLS,PARAMETERS=FIELD,FIELD=DISPLACEMENT
 .05,1.0
*CONTROLS,PARAMETERS=TIME INCREMENTATION
 1500,1500,,1500,1500
*CONTROLS,PARAMETERS=LINE SEARCH
 4,4,0.25,0.25,0.15
*OUTPUT,HISTORY,FREQUENCY=1
*NODE OUTPUT,NSET=FDALT
 U2
*NODE OUTPUT,NSET=FBAIX
 RF2
*OUTPUT,FIELD,FREQUENCY=1
*NODE OUTPUT
 U
*ELEMENT OUTPUT
 S
*END STEP
```

C.2 Mode I, mode II and mixed-mode delamination growth for a PEEK composites

C.2.1 Input file for the DCB test.

```
*HEADING DCB ** ** CLAMPED AT THE END, DIPLACEMENTS AT THE CRACK
FACES ** *NODE
 1, 0.00, 0.00, 0.00
 301,102.00, 0.00, 0.00
 .
 .
 .
 30301,102.00, 0.00, 3.12
 34001, 0.00, 25.40, 3.12
 34301,102.00, 25.40, 3.12
*NGEN,NSET=A
 1, 301
 5001, 5301
 10001,10301
 20001,20301
 25001,25301
 30001,30301
*NGEN,NSET=B
 4001, 4301
 9001, 9301
 14001,14301
 24001,24301
 29001,29301
 34001,34301
*NFILL,NSET=ALL
 A,B,8,500
** nsets ** ***************************
*NSET,NSET=BOT,GEN
 1,4001,500
*NSET,NSET=TOP,GEN
 30001,34001,500
*NSET,NSET=CLAMP,GEN
 301, 4301,500
 5301, 9301,500
10301,14301,500
20301,24301,500
25301,29301,500
30301,34301,500
***************************
**
** GENERATION OF ELEMENTS **
**
***************************
*ELEMENT,TYPE=C3D8I
```

```
 1001,1,3,1003,1001,10001,10003,11003,11001
*ELGEN,ELSET=SOLIDO
 1001, 150, 2, 1, 4, 1000, 150, 2,20000,2000
**
*USER ELEMENT,TYPE=U1,NODES=8,UNSYMM,COORDINATES=3,
 I PROPERTIES=1, PROPERTIES=7,VARIABLES=4
 1,2,3
*ELEMENT,TYPE=U1
 1,10097,10099,11099,11097,20097,20099,21099,21097
*ELGEN,ELSET=INTER
 1, 102, 2, 1, 4, 1000, 102
*UEL PROPERTY,ELSET=INTER
** GIc GIIc SI SII Kp Eta Thick NLGEOM
 0.9690, 1.719, 80.0, 115.0, 1.E+6, 2.0,, 1
*ORIENTATION,NAME=OR1
 1.,0.,0.,0.,1.,0.
 3,0.
*SOLID SECTION,MATERIAL=CFRP,ELSET=SOLIDO,ORIENTATION=OR1
*MATERIAL,NAME=CFRP
*ELASTIC,TYPE=ENGINEERING CONSTANTS
 122.7E+03,10.1E+03,10.1E+03,0.25,0.25,0.45,5.5E+03,5.5E+03
 3.7E+03
**
** BOUNDARY CONDITIONS**
**
*BOUNDARY
 CLAMP,ENCASTRE
**
*PREPRINT,ECH=NO,HISTORY=NO,MODEL=NO
*RESTART,WRITE,FREQ=4,OVERLAY
**
******************
**
** STEP 1 **
**
******************
*STEP,INC=10000
 2mm displacement
*STATIC
 0.040,0.286,,0.02
*BOUNDARY,TYPE=DISP
 TOP,3,3, 1.0
 BOT,3,3,-1.0
*CONTROLS,PARAMETERS=FIELD,FIELD=DISPLACEMENT
 .05,1.0
*CONTROLS,PARAMETERS=TIME INCREMENTATION
 1500,1500,,1500,1500
*CONTROLS,PARAMETERS=LINE SEARCH
 4,4,0.25,0.25,0.15
*OUTPUT,HISTORY,FREQUENCY=1
*NODE OUTPUT,NSET=TOP
 U3
```

```
*NODE OUTPUT,NSET=BOT
 RF3
*NODE OUTPUT,NSET=TOP
*OUTPUT,FIELD,FREQUENCY=2
*NODE OUTPUT
 U
*ELEMENT OUTPUT
 S
*END STEP
*****************
**
** STEP 2 **
**
*****************
*STEP,INC=10000
 7mm displacement
*STATIC
 0.02,0.714,,0.02
*BOUNDARY,TYPE=DISP
 TOP,3,3, 3.5
 BOT,3,3,-3.5
*CONTROLS,PARAMETERS=FIELD,FIELD=DISPLACEMENT
 .05,1.0
*CONTROLS,PARAMETERS=TIME INCREMENTATION
 1500,1500,,1500,1500
*CONTROLS,PARAMETERS=LINE SEARCH
 4,4,0.25,0.25,0.15
*OUTPUT,HISTORY,FREQUENCY=1
*NODE OUTPUT,NSET=TOP
 U3
*NODE OUTPUT,NSET=BOT
 RF3
*OUTPUT,FIELD,FREQUENCY=2
*NODE OUTPUT
 U
*ELEMENT OUTPUT
 S
*END STEP
*************************
** END **
*************************
```

C.2.2 Input file for the ENF test.

```
*HEADING ENF ** *NODE
 1, 0.00, 0.00, 0.00
 301,102.00, 0.00, 0.00
 .
 .
 .
  34001, 0.00, 25.40, 3.12
 34301,102.00, 25.40, 3.12
*NGEN,NSET=A
 1, 301
 5001, 5301
 10001,10301
 20001,20301
 25001,25301
 30001,30301
*NGEN,NSET=B
 4001, 4301
 9001, 9301
 14001,14301
 24001,24301
 29001,29301
 34001,34301
*NFILL,NSET=ALL
 A,B,8,500
** nsets ** ***************************
*NSET,NSET=BOT,GEN
 1,4001,500
*NSET,NSET=TOP,GEN
 30001,34001,500
*NSET,NSET=BOTEND,GEN
 301,4301,500
*NSET,NSET=TOPMID,GEN
 30151,34151,500
*NSET,NSET=CLAMP,GEN
 301, 4301,500
 5301, 9301,500
10301,14301,500 20301,24301,500 25301,29301,500 30301,34301,500
*******************************************************
*ELEMENT,TYPE=C3D8I
 1001,1,3,1003,1001,10001,10003,11003,11001
**
*ELGEN,ELSET=SOLIDO
 1001, 150, 2, 1, 4, 1000, 150, 2,20000,2000
**
*USER ELEMENT,TYPE=U2,NODES=8,UNSYMM,COORDINATES=3,
 I PROPERTIES=1,PROPERTIES=7,VARIABLES=4
 1,2,3
*ELEMENT,TYPE=U2
 1,10001,10003,11003,11001,20001,20003,21003,21001
*USER ELEMENT,TYPE=U1,NODES=8,UNSYMM,COORDINATES=3,
```

```
 I PROPERTIES=1,PROPERTIES=7,VARIABLES=4
 1,2,3
*ELEMENT,TYPE=U1
 233,10117,10119,11119,11117,20117,20119,21119,21117
*ELGEN,ELSET=DECOPEN
 1,58,2,1,4,1000,58
*ELGEN,ELSET=DECLOSED
 233,92,2,1,4,1000,92
*UEL PROPERTY,ELSET=DECOPEN
** GIc GIIc SI SII Kp Eta Thick NLGEOM
 0.9690, 1.719, 80.0, 100.0, 1.E+6, 2.284, , 1
*UEL PROPERTY,ELSET=DECLOSED
** GIc GIIc SI SII Kp Eta Thick
NLGEOM
 0.9690, 1.719, 80.0, 100.0, 1.E+6, 2.284, , 1
*ORIENTATION,NAME=OR1
 1.,0.,0.,0.,1.,0.
 3,0.
*SOLID SECTION,MATERIAL=CFRP,ELSET=SOLIDO,ORIENTATION=OR1
*MATERIAL,NAME=CFRP
*ELASTIC,TYPE=ENGINEERING CONSTANTS
 122.7E+03,10.1E+03,10.1E+03,0.25,0.25,0.45,5.5E+03,5.5E+03
 3.7E+03
**BOUNDARY CONDITIONS **
**
*BOUNDARY
 BOT ,3,3
 BOTEND,1,3
** BOT,PINNED
** BOTEND,2,3
**
*PREPRINT,ECH=NO,HISTORY=NO,MODEL=NO
*RESTART,WRITE,FREQ=4,OVERLAY
**
******************
**
** STEP 1 **
**
******************
*STEP,INC=10000,NLGEOM
 2mm displacement
*STATIC
 0.040,0.44,,0.02
*BOUNDARY,TYPE=DISP
 TOPMID,3,3,-2.
*CONTROLS,PARAMETERS=FIELD,FIELD=DISPLACEMENT ** .1,1.0
 .02,.5,,,0.04
*CONTROLS,PARAMETERS=TIME INCREMENTATION
 1500,1500,200,1500,100
*OUTPUT,HISTORY,FREQUENCY=1 *NODE OUTPUT,NSET=TOPMID
 U3
*NODE OUTPUT,NSET=BOTEND
```

```
 RF3
*NODE OUTPUT,NSET=BOT
 RF3
*OUTPUT,FIELD,FREQUENCY=10
*NODE OUTPUT
 U,RF
*ELEMENT OUTPUT
 S
*END STEP
*****************
**
** STEP 2 **
**
*****************
*STEP,INC=10000,NLGEOM
 4.5mm displacement
*STATIC
 0.005,0.56,,0.005
*BOUNDARY,TYPE=DISP
 TOPMID,3,3,-4.5
*CONTROLS,PARAMETERS=FIELD,FIELD=DISPLACEMENT
 0.05,0.5,,,0.004
*CONTROLS,PARAMETERS=TIME INCREMENTATION
 1500,1500,400,1500,100
*CONTROLS,PARAMETERS=LINE SEARCH
 4,4,0.25,0.25,0.15
*OUTPUT,HISTORY,FREQUENCY=1
*NODE OUTPUT,NSET=TOPMID
 U3
*NODE OUTPUT,NSET=BOTEND
 RF3
*NODE OUTPUT,NSET=BOT
 RF3
*OUTPUT,FIELD,FREQUENCY=10
*NODE OUTPUT
 U,RF
*ELEMENT OUTPUT
 S
*END STEP
```

C.2.3 Input file for the MMB 80 test.

```
*HEADING MMB
GII/GT = 80%
**
** CLAMPED AT THE END, DIPLACEMENTS AT THE CRACK FACES
**
*NODE
 1, 0.00, 0.00, 0.00
 301,102.00, 0.00, 0.00
 .
 .
 .
 34001, 0.00, 25.40, 3.12
 34301,102.00, 25.40, 3.12
** lever nodes
 40301, 27.58, 0.00,15.00
 44301, 27.58, 25.40,15.00
 43301, 27.58, 19.05,15.00
 42301, 27.58, 12.70,15.00
 41301, 27.58, 6.35,15.00
*NGEN,NSET=A
 1, 301
 5001, 5301
 10001,10301
 20001,20301
 25001,25301
 30001,30301
*NGEN,NSET=B
 4001, 4301
 9001, 9301
 14001,14301
 24001,24301
 29001,29301
 34001,34301
*NFILL,NSET=ALL
 A,B,8,500
***************************
**
** nsets
**
***************************
*NSET,NSET=BOT,GEN
 1,4001,500
*NSET,NSET=TOP,GEN
 30001,34001,500
*NSET,NSET=BOTEND,GEN
 301,4301,500
*NSET,NSET=TOPMID,GEN
 30151,34151,500
*NSET,NSET=CLAMP,GEN
 301, 4301,500
```

```
 5301, 9301,500
 10301,14301,500
 20301,24301,500
 25301,29301,500
 30301,34301,500
**cat
*NSET, NSET=TOPL
 40301,41301,42301,43301,44301
****************************
**GENERATION OF ELEMENTS **
***************************
*ELEMENT,TYPE=C3D8I
 1001,1,3,1003,1001,10001,10003,11003,11001
**
*ELGEN,ELSET=SOLIDO
 1001, 150, 2, 1, 4, 1000, 150, 2,20000,2000
**
*USER ELEMENT,TYPE=U2,NODES=8,UNSYMM,COORDINATES=3,
 I PROPERTIES=1, PROPERTIES=7,VARIABLES=4
 1,2,3
*ELEMENT,TYPE=U2
 1,10001,10003,11003,11001,20001,20003,21003,21001
*USER ELEMENT,TYPE=U1,NODES=8,UNSYMM,COORDINATES=3,
 I PROPERTIES=1, PROPERTIES=7,VARIABLES=4
 1,2,3
*ELEMENT,TYPE=U1
 185,10091,10093,11093,11091,20091,20093,21093,21091
*ELGEN,ELSET=DECOPEN
 1,46,2,1,4,1000,46
*ELGEN,ELSET=DECLOSED
 185,104,2,1,4,1000,104
*ELSET,ELSET=LOADMID
 3075,3225,3375,3525,3076,3226,3376,3526
*ELSET,ELSET=LOADEND
 3001,3151,3301,3451
*UEL PROPERTY,ELSET=DECOPEN
**
** GIc GIIc SI SII Kp Eta Thick NLGEOM
 0.9690, 1.719, 80.0, 100.0, 1.E+6, 2.284,, 1
**
*UEL PROPERTY,ELSET=DECLOSED
**
** GIc GIIc SI SII Kp Eta Thick NLGEOM
 0.9690, 1.719, 80.0, 100.0, 1.E+6, 2.284,, 1
**
*ORIENTATION,NAME=OR1
 1.,0.,0.,0.,1.,0.
 3,0.
*SOLID SECTION,MATERIAL=CFRP,ELSET=SOLIDO,ORIENTATION=OR1
*MATERIAL,NAME=CFRP
*ELASTIC,TYPE=ENGINEERING CONSTANTS
 122.7E+03,10.1E+03,10.1E+03,0.25,0.25,0.45,5.5E+03,5.5E+03
```

```
 3.7E+03
** 128.9E+03,10.1E+03,10.1E+03,0.25,0.25,0.45,5.5E+03,5.5E+03 **
3.7E+03 *
* BOUNDARY CONDITIONS ** **
*BOUNDARY
 BOT ,1,3
 BOTEND,3,3
*EQUATION
 3
 30001,3,0.54, 30151,3,-1.54, 40301,3,1.0
 3
 31001,3,0.54, 31151,3,-1.54, 41301,3,1.0
 3
 32001,3,0.54, 32151,3,-1.54, 42301,3,1.0
 3
 33001,3,0.54, 33151,3,-1.54, 43301,3,1.0
 3
 34001,3,0.54, 34151,3,-1.54, 44301,3,1.0
** *PREPRINT,ECH=NO,HISTORY=NO,MODEL=YES
*RESTART,WRITE,FREQ=4,OVERLAY
********************
*STEP,INC=10000,NLGEOM *STATIC
 .01,.5, ,0.04
**CAT
*BOUNDARY, TYPE=DISP
 TOPL,3,3,-4.5
*CONTROLS,PARAMETERS=FIELD,FIELD=DISPLACEMENT
 .1,1.0
*CONTROLS,PARAMETERS=TIME INCREMENTATION
 1500,1500,,1500,1500
*CONTROLS,PARAMETERS=LINE SEARCH
 4,4,0.25,0.25,0.15
*OUTPUT,HISTORY,FREQUENCY=1
*NODE OUTPUT,NSET=TOP
 U3
*NODE OUTPUT,NSET=TOPMID
 U3
*NODE OUTPUT,NSET=TOPL
 U3
*NODE OUTPUT,NSET=BOT
 RF3
*NODE OUTPUT,NSET=BOTEND
 RF3
*OUTPUT,FIELD,FREQUENCY=15
*NODE OUTPUT
 U
*ELEMENT OUTPUT
 S
*END STEP
******************
**
** STEP 2 **
```

```
**
*******************
*STEP,INC=10000,NLGEOM
*STATIC
 .005,1.0, ,0.005
**CAT
*BOUNDARY, TYPE=DISP
 TOPL,3,3,-8.
*CONTROLS,PARAMETERS=FIELD,FIELD=DISPLACEMENT
 .1,1.0
*CONTROLS,PARAMETERS=TIME INCREMENTATION
 1500,1500,,1500,1500
*CONTROLS,PARAMETERS=LINE SEARCH
 4,4,0.25,0.25,0.15
*OUTPUT,HISTORY,FREQUENCY=1
*NODE OUTPUT,NSET=TOP
 U3
*NODE OUTPUT,NSET=TOPMID
 U3
*NODE OUTPUT,NSET=TOPL
 U3
*NODE OUTPUT,NSET=BOT
 RF3
*NODE OUTPUT,NSET=BOTEND
 RF3
*OUTPUT,FIELD,FREQUENCY=15
*NODE OUTPUT
 U
*ELEMENT OUTPUT
 S
*END STEP
**** end of model ****
```

Bibliography

[1] MIL-HDBK-17-3F, Military Handbook, Polymer Matrix Composites. U.S. Department of Defense (2002).

[2] Caiazzo, (2001). A.A. Caiazzo, F. Costanzo, Modelling the nidireccion behaviour of layered composites with evolving cracks, International Journal of Solids and Structures, 38 (2001), 3469-3485.

[3] N.J. Pagano, G.A. Schoeppner, Delamination of polymer matrix composites: problems and assessment, (Ed.) Anonymous Kelly, A.; Zweben, D., Oxford (UK) (2000.

[4] T.E. Tay, F. Shen, Analysis of delamination growth in laminated composites with consideration for residual thermal stess effects, Journal of Composite Materials 36, 36 (11) (2002), 1299–1320.

[5] A.S. Crasto, R.Y. Kim, Hygrothermal influence on the free-edge delamination of composites under compressive loading, In: Composite Materials: Fatigue and Fracture 6, (Ed.) Anonymous Armanios, E.A., Philadelphia (1997), 381–393.

[6] V.V. Bolotin, Delaminations in composite structures: Its origin, buckling, growth and stability, Composites Part B-Engineering 27 (2) (1996), 29-145.

[7] V.V. Bolotin, Mechanics of delaminations in laminate composite structures, Mechanics of Composite Materials 37 (5-6) (2001), 367-380.

[8] W.L. Bradley, C.R. Corleto, D.P. Goetz, Fracture physics of delmaintion of composite materials, AFOSR-TR-88-0020 (1987).

[9] N. Blanco, Variable mixed-mode delamination in composite laminates under fatigue conditons: testing and analysis, PhD Thesis, University of Girona (2005).

[10] I.W. Obreimoff, The splitting strength of mica, Proceedings of the Royal Society of London A 127 (1930), 290–297.

[11] C.G. Dávila, E.R. Johnson, Analysis of delamination initiation in postbuckled dropped-ply laminates, AIAA Journal, 31 (1993), 721–727.

[12] P.P. Camanho, F.L. Matthews, Delamination onset prediction in mechanically fastened joints in composite laminates, Journal of Composite Materials, 33 (1999), 906–927.

[13] S. Liu, Quasi-impact damage initiation and growth of thick-section and toughened composite material. International Journal of Solids and Structures, 31 (1999), 3079–3098.

[14] Z. Zou, S.R. Reid, S. Li, P.D. Soden, Modelling interlaminar and intralaminar damage in filament wound pipes under quasi-static indentation, Journal of Composite Materials, 36 (2002), 477–499.

[15] G.R. Irwin, Analysis of stresses and strains near the end of a crack transversing a plate, Journal for Applied Mechancis, 24 (1957), 361–366.

[16] E.F. Rybicki, M.F. Kanninen, A finite element calculation of stress intensity factors by a modified crack closure integral, Engineering Fracture Mechanics, 9 (1977), 931–938.

[17] I.S. Raju, Calculation of strain-energy release rates with higher order and singular finite elements. Engineering Fracture Mechanics, 38(3) (1987),251–274.

[18] Z. Zou, S.R. Reid, S. Li, P.D. Soden, Mode separation of energy release rate for delamination in composite laminates using sublaminates. International Journal of Solids and Structures, 38 (2001), 2597–2613.

[19] R. Krueger, The virtual crack closure technique: history, approach and applications, NASA/CR-2002-211628 (2002).

[20] J.R. Rice, A path independent integral and the approximate analysis of strain concentration by notches and cracks, Journal for Applied Mechanics, 35 (1968), 379–386.

[21] T.K. Hellen, On the method of the virtual crack extension. International Journal for Numerical Methods in Engineering, 9 (1975), 187–207.

[22] D.M Parks, A stiffness derivative finite element technique for determination of crack tip stress intensity factors, International Journal of Fracture, 10(4) (1974), 487–502.

[23] A.A. Griffith, The phenomena of rupture and flow in solids, Philosophical transactions of the Royal Society, London, Series A, 221 (1921), 163–198.

[24] D.S. Dugdale, Yielding of steel sheets containing slits. Journal of the Mechanics and Physics of Solids, 8 (1960), 100–104.

[25] G. Barenblatt, The mathematical theory of equilibrium cracks in brittle fracture, Advances in Applied Mechanics , 7 (1962), 55–129.

[26] A. Hillerborg, M. Modéer, P.E. Petersson, Analysis of crack formation and crack growth in concrete by means of fracture mechanics and finite elements, Cement and Concrete Research., 6 (1976), 773–782.

[27] Z.P. Bažant, M. Jirásek, Nonlocal integral formulations of plasticity and damage: survey of progress, J. Engineering Mechanics, 128 (2002), 1119-1149.

[28] L. Ye, Role of Matrix Resin in Delamination Onset and Growth in Composite Laminates, Composites Science and Technology, 33 (1988), 257-277.

[29] M.L. Benzeggagh, M. Kenane, Measurement of Mixed-Mode delamination Fracture Toughness of Unidirectional Glass/Epoxy Composites With Mixed-Mode Bending Apparatus, Composites Science and Technology, 49 (1996(, 439–449.

[30] B.W. Kim, A.H. Mayer, Influence of fiber direction and mixed-mode ratio on Delamination fracture toughness of carbon/epoxy laminates, Composites Science and Technology, 63 (2003), 695–713.

[31] A. Carpinteri, Post-peak and post-bifurcation analysis of cohesive crack propagation, Engineering Fracture Mechanics, 32 (1998), 265–78.

[32] P. Bocca, A. Carpinteri, S. Valente, Mixed mode fracture of concrete, International Journal of Solids and Structures, 27 (1991), 1139–1153.

[33] T.N. Bittencourt, A.R Ingraffea, J. Llorca, Simulation of arbitrary cohesive crack propagation, In: Z.P. Bâzant (ed.), Fracture Mechanics of Concrete Structures, Amsterdam: Elsevier (1992), 339–350.

[34] V. Tvergaard, J. Hutchinson, The relation between crack growth resistance and fracture process parameters in elastic-plastic solids, Journal of Mechanics and Physics of Solids, 40 (1992), 1377–1397.

[35] A.S. Gullerud, X. Gao, R.H. Dodds, R. Haj-Ali, Simulation of ductile crack growth using computational cells: numerical aspects, Engineering Fracture Mechanics, 66 (2000), 65–92.

[36] X. Xu, A. Needleman, Numerical simulations of fast crack growth in brittle solids, Journal of Mechanics and Physics of Solids, 42 (9) (1994), 1397–1434.

[37] G.T. Camacho, M. Ortiz, Computational modelling of impact damage in brittle materials, International Journal of Solids and Structures, 33 (1996), 2899–2938.

[38] O. Allix, P. Ladevèze, A. Corigliano, Damage analysis of interlaminar fracture specimens, Composite Structures, 31 (1995), 66–74.

[39] O. Allix, A. Corigliano, Modelling and simulation of crack propagation in mixed-mode interlaminar fracture specimens, International Journal of Fracture, 77 (1996), 111–140.

[40] W. Cui, M. Wisnom, A combined stress-based and fracture-mechanics-based model for predicting delamination in composites, Composites, 24 (1993), 467–474.

[41] J. Schellekens, R. de Borst, A nonlinear finite-element approach for the analysis of mode-I free edge delamination in composites, International Journal of Solids and Structures, 30 (9) (1993), 1239–1253.

[42] J.L. Chaboche, R. Girard, A. Schaff, Numerical analysis of composite systems by using interphase/interface models, Composite Mechanics, 20 (1997), 3–11.

[43] U. Mi, M. Crisfield, G. Davies, Progressive delamination using interface elements, Journal of Composite Materials, 32 (1998), 1246–1272.

[44] J. Chen, M. Crisfield, A. Kinloch, E. Busso, F. Matthews, Y. Qiu, Predicting progressive delamination of composite material specimens via interface elements, Mechanics of Composite Materials and Structures, 6 (1999), 301–317.

[45] G. Alfano, M. Crisfield, Finite element interface models for the delamination analysis of laminated composites: mechanical and computational issues,

International Journal for Numerical Methods in Engineering, 77 (2) (2001), 111–170.

[46] J. Segurado and J. Llorca, A new three-dimensional interface finite element to simulate fracture in composites, International Journal of Solids and Structures, 41(11-12) (2004), 2977–2993.

[47] P.P. Camanho, C.G. Dávila, M. de Moura, Numerical simulation of mixed-mode progressive delamination in composite materials, Journal of Composite Materials, 37 (2003), 1415–1438.

[48] V. Goyal-Singhal, E. Johnson, C.G. Dávila, Irreversible constitutive law for modeling the delamination process using interfacial surface discontinuities, Composite Structures, 64 (2004), 91–105.

[49] A. Turon, P.P. Camanho, J. Costa, C.G. Dávila, A damage model for the simulation of delamination in advanced composites under variable-mode loading, Mechanics of Materials, 38(11) (2006), 1072-1089.

[50] J.C. Simo, J. Oliver and F. Armero, An analysis of strong discontinuities induced by strain-softening in rate-independent inelastic solids, Computational Mechanics. 12 (1993), 277–296.

[51] J.C. Simo and J. Oliver, A new approach to the analysis and simulation of strong discontinuities, In: Z.P. Bâzant et al, Fracture and Damage in Quasi-brittle Structures, E&FN Spon (1994), 25–39.

[52] F. Armero and K. Garikipati, An analysis of strong discontinuities in multiplicative finite strain plasticity and their relation with the numerical simulation of strain localization in solids, International Journal of Solids and Structures, 33 (1996), 2863–2885.

[53] J. Oliver, Continuum modelling of strong discontinuities in solid mechanics using damage models, Computational Mechanics,17(2) (1995), 49–61.

[54] T. Belytschko, T. Black, Elastic crack growth in finite elements with minimal remeshing, International Journal for Numerical Methods in Engineering, 45(5) (1999), 601–620.

[55] N. Möes, J. Dolbow, T. Belytschko, A finite element method for crack growth without remeshing, Internatinal Journal for Numerical Methods in Engineering, 46 (1999), 131–150.

[56] N. Moes and T. Belytschko, Extended finite element method for cohesive crack growth, Engineering Fracture Mechanics, 69(7) (2002), 813–833.

[57] J. Oliver, On the discrete constitutive models induced by strong discontinuity kinematics and continuum constitutive equations, International Journal of Solids and Structures, 37 (2000), 7207–7229.

[58] I. Babuska, J.M. Melenk, The partition of unity method. International Journal for Numerical Methods in Engineering, 40(4) (1997), 727–758.

[59] J.J.C. Remmers, N.G. Wells, R. de Borst, A solid-like shell element allowing for arbitrary delaminations, International Journal for Numerical Methods in Engineering, 58(13) (2003), 2013–2040.

[60] B. Cotterell, I.Y.W Mai, Fracture mechanics of cmentitious materials, London, UK: Blackie Academic &professional, an Imprint of Chapman and Hall (1996).

[61] P. Brenet, F. Conchin, G. Fantozzo, P. Reynaud, D. Rouby, C. Tallaron, Direct measurement of the crack bridging tractions: a new approach o the facture behaviour of ceramic-matrix composites, Computational Science Technology, 56 (1996), 817–823.

[62] E.K. Gamstedt, T.K. Jacobsen, B.F. Sørensen, Determination of cohesive laws for materials exhibiting large scale damage zones, Analytical and Com-

putational Fracture Mechanics of NonHomogeneos Materials, B.L. Karihalov (ed.), Kluwer, Dordrecht (2002), 349–353.

[63] B.F. Sørensen, T.K. Jacobsern, Determination of cohesive laws by the J integral approach, Engineering fracture mechanics, 70 (2003), 1841–1858.

[64] A. Carpinteri, P. Cornetti, F. Barpi, S. Valente, Cohesie crack model description of ductile to brittle size-scale transition: dimensional analysis vs. renormalization group theory, Engineering fracture mechanics, 70 (2003), 1809–1839.

[65] M. Elices, G.V. Guinea, J. Gómez, J. Planas, The cohesive zone model: advantages, limitations and challenges, Engineering Fracture Mechanics, 69 (2002), 137–163.

[66] Z. Zou, S.R Reid, S. Li, A continuum damage model for delaminations in laminated composites, Journal of the Mechanics and Physics of Solids, 51 (2003), 333–356.

[67] A. Needleman, A continuum model for void nucleation by inclusion debonding, Journal of Applied Mechanics, 54 (1987), 525–532.

[68] G.Alfano, On the influence of the shape of the interface law on the application of cohesive-zone models, Composites Science and Technology, 66 (6) (2006), 723–730.

[69] Yan, A.M., Marechal, E., Ngyen-Dang, H., A finite-element model of mixed-mode delamination in laminated composites with and R-curve effect. *Composites Science and Technology*, **61**, 1413-1427, 2001.

[70] N.E. Jansson, R. Larsson, A damage model for simulation of mixed-mode delamination growth. Composite Structures, 53 (2001), 409-417.

[71] Li, D., Wisnom, M., Modelling damage initiation and propagation composites using interface elements. Presented at the *Computer Aided Design in Composite Material Technology- International Conference.* Southampton, UK, 1994.

[72] Petrossian, Z., Wisnom, M.R., Prediction of Delamination Initiation and Growth From Discontinuous Plies Using Interface Elements, *Composites-Part A*, **29**, 503-515, 1998.

[73] Ladevèze, P., Allix, O., Gornet, L., Lévêque, D., et al., A computational damage mechanics approach for laminates: identification and comparisons with experimental results, in *Damage Mechanics in Engineering Materials,* G.Z. Voyiadkjis, J.W.W. Ju, and J.L. Chaboche, Editors. Elsevier Science B.V. 481-499, 1998.

[74] Borg, R., Nilsson, L. Simonsson, K., Modeling of delamination using a discretized cohesive zone and damage formulation.*Composites Science and Technology*, **62**, 1299-1314, 2002.

[75] Hibbitt, Karlsson, Sorensen. ABAQUS 6.2 User's Manuals. Pawtucket, USA, 1996.

[76] Ortiz, M., Pandolfi, A., Finite-deformation irreversible cohesive elements for three- dimensional crack propagation analysis. *International Journal for Numerical Methods in Engineering,* **44**, 1267-82, 1999.

[77] Simo, J., Ju, J. W., Strain- and stress- based continuum damage model- I. Formulation. *International Journal Solids Structures*, **23**, 821-840, 1987.

[78] Simo, J., Ju, J. W., Strain- and stress- based continuum damage model- II. Computational aspects. *International Journal Solids Structures*, **23**, 841-869, 1987.

[79] Mazars, J., Mechanical Damage and Fracture of Concrete Structures. *Advances in Fracture Research (Fracture 81)*, **4**, 1499-1506. Pergamon Press, Oxford, 1982.

[80] Oliver, J., Cervera, M., Oller, S., Lubliner, J., Isotropic damage models and smeared crack analysis of concrete. *Second International Conference on Computer Aided Analysis and Design of Concrete Structures,* **2**, 945-958, 1990.

[81] Goyal-Singhal, V., Johnson, E.R., Dávila, C.G, and Jaunky, N., An Irreversible Constitutive Law for Modeling the Delamination Process Using Interface Elements. *43rd AIAA/ASME/ASCE/AHS/ASC Structures, Structural Dynamics and Materials Conference*, Colorado,USA, 2002.

[82] E. Reddy Jr., F. Mello, T. Guess, Modeling the initiation and growth of delaminations in composite structures, Journal of Composite Materials, 31 (1997), 812–831.

[83] Schellekens, J.C.J., de Borst R., On the numerical integration of interface elements. *Int. J. Numer. Meth. Engng.*, **36**: 43-66, 1992.

[84] Wu, E.M., Reuter Jr., R.C., Crack extension in fiberglass reinforced plastics. *T. & AM Report No.* 275. University of Illinois, 1965.

[85] Camanho, P.P., Dávila, C.G., Pinho, S.T., Fracture analysis of composite co-cured structural joints using decohesion elements. *Fatigue Fract Engng Mater Struct,* **27**,745-757, 2004.

[86] Li, J., Sen, J.K., Analysis of frame-to-skin joint pull-off tests and prediction of the delamination failure. *42nd AIAA/ASME/ASCE/AHS/ASC Structures, Structural Dynamics and Materials Conference, Seattle, WA, USA,* 2000.

[87] Li, J., Three-Dimensional effects in the prediction of flange delamination in composite skin-stringer pull-off specimens. *15th Conference of the American Society for Composites Texas, USA,* 2000.

[88] Larsson, R., Jansson, N., Geometrically non-linear damage interface based on regularized strong discontinuity. *Int. J. Numer. Meth Engng,* **54**, 473-497, 2002.

[89] Belytschko, T., Liu, W.K., Moran, B., Nonlinear Finite Elements for Continua and Structures. *John Wiley & Sons, LTD*, 2001.

[90] Crews, J.H., Reeder, J.R., A Mixed-Mode Bending Apparatus for Delamination Testing. *NASA TM* 100662, 1988.

[91] Reeder, J.R., Crews, J.H., Mixed-Mode Bending Method for Delamination Testing. *AIAA Journal* **28**, 1270-1276, 1990.

[92] Reeder, J.R., Crews, J.H., Nonlinear Analysis and Redesign of the Mixed-Mode Bending Delamination Test. *NASA TM* 102777, 1991.

[93] Krueger, R., Cvitkovich, M.K., O'Brien, T.K., Minguet, P.J., Testing and analysis of composite skin/stringer debonding under multi-axial loading. *Journal of Composite Materials*, **34**, 1263-1300, 2000.

[94] Falk, M.L., Needleman, A., Rice J.R., A critical evaluation of cohesive zone models of dynamic fracture. *Journal de Physique IV, Proceedings*, 543-550, 2001.

[95] Rice, J.R., Dislocation nucleation from a crack tip- an analysis based on the PIERLS concept. *Journal of the Mechanics and Physics of Solids*, **40**, 239-271, 1992.

[96] Rice, J.R., Beltz, G.E.,The activation-energy for dislocation. *Journal of the Mechanics and Physics of Solids*, **42**, 333-360, 1994.

[97] Camacho, G.T., Ortiz, M.,Computational modelling of impact damage in brittle materials. *International Journal of Solids and Structures*, **33**, 2899-2938, 1996.

[98] Ruiz, G., Pandolfi, A., Ortiz, M., Three-dimensional cohesive modeling of dynamic mixed-mode fracture. *International Journal for Numerical Methods in Engineering*, **52**, 97-120, 2001.

[99] Daudeville, L., Allix, O., Ladevèze, P., Delamination analysis by damage mechanics. Some applcations. *Composites Engineering,* **5**(1), 17-24, 1995.

[100] Zou, Z., Reid, S.R., Li, S., Soden, P.D., Modelling interlaminar and intralaminar damage in filament wound pipes under quasi-static indentation. *Journal of Composite Materials*, **36**, 477-499, 2002.

[101] Klein, P.A., Foulk, J.W., Chen, E.P., Wimmer, S.A., Gao, H., Physics-based modeling of brittle fracture: cohesive formulations and the application of meshfree methods. *Sandia Report* SAND2001-8099, 2000.

[102] Schellekens, J., Computational strategies for composite structures. PhD thesis, Delft University of Technology, 1992.

[103] Irwin, G.R., Plastic zone near a crack and fracture toughness. In *Proceedings of the Seventh Sagamore Ordnance Materials Conference,* vol. **IV**, 63-78, New York: Syracuse University, 1960.

[104] Hui, C.Y., Jagota, A., Bennison, S.J., Londono, J.D., Crack blunting and the strength of soft elastic solids. *Proceedings of the Royal Society of London A*, **459**, 1489-1516, 2003.

[105] J. Rice, The mechanics of earthquake rupture, Physics of the Earth's Interior (Proc. International School of Physics "Enrico Fermi", Course 78, 1979; ed. A.M. Dziewonski and E. Boschi), Italian Physical Society and North-Holland Publ. Co. (1980) 555–649.

[106] Yang, Q., Cox, B., Cohesive models for damage evolution in laminated composites, *International Journal of Fracture*, **133**, 107-137, 2005.

[107] Moës, N., Belytschko, T., Extended finite element method for cohesive crack growth. *Engineering Fracture Mechanics*, **69**,813-833, 2002.

[108] Dávila, C.G., Camanho, P.P., de Moura, M.F.S.F., Mixed-Mode decohesion elements for analyses of progressive delamination. *Proceedings of the 42nd AIAA/ASME/ASCE/AHS/ASC Structures, Structural Dynamics and Materials Conference,* Seattle, Wasington, April 16-19, 2001.

[109] Bažant, Z.P., Planas, J., Fracture and size effect in concrete and other quasibrittle materials, *CRC Press*, 1998.

[110] Morais, A.B., de Moura, M.F., Marques, A.T., de Castro, P.T., Mode-I interlaminar fracture of carbon/epoxy cross-ply composites. *Composites Science and Technology,* **62**, 679-686, 2002.

[111] Schellekens, J.C.J., de Borst, R., Numerical simulation of free edge delamination in graphite-epoxy laminates under uniaxial tension, *6th International Conference on Composite Structures*, 647-657, 1991.

[112] Crossman, F.W., Wang, A.S.D., The dependence of transverse cracking and delamiantion on ply thickness in graphite/epoxy laminates. *Damage in Composite Materials*, ed. K.L. Reifsnider, American Society for Testing and Materials (ASTM STP 775), Ann Arbor, Michigan, 118-39, 1982.

[113] O'Brien, T.K., Characterization of delamination onset and growth in a composite laminate, *Damage in Composite Materials* , ed. K.L. Reifsnider, American Society for Testing and Materials (ASTM STP 775), Ann Arbor, Michigan, 140-67, 1982.

[114] Wang, A.S.D., Fracture analysis of interlaminar cracking, *Interlaminar Response of Composite Materials*, Ed. N.J. Pagano, Elsevier Science Publishers BV, Amsterdam, 69-109, 1989.

[115] Li, S., Lim, S.H., Variational principles for generalized plane strain problems and their applications, *Composites: Part A*, **36**, 353-365, 2005.

[116] Pipes, R.B., Pagano, N.J., Interlaminar stresses in composite laminates under uniform axial tension, *J. Composite Materials*, 538-548, 1971.

[117] J. Degrieck, W. Van Paepegem, Fatigue damage modelling of fibre-reinforced composite materials: Review, Applied Mechanics Reviews, 54 (4) (2001), 279–300.

[118] R. Talreja, Fatigue of composite materials, Lancaster, PA: Technomic (1987).

[119] R. Talreja, Damage mechanics and fatigue life assessment of composite materials, International Journal of Damage Mechanics , 8 (4) (1999), 339-354.

[120] K.L. Reifsnider, Fatigue of composite materials, Amsterdam: Elsevier (1991).

[121] G.P. Sendeckyj, Fitting models to composite materils fatigue data. In: Chamis CC (ed.), Test methods and design allowables for fibrous compoistes, ASTM STP 734, American Society for Testing and Materials, (1981) 245–260.

[122] J. Andersons, Methods of fatigue prediction for composite laminates. A review, Mechanics of Composite Materials 6 (1994), 545-554.

[123] J.A. Mayugo, Estudio constitutivo de materiales compuestos laminados sometidos a cargas cíclicas, PhD Thesis, Universitat Politècnica de Catalunya (2003).

[124] Z. Hashin, A. Rotem, A fatigue failure criterion for fibre reinforced materials, Journal of Composite Materials 7 (1973), 448-464.

[125] P. Paris, M. Gomez, W. Anderson, A rational analytical theory of fatigue, Trend in Engineering, 13 (1961), 9–14.

[126] P. Paris, F. Erdogan, Critical analysis of propagation laws, Journal of Basic Engineering, 85 (1963), 528–534.

[127] H.L. Ewalds, Fracture Mechanics. Edward Arnold, London (1984).

[128] N. Dowling, J. Begley, Fatigue crack growth during gross plasticity and the J-integral, ASTM STP 590 (1976), 82–103.

[129] D. McDowell, An engineering model for propagation of small cracks in fatigue, Engineering Fracture Mechanics, 56 (1997), 357–377.

[130] J. Lemaitre, J. Sermage, R. Desmorat, A two scale damage concept applied to fatigue, International Journal of Fracture, 97 (1999), 67–81.

[131] Q. Yang, D. Shim, S. Spearing, A cohesive zone model for low cycle fatigue life prediction of solder joints, Microelectronic Engineering, 75 (2004), 85–95.

[132] K. Roe, T. Siegmund, An irreversible cohesive zone model for interface fatigue crack growth simulation, Engineering Fracture Mechanics, 70 (2003), 209–232.

[133] O. Nguyen, E. Repetto, M. Ortiz, R. Radovitzky, A cohesive model for fatigue crack growth, International Journal of Fracture, 110 (2001), 351–369.

[134] V. Goyal-Singhal, E. Johnson, Cohesive-decohesive interfacial constitutive law for the analyses of fatigue crack initiation and growth, 44th AIAA/ASME/ASCE/AHS Structures, Structural Dynamics, and Materials Conference AIAA-2003-1678, (2003), 1–11.

[135] P. Boisse, P. Bussy, P. Ladevèze, A new approach in nonlinear mechanics– the large time increment method, International Journal for Numerical Methods in Engineering, 29 (1990), 647–63.

[136] J.Y. Cognard, P. Ladevèze, P. Talbot, A large time increment approach for thermo–mechancial problems, Advances in Engineering SOftware, 20 (1999), 583–593.

[137] W. Van Paepegem, J. Degrieck, Fatigue degradation modelling of plain woven glass/epoxy composites, Composites Part A, 32 (10) (2001), 1433–1441.

[138] D. Cojocaru, A. M. Karlsson, A simple numerical method of cycle jumps for cyclically loaded structures, Inetrantional Journal of Fatigue, (2006), in Press.

[139] R. Peerling, W. Bredelmans, R. de Borst, M. Geers, Gradient-enhaced damage modelling of high-cyclic fatigue, International Journal of Numerical Methods in Engineering, 9 (2000), 1547–1569.

[140] P. Robinson, U. Galvanetto, D. Tumino, G. Bellucci, Numerical simulation of fatigue-driven delamination using interface elements, International Journal of Numerical Methods in Engineering, 63 (2005), 1824–1848.

[141] P. Robinson, U. Galvanetto, D. Tumino, G. Bellucci, On the numerical simulation of fatigue-driven delamination using interface elements, International Journal of Fatigue, in Press.

[142] T.K. Ob́rien, Fatigue Delamination Behavior of Peek Thermoplastic Composite Laminates, Journal of Reinforced Plastics and Composites 7 (4) (1988), 341-359.

[143] A. Sjögren, L.E. Asp, Effects of temperature on delamination growth in a carbon/epoxy composite under fatigue loading, International Journal of Fatigue 24 (2-4) (2002), 179-184.

[144] C.G. Gustafson, M. Hojo, Delamination Fatigue Crack-Growth in Unidirectional Graphite Epoxy Laminates, Journal of Reinforced Plastics and Composites 6 (1) (1987), 36-52.

[145] M. Hojo, K. Tanaka, C.G. Gustafson, R. Hayashi, Effect of Stress Ratio on Near-Threshold Propagation of Delamination Fatigue Cracks in Unidirectional CFRP, Composites Science and Technology 29 (4) (1987), 273-292.

[146] M. Hojo, S. Matsuda, S. Ochiai, Delamination fatigue crack growth in CFRP laminates under mode I and II loadings -effect of mesoscopic structure on fracture mechanism-, Proceedings of the International Conference on Fatigue of Composites, Paris (F), (1997), 15-26.

[147] S. Matsuda, M. Hojo, S. Ochiai, Mesoscopic fracture mechanism of mode II delamination fatigue crack propagation in interlayer-toughened CFRP, Jsme International Journal Series A-Solid Mechanics and Material Engineering 40 (4) (1997), 423-429.

[148] H. Tanaka, K. Tanaka, Mixed-Mode Growth of Interlaminar Cracks in Carbon/Epoxy Laminates under Cyclic Loading, Proceedings of the 10th International Conference on Composite Materials, Whistler, B.C., Canada, (1995), 181-189.

[149] K. Tanaka, H. Tanaka, Stress-Ratio Effect on Mode II Propagation of Interlaminar Fatigue Cracks in Graphite/Epoxy Composites, In: Composite Materials: Fatigue and Fracture (6th vol.). (Ed.) Armanios, E.A. American Society for Testin and Materials, Philadelphia, (1997), 126-142.

[150] J. Schön, T. Nyman, A. Blom, H. Ansell, A numerical and experimental investigation of delamination behaviour in the DCB specimen, Composites Science and Technology 60 (2) (2000), 173-184.

[151] J. Andersons, M. Hojo, S. Ochiai, Model of delamination propagation in brittle-matrix composites under cyclic loading, Journal of Reinforced Plastics and Composites 20 (5) (2001), 431-450.

[152] J. Andersons, M. Hojo, S. Ochiai, Empirical model for stress ratio effect on fatigue delamination growth rate in composite laminates, International Journal of Fatigue 26 (6) (2004), 597-604.

[153] R. Krueger, I.L. Paris, T.K. OB́rien, Fatigue life methodology for bonded composite skin/stringer configurations, Proceedings of the American Societey for Composites, Fifteenth Technical COnference, Technomic Publishing (2000), 729–736.

[154] R. Krueger, I.L. Paris, T.K. OB́rien, P.J. Minguet, Fatigue life methodology for bonded composite skin/stringer configurations, NASA/TM-2001-21842 (2001).

[155] R.L. Ramkumar, J.D. Whitcomb, Characterization of mode I and mixed–mode delamination growth in T300/5208 graphite/epoxy, In: Delamination and Debonding of Materials. (Ed.) Anonymous Johnson, W.S., Philadelphia (USA) (1985), 315-335.

[156] A.J. Russell, K.N. Street,Predicting interlaminar fatigue crack growth rates in compressively loaded laminates, In: Composite Materials: Fatigue and Fracture II. (Ed.) Lagace, P.A. American Society for Testing and Materials, Philadelphia (USA) (1989), 162-178.

[157] C. Dahlen, G.S. Springer, Delamination Growth in Composites Under Cyclic Loads, Journal of Composite Materials 28 (8) (1994), 732-781.

[158] G.A. Kardomateas, A.A. Pelegri, B. Malik, Growth of internal delaminations under cyclic compression in composite plates, (Ed.) Anonymous Kardomateas, G.A.; Rajapakse, Y.D.S., New York (USA) (1994), 13-29.

[159] G.A. Kardomateas, B. Malik, Fatigue delamination growth under cyclic compression in glass/epoxy composite beam/plates, Polymer Composites 18 (2) (1997), 169-178.

[160] G.A. Kardomateas, A.A. Pelegri, B.Malik, Growth of Internal Delaminations Under Cyclic Compression in Composite Plates, Journal of the Mechanics and Physics of Solids 43 (6) (1995), 847-868.

[161] J.W. Hutchinson, Z. Suo, Mixed mode cracking in layered materials, In: Advances in Applied Mechanics. (Ed.) Hutchinson, J.W., Wu, T.Y. Academic Press Inc., Boston (USA) (1992), 63-191.

[162] M. Kenane, M.L. Benzeggagh, Mixed-mode delamination fracture toughness of unidirectional glass/epoxy composites under fatigue loading, Composites Science and Technology 57 (5) (1997), 597-605.

[163] N. Blanco, E.K. Gamstedt, L.E. Asp, J.Costa, Mixed–mode delamination growth in carbon-fibre composite laminates under cyclic loading, International Journal of Solids and Structures 41 (2004), 4219–4235.

[164] M. Ortiz, A. Pandolfi, Finite-deformation irreversible cohesive elements for three-dimensional crack propagation analysis, International Journal for Numerical Methods in Engineering, 44 (1999), 1267–82.

[165] A. Turon, C.G. Dávila, P.P. Camanho, J. Costa, An engineering solution for solving mesh size effects in the simulation of delamination with cohesive zone models, Engineering Fracture Mechanics, in Press.

[166] L.M. Kachanov, Time of the rupture process under creep conditions. IZV Akad Nauk - S.S.R. Od Tech Nauk 8 (1958).

[167] L. Asp, A. Sjögren, E. Greenhalgh, Delamination growth and thresholds in a carbon/epoxy composite under fatigue loading, Journal of Composites Technology and Research, 23 (2001), 55–68.

[168] M. Juntti, L. Asp, R. Olsson, Assessment of evaluation methods for the mixed-mode bending test, Journal of Composites Technology and Research, 21 (1999), 37–48.